Title
Thermal and Statistical Properties of Nuclei and Nuclear Systems

Authors
Moretto, L.
Wozniak, G.J.

Publication Date
1989-07-01

UC-413
LBL-27502

Lawrence Berkeley Laboratory
UNIVERSITY OF CALIFORNIA

Presented at the International School of Physics
"Enrico Fermi" Summer Course CX11, Nuclear Collisions
From the Mean-Field Into the Fragmentation Regime,
Varenna, Italy, July 11–21, 1989

Thermal and Statistical Properties of Nuclei and Nuclear Systems

L.G. Moretto and G.J. Wozniak

July 1989

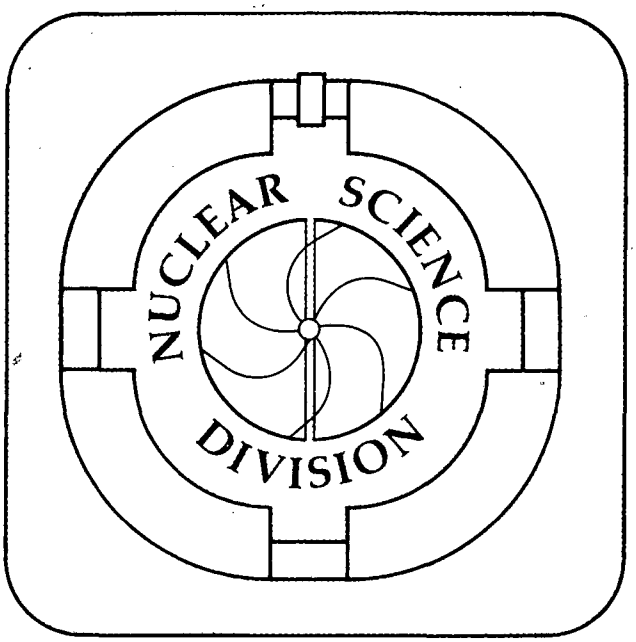

Prepared for the U.S. Department of Energy under Contract Number DE-AC03-76SF00098.

DISCLAIMER

Thermal and Statistical Properties of Nuclei and Nuclear Systems*

L. G. Moretto and G. J. Wozniak

Nuclear Science Division, Lawrence Berkeley Laboratory, Berkeley, CA 94720, USA

1. Introduction

The term statistical decay, statistical or thermodynamic equilibrium, thermalization, temperature, etc. have been used in nuclear physics since the introduction of the compound nucleus (CN) concept, and they are still used, perhaps even more frequently, in the context of intermediate- and high-energy heavy-ion reactions.

Unfortunately, the increased popularity of these terms has not made them any clearer, and more often than not one encounters sweeping statements about the alleged statisticity of a nuclear process where the "statistical" connotation is a more apt description of the state of the speaker's mind then of the nuclear reaction.

It is our goal, in this short set of lectures, to set at least some ideas straight on this broad and beautiful subject, on the one hand by clarifying some fundamental concepts, on the other by presenting some interesting applications to actual physical cases.

Let us start by distinguishing between statistical decay rates and statistical equilibrium. Statistical decay rates do not imply the existence of an actual equilibrium. They apply to the decay of a nearly stationary state according to time-dependent first-order perturbation theory or golden

rule #2.

The golden rule states that if a system in a state A decays to a system B with degeneracy ρ_B the transition rate is:

$$P_{A\to B} = \frac{2\pi}{\hbar}\left| H_{AB}\right|^2 \rho_B \ . \qquad (1)$$

If the system A, rather than being in a single state, has a degeneracy ρ_A, the "average" decay probability can still be written down as above, by simply averaging over the transition matrix elements:

$$\bar{P}_{A\to B} = \frac{2\pi}{\hbar}\overline{\left|H_{AB}\right|^2}\,\rho_B \ . \qquad (2)$$

Thus the rule that one averages over intial states and sums over final states. These transition rates do not require nor do they imply that the systems A and B are in statistical equilibrium with each other, as, in general they are not. A typical case is the beta decay of a ground-state nucleus to a specific state of the daughter nucleus. This decay is statistical in that the momentum distribution of the emitted electron and (anti)neutrino is in accordance with their corresponding phase space.

The case of a CN has to be dealt with with some care, as it is the case most subjected to improper statements. We must distinguish first between the formation of a CN and its decay. One frequently hears that a certain reaction gives rise to an equilibrated, or thermalized system called a CN. This means that one can describe the system in terms of an Hamiltonian H_A which gives rise to a set of eigenstates that would be stationary if it were not for the perturbation Hamiltonian H_{AB} responsible for their decay. The only statistical parameter is the level density ρ_A or the number of eigenstates per unit energy at a given energy E which are assumed to be "equally" populated.

The statistical or thermal decay of this CN means that each state decays according to Eq. 1, or

better that the system A with an energy E and density of states ρ_A has an average decay rate according to Eq. 2.

In summary, we have first the formation of a quasi-stationary system whose states in a given energy interval ΔE are equally represented. This system then proceeds to decay in accordance to the phase space associated with each final state, as described by Eq. 2.

Incidentally, the fact that H_{AB} is Hermitian allows us to write:

$$P_{AB} = \frac{2\pi}{\hbar} \overline{\left| H_{AB} \right|^2} \rho_B \tag{3}$$

$$P_{BA} = \frac{2\pi}{\hbar} \overline{\left| H_{AB} \right|^2} \rho_A \tag{4}$$

$$\frac{P_{AB}}{P_{BA}} = \frac{\rho_B}{\rho_A} \quad \text{or} \quad \rho_A P_{AB} = \rho_B P_{BA} \,. \tag{5}$$

The latter equation is the "detailed balance" equation that is frequently used in compound nuclear theory to express the unknown decay probability in terms of the "allegedly" known "inverse" probability. This inverse probability is often expressed in terms of an inverse-cross section which is unwittily identified with experimental quantities that have nothing to do with it, to the great confusion of us all. But this is another story!

Statistical equilibrium is something altogether different. If a nuclear reaction is interpreted in terms of statistical or thermal equilibrium of the kind:

$$A \leftrightarrow B \tag{6}$$

one expects that a stationary regime is attained, whereby A and B are confined in a well specified volume and do in fact interact frequently, so that their population can be written in terms of their respective partition functions:

$$P(A) = \frac{q_A}{q_A + q_B} \quad \text{and} \quad P(B) = \frac{q_B}{q_A + q_B} \,, \tag{7}$$

where

$$q_A = \sum e^{-\varepsilon_a/T} \quad \text{and} \quad q_B = \sum e^{-\varepsilon_b/T}. \tag{8}$$

As the system separates or expands beyond the freeze-out volume, A and B become decoupled and reflect in their distribution the original equilibrium. There ideas will be explored in the following two sections. The last two sections will be devoted to experimental evidence, the emission of rare particles and energy fluctuations.

2. - Compound Nucleus Decay.

2.1. *Transition Rates.* - "Particle" evaporation traditionally includes neutron, proton and α-particle emission. Alpha-particle emission did not appear strange despite the complex nature of the particle, because the lack of easily excited internal degrees of freedom made ^{4}He look truly like an "elementary" particle. The similarity in mass may have led to the incorporation of the somewhat rarer emissions of ^{2}H, ^{3}H and ^{3}He under the "evaporation" label. In its simplest form, the decay width is typically written down in terms of the inverse cross section and of the phase space of the system with the particle at infinity as:

$$\Gamma(\varepsilon)d\varepsilon = \frac{8\pi g m}{2\pi\rho(E)}\frac{\varepsilon\sigma(\varepsilon)}{h^2}\rho(E - B - \varepsilon)d\varepsilon \tag{9}$$

where $\rho(\varepsilon)$ and $\rho(E - B - \varepsilon)$ are the level densities of the CN and residual nucleus, respectively; m, ε, g are the mass, kinetic energy and spin degeneracy of the emitted particle; and $\sigma(\varepsilon)$ is the inverse cross section.[1-4]

On the other hand, fission involves the emission of fragments with approximately one half the mass of the CN. The identification of fission as an independent process is based upon the vast separation in mass between the observable yields of fission fragments and of the evaporated

particles (and evaporation residues).

The fission decay width is traditionally evaluated by following the Bohr-Wheeler formalism which makes use of the transition-state method. In this approach, the reaction (fission) coordinate is determined at a suitable point in coordinate space, (typically at the saddle point) and the decay rate is identified with the phase-space flux across a hyperplane in phase space passing through the saddle point and perpendicular to the fission direction. The decay width is written[5] as:

$$\Gamma_F = \frac{1}{2\pi\rho(E)} \int \rho^*(E - B_F - \varepsilon) d\varepsilon, \qquad (10)$$

where $\rho(E)$ and $\rho^*(E - B_F - \varepsilon)$ are the level densities of the CN and of the saddle point; ε is the kinetic energy along the fission mode; and B_F is the fission barrier. As it can be seen, the dichotomy between fission and evaporation is emphasized even in the expressions for the corresponding decay rates.

It was observed some time ago that this dichotomy is deceptive.[6,7] The separation between evaporation and fission, it was claimed, was an optical illusion due to the very low cross section of products with masses intermediate between ^{4}He and fission fragments. If the emission of any fragment is not energetically forbidden, the mass distribution should be continuous from nucleons to symmetric products. Thus, there is no need to consider the two extremes of this distribution as two independent processes. **Rather, one would conclude, fission and evaporation are the two, particularly (but accidentally) obvious extremes of a single statistical decay process, the connection being provided in a very natural way by the mass asymmetry coordinate.**

As it turns out, it is indeed possible to bring out the yield of intermediate mass fragments from the abyss. In fact, experimental mass or charge yields from CN decay going continuously from

^{4}He to symmetry have now been obtained.[8-16]

In order to demonstrate the inherent unity of fission and evaporation through complex fragment emission, it is useful to consider the potential-energy landscape as a function of a suitable set of collective coordinates, among which the mass asymmetry plays a dominant role.

2.2. *The Potential Energy: Absolute and Conditional Saddle Points.* - The potential-energy surface $V(\tilde{q})$ as a function of a set of deformation coordinates $\tilde{q}$ has been studied in detail first within the framework of the liquid-drop model,[17-19] and more recently the finite-range model.[20,21] The liquid-drop model calculates the macroscopic nuclear energy for a given shape by evaluating the corresponding shape-dependent surface and Coulomb energies plus the volume and symmetry terms, which are shape independent. The finite-range model starts from a sharp-surface nucleus and spreads out the density by folding its shape with a Gaussian plus exponential function. In this way the diffuseness of the surface is dealt with, together with those proximity effects arising when portions of the nuclear surface happen to be close to each other as in strongly indented shapes.

The stationary points of the potential-energy surface, obtained by solving the set of equations

$$\frac{\partial V(\tilde{q})}{\partial \tilde{q}} = 0 \qquad (11)$$

comprise the ground state minimum, and one to three saddle points, of which the saddle point with degree of instability one, if it exists, is known as the "fission" saddle point because of its relevance to the fission process. In general, only the points of the potential-energy surface corresponding to the solutions of the above equation are of intrinsic physical significance, because they are invariant under a canonical transformation of the coordinates.

Saddle-point shapes for fissility parameter values of $x < 0.7$ are strongly constricted at the neck, so that the nascent fission fragments are already well defined in mass. Thus one can assign a physical significance to the mass-asymmetry parameter $A_1/(A_1 + A_2)$. Then it is possible to consider a cut in the potential energy along the mass-asymmetry coordinate passing through the fission saddle point, with the property that at any point the potential energy is stationary with respect to all the other degrees of freedom. Each point is then a "conditional saddle point" with the constraint of a fixed mass asymmetry. This line has been called[6,7] the "ridge line" in analogy with the term "saddle point". The shape of the ridge line depends on whether the fissility parameter lies above or below the Businaro-Gallone point.[22] This point corresponds to the fissility parameter value at which the symmetric saddle point gains/loses stability against the mass-asymmetry coordinate. For the liquid-drop model, this point occurs at $x_{BG} = 0.396$ for zero angular momentum. The properties of the ridge line above and below the Businaro-Gallone point are illustrated in Fig. 1.

Below the Businaro-Gallone point, the ridge line shows a maximum at symmetry. This is a saddle point of degree of instability two (the system is unstable both along the fission mode and the mass-asymmetry mode). As the fissility parameter x increases above x_{BG}, this saddle point splits into three saddle points. The symmetric saddle point is stable with respect to the mass-asymmetry mode (degree of instability one) and is the ordinary fission saddle point. The other two saddles, of degree of instability two, are also called Businaro-Gallone mountains, and flank symmetrically the fission saddle point. The incorporation of angular momentum maintains essentially the same topology. Its main effect is to decrease the overall heights of the barriers and to displace the Businaro-Gallone point towards lower values of the fissility parameter.

2.3. - *Complex Fragment Decay Width.* - The role of the ridge line on the emission of complex fragments can be appreciated by observing that for $x < 0.7$ at all asymmetries and for $x > 0.7$ over a progressively reduced range of asymmetries, the nuclear shapes at the ridge line are so profoundly necked-in that the ridge and scission lines approximately coincide. This means that, as the system reaches a given point on the ridge line, it is, to a large extent, committed to decay with the corresponding saddle asymmetry. On the basis of the transition-state theory one can write, for the partial decay width:[7]

$$\Gamma(Z)dZ = \frac{1}{2\pi\rho(E)} \int \rho^{**}[E - B(Z) - \varepsilon]d\varepsilon dZ \qquad (12)$$

where $\rho(E)$ is the CN level density, and $\rho^{**}[E - B(Z) - \varepsilon]$ is the level density at the conditional saddle of energy $B(Z)$, which the system is transiting with kinetic energy ε.

The units and the number of degrees of freedom associated with the various level densities are clarified by the following relations :

$$\Gamma_Z(Z) = \frac{1}{2\pi\rho(E)}\int \rho^{**}(E\text{-}B(Z)\text{-}\varepsilon)d\varepsilon \cong \frac{1}{2\pi\rho(E)}\rho^{**}[E\text{-}B(Z)]\int e^{-\varepsilon/T}d\varepsilon$$

$$\cong \frac{T}{2\pi\rho(E)}\rho^{**}[E\text{-}B(Z)] \; . \qquad (13)$$

Well above the Businaro-Gallone point, one can expand the potential energy as:

$$B(Z) = B_F + bZ^2. \qquad (14)$$

This gives rise to a fission peak whose integrated yield is:

$$\Gamma_F \cong \frac{T\,\rho^{**}(E - B_F)}{2\pi\rho(E)}\int e^{-bZ^2/T}\,dZ = \frac{T^{3/2}\,\pi^{1/2}}{2\pi\rho(E)b^{1/2}}\rho^{**}(E - B_F) = \frac{T}{2\pi\rho(E)}\rho^{*}(E - B_F) \qquad (15)$$

where we have set

$$\sqrt{\frac{\pi T}{b}}\rho^{**}(E - B_F) = \rho^{*}(E - B_F) \; . \qquad (16)$$

Alternatively,

$$\Gamma_F = \frac{1}{2\pi\rho(E)} \iint \rho^{**}(E - B_F - bZ^2 - \varepsilon) dZ d\varepsilon = \frac{1}{2\pi\rho(E)} \sqrt{\frac{\pi T}{b}} \int \rho^{**}(E - B_F - \varepsilon) d\varepsilon \qquad (17)$$

$$= \frac{T}{2\pi\rho(E)} \sqrt{\frac{\pi T}{b}} \rho^{**}(E - B_F) = \frac{T}{2\pi\rho(E)} \rho^{*}(E - B_F) . \qquad (18)$$

These results allow us to make qualitative predictions on the shape of the mass/charge distributions. Equation 13 can be further simplified as follows:

$$\Gamma_Z \propto \frac{\rho^{**}[E - B(Z)]}{\rho(E)} \propto e^{-B(Z)/T_Z} \qquad (19)$$

where T_Z represents the nuclear temperature calculated at an excitation energy

$$E_x = E - B(Z) = aT_Z^2 . \qquad (20)$$

This means that the mass or charge yield mirrors the ridge line, being characterized by high emission probabilities in the regions of low potential energy and vice-versa. This is illustrated in Fig. 1 for two systems, one below the Businaro-Gallone point, and the second above it. In the former case, the yield has a characteristic U-shape, where the light wing is associated with very light particle emission, and the complementary heavy wing with the corresponding evaporation residues. In the latter case, besides the light and heavy wings observed in the former case, one observes also a peak at symmetry which becomes more and more prominent with increasing fissility parameter x, and which can be identified as the fission peak.

In the limit in which the conditional saddle and scission points can be considered degenerate, one can also develop a theory of the complex-fragment kinetic energy and angular distributions.

2.4. - *Multifragmentation and Nuclear Comminution.* - The previous discussion illustrates the emission of complex fragments through binary CN decay. If there is enough excitation energy

available, the primary binary-decay products are also very excited and have a significant probability of decaying in turn into two fragments. In this very conventional way, one can foresee the possibility of several fragments in the exit channel (multifragmentation), due to several sequential binary decays. At high energies, these multifragment events may be responsible for a substantial background to other predicted multifragmentation mechanisms.

This process of sequential binary decay, controlled at each stage by the CN branching ratios, we call "nuclear comminution".[23] The limitations of this process are of two kinds: extrinsic and intrinsic.

The most obvious extrinsic limitation is the ability of the system to form a CN. In other words, the relaxation times associated with the CN formation may be too long when compared to the dynamical times leading the system to a different fate. Limitations of this sort are of course shared by all other multifragmentation modes involving an intermediate relaxed system.

The intrinsic limitations are associated with the aspect of sequentiality. Should two sequential binary decays occur too close in space-time, they would interact to an extent incompatible with the definition of sequentiality. In this case one may be led to favor models in which fragments are formed simultaneously. Nonetheless, it may be possible to extend the sequential binary model to situations in which the interaction between two successive decays is only strong enough to perturb the angular distributions. The decay probabilities are overwhelmingly affected by the level densities of the corresponding final states. These level densities arise almost completely from the intrinsic degrees of freedom. The collective degrees of freedom on which the angular distributions depend hardly contribute to the level densities. Therefore, one can observe a multifragment pattern, whose branching ratios are still clearly binary, while the angular distributions may be substantially perturbed.

The lesson to be learned from these considerations is that the best way to establish the underlying mechanism of a multifragmentation process is to study the excitation functions of binary, ternary, and quaternary events, which of course reflect the energy dependence of the branching ratios, and not to be troubled too much, should the angular distributions indicate multifragment interaction.

The calculations of the resulting mass distributions are trivial, although tedious and time consuming. We have tried to simulate the process by assuming a potential energy curve vs mass asymmetry (ridge line) with a maximum value of 40 MeV for symmetry and 8 MeV for the extreme asymmetries. The primary yield curve is taken to be of the form:

$$Y(A) = K \exp[-V(A)/T(A)]. \quad (21)$$

Each of the resulting fragments is assumed to have a similar ridge line, a properly scaled temperature, and is allowed to decay accordingly, until all the excitation energy is exhausted. For a series of initial excitation energies, the resulting mass distributions are shown in Fig. 2. The log-log plots show an exquisite power-law dependence for the low mass fragments. At excitation energies of about 400 MeV, the exponent (see Fig. 3) is around 2.3 - 2.4 which, incidentally, is very close to the value expected for the liquid-vapor phase transition at the critical temperature. This result shows that a power-law dependence is not a unique diagnostic feature of liquid-vapor equilibrium, but rather is an apparently "generic" property arising even from sequential-binay decay or comminution. A more realistic calculation with the statistical code GEMINI[13] leads to similar results.[23]

The code GEMINI generates complete events on the basis of standard CN branching ratios. Examples of events with three and four complex fragments plus a multitude of lighter particles are illustrated in Figs. 4a & 4b. Of course, the analysis of individual complete events does not

reveal the "statistical" nature of the branching ratios. Little can be said concerning the fact that the first "binary" decay is in one case occuring at the beginning of the cascade and in another quite late in the cascade after the emission of a multitude of light particles. Nor is the selection of these "particular" events among a plethora of ordinary binary decays conducive to an appreciation of the underlying statistical processes. These can be appreciated more directly in the excitation functions for events with one, two, three, etc. fragments in the exit channel, like those plotted in Fig. 5. Here one can get, at a glance, a "qualitative" feeling of the statistical competition beside the direct quantitative predictions. In view of the uncertainies in the barriers used in the calculations, plus the fact that the temperature dependence of the barriers themselves has not been included, the qualitative dependence of the branching ratios upon energy may be the most important lesson to be derived from this exercise.

2.5 - *Gamma, Pion, and Antiproton Emission* - The γ-ray decay rate can be written down quite easily in terms of the inverse (absorption) cross section and the photon phase space. The probability of emission of a photon of energy ε_γ is

$$P(\varepsilon_\gamma) = \frac{\Gamma(\varepsilon_\gamma)}{\hbar} = \frac{8\pi}{c^3 h^3 \rho(E)} \sigma(\varepsilon_\gamma)\, \rho(E - \varepsilon_\gamma)\, \varepsilon_\gamma^2 \tag{22}$$

$$\approx \frac{8\pi}{c^3 h^3} \sigma(\varepsilon_\gamma)\, \varepsilon_\gamma^2\, e^{-\varepsilon_\gamma / T}. \tag{23}$$

The inverse cross section is fairly well known experimentally. In the energy region below 20 MeV, it is dominated by the giant dipole resonance while, above that energy the quasi-deuteron mechanism prevails.

Similarly, the thermal emission of fancier particles can be written down just as easily. For instance for the pion evaporation we can write:

$$\Gamma_\pi(\varepsilon) = \frac{1}{2\pi\rho(E)} \frac{8\pi m_\pi \sigma_\pi}{h^2} \varepsilon \rho(E - m_\pi - \varepsilon) \tag{24}$$

where m_π, ε are the pion mass and kinetic energy, respectively, σ_π the inverse cross section and the other quantities are the same as in the previous equations.

The integrated cross section is:

$$\Gamma_\pi = \frac{T^2 8\pi m_\pi}{2\pi\rho(E)} \frac{\sigma_\pi \rho(E - m_\pi)}{h^2} \approx \frac{4T^2 m_\pi \sigma_\pi e^{-m_\pi/T}}{h^2} . \tag{25}$$

For any other particle, one can use the same equations, provided that the proper spin degeneracies are taken into account. Attention must be paid to the case in which a particle must be produced with its own antiparticle.

A rather spectacular example[24] of the exponential dependence predicted by Eq. 25 is shown in Fig. 6. In this figure the invariant cross section for the production π^-, K^+, K^- and $\bar{p}$ for the reaction $^{28}Si + ^{28}Si$ at 2.0 Gev/u is plotted as a function of the threshold energy (E_{thres}) plus center-of-mass (c.m.) kinetic energy ($KE_{c.m.}$). The exponential dependence is seen to extend over almost nine orders of magnitude with an effective temperature of ~ 87 MeV. As to the meaning of this result, the best comment may well be a prudent silence. Yet the temptation of saying that a rather extended source with T ~ 87 MeV is responsible for the emission of all those particles is easy to succumb to.

3. - Two or More Fragments in Equilibrium.

Although it may not be easy to determine whether, how (and where!), a system may have achieved equilibrium, it is nonetheless a useful exercise to calculate some relevant distributions

which may be used as minimal hypotheses in the analysis of an experiment.

We are going to consider here three kinds of equilibria which have been discussed in the literature with some degree of attention: 1) the chemical equilibrium; 2) the thermal equilibrium; and 3) the angular momentum equilibrium.

3.1. *The Chemical Equilibrium.* - A fundamental problem in nuclear physics is the aggregation of nucleons to form nuclei. An associated question is the relative abundance of nuclei of any given size. Statistical mechanics shows us how to calculate equilibria of the general kind:

$$aA + bB + cC + ... \leftrightarrow \ell L + mM + nN + ... \tag{26}$$

or

$$\Sigma\, a_i I = 0. \tag{27}$$

For a system at equilibrium, the free energy F must be a minimum with respect to an infinitesimal displacement $\delta\lambda$ along the reaction coordinate λ defined by:

$$dN_i = a_i\, d\lambda. \tag{28}$$

Therefore

$$dF = (\Sigma\, a_i\, \mu_i)\, d\lambda = 0 \tag{29}$$

or

$$\Sigma\, a_i\, \mu_i = 0, \tag{30}$$

where μ_i are the chemical potentials of the ith species, that can be written as

$$\mu_i = -T \ln q_i/N_i \tag{31}$$

where again q_i is the partition function of the i th component. Substituting, one obtains

$$\sum \ln \left[\frac{q}{N_i} \right]^{a_i} = 0 \tag{32}$$

or

$$\frac{N_\ell^\ell N_m^m \cdots}{N_a^a N_b^b \cdots} = \frac{q_\ell^\ell q_m^m}{q_a^a q_b^b \cdots} . \tag{33}$$

As an example, let us calculate the equilibrium:

$$p + n = d. \tag{34}$$

For this we need the three partition functions: $q_p \approx q_n$, q_d. Assuming for the moment that we are dealing with classical ideal behaviour:

$$q_n \sim q_p = 2\left[\frac{2\pi m_n T}{h^2} \right]^{3/2} V; \quad q_d = 3\left[\frac{2\pi m_d T}{h^2} \right]^{3/2} V e^{+\Delta/T} \tag{35}$$

where $\Delta = 2.2$ MeV is the deuteron binding energy,

$$\frac{N_D}{N_p N_n} = \frac{3}{4}\left[\frac{h^2}{\pi m_n T} \right]^{3/2} \frac{e^{\Delta/T}}{V}; \quad \frac{N_D}{N_p} = \frac{3N_n}{4V}\left[\frac{h^2}{\pi m_n T} \right]^{3/2} e^{\Delta/T} . \tag{36}$$

This shows that for any finite volume there will be no deuterons at high temperature, but also, and perhaps more surprising, that, at any non-zero temperature, there will be no deuterons at high dilutions when $V \to \infty$. We have here, the first lesson to be learnt. If there is any chemical equilibrium at all in any nuclear reaction, it is certainly not an equilibrium at infinite dilution. At best it is an equilibirum that is established at some freeze-out volume. After that, one must assume that the product distribution remains unaltered as the system keeps expanding. Thus the freeze-out volume, or the freeze-out concentration become inherent parameters of this kind of theory.

A similar exercise can be performed for the reaction

$$2n + 2p \leftrightarrow {}^4He. \tag{37}$$

The following ratio is easily calculated

$$\frac{N_\alpha}{N_D} = \frac{2^{2/3}}{12}\,\frac{N_p N_n}{V^2}\left[\frac{2\pi m_n T}{h^2}\right]^{-3/2} e^{(\Delta_\alpha - \Delta_D)/T} \tag{38}$$

which, incidentally can be used to determine the freeze-out concentration after the big bang.

The problem of nucleation in a nuclear vapor near saturation and/or criticality may be of potential interest. The average nucleon-nucleon interaction is composed of a very short range repulsive core and of a short range attractive part. In this it mimics the Van der Waals force between monoatomic gases which leads to the homonymous equation of state. In fact Fermi-Thomas[25-27] and Hartree-Fock calculations[28-30] for nuclear matter lead to isotherms which are quite similar to those of the Van der Waals equation. In particular, there is a critical isotherm along which the two phases, liquid and vapor, identified through the Maxwell construction, lose their identity.

It is well known that, at the critical point, density fluctuations acquire infinite range, and manifest themselves through the spectacular phenomenon of critical opalescence. The distribution in cluster size can be derived in the following simple way.[31,32] The whole gas or vapor is an imperfect gas, but can also be considered as an ideal gas mixture of clusters in equilibrium with each other. The condition of equilibrium between clusters of different size is:

$$\mu_j = j\mu \tag{39}$$

where μ_j is the chemical potential of the clusters of size j and μ is the chemical potential of the clusters of size one.

Let J_j be the partition function of a cluster of size j. Then the partition function A_j of the m_j clusters of size j is:

$$A_j = \frac{1}{m_j!} J_j^{m_j} \tag{40}$$

and the total partition function is:

$$Q = \Pi_j A_j. \tag{41}$$

The chemical potentials are:

$$-\frac{\mu_j}{T} = \frac{\partial \ln A_j}{\partial m_j} = \ln J_j - \ln m_j \tag{42}$$

and

$$m_j = J_j e^{\frac{j\mu}{T}}. \tag{43}$$

The free energy of a cluster can be written as:

$$F_j = -T \ln J_j = j\mu_L + cj^{2/3} \tag{44}$$

where μ_L is the chemical potential of the liquid and the term in $j^{2/3}$ is a surface contribution which takes care of the finite size of the cluster. By substitution in Eq. 42 we obtain:

$$m_j = y^j e^{-cj^{2/3}/T} \tag{45}$$

where

$$y = e^{\frac{(\mu-\mu_L)}{T}} \tag{46}$$

or

$$m_j = y^j x^{j^{2/3}} \tag{47}$$

where

$$x = e^{-c/T}. \tag{48}$$

Below the critical temperature and when the gas phase is stable $\mu < \mu_L$, $y < 1$, the contribution of

large clusters is exponentially unimportant. On the other hand, if the liquid phase is stable, then $\mu \geq \mu_L$ and the vapor is supersaturated. In this case the first factor increases with j and the second decreases with j. Therefore there is a value of j for which m_j is a minimum. This is given by

$$\frac{d \ln m_j}{dj} = 0 \tag{49}$$

or

$$\ln y = \frac{2c}{3Tj^{*1/3}} . \tag{50}$$

Clusters of this size represent a maximum in free energy. Thus the size j^* defined by Eq. 50 represents a hurdle to be overcome before entering the region of runaway condensation.

At the critical temperature, y = 1 and x = 1 (the latter because the surface-energy coefficient c in Eq. 44 goes to zero at the critical temperature where no distinction exists between liquid and vapor). Eq. 45 would then predict a constant distribution in m_j. However, it has been pointed out[33] that in Eq. 45 the factor y^j should be multiplied by a quantity a(j) such that a(j) is of order j and ln a(j) is of the order ln j. This factor, that arises from the energy independent statistical weight of the cluster of size j, has been estimated[34,35] to be of the form $j^{-\tau}$ where τ is a critical exponent which depends on the dimensionality of the cluster. Then, revision of Eq. 45 gives:

$$m_j = m_0 j^{-\tau} x^{j^{2/3}} y^j . \tag{51}$$

At the critical temperature the cluster distribution assumes a power law:

$$m_j \propto j^{-\tau} . \tag{52}$$

It is this power-law distribution that some authors believed to have identified, in a variety of inclusive experiments.

The finite nuclear size and the role of the Coulomb interactions,[36,37] not to speak of the shell

structure of the individual fragments set serious limitations to the applicability of the liquid-vapor equilibrium theory.

Several authors[38-44] have taken up these problems with a different emphasis. The general approach is to assume a critical freeze-out volume within which a chemical equilibrium between all the possible fragments is established. It is in this chemical equilibrium aspect that these theories differ somewhat from the lower-energy transition-state theory. The latter does not require that chemical equilibrium is established, rather it approximates the decay rate with the phase-space flux across a hyper surface perpendicular to a previously identified reaction coordinate, located at a point where multiple crossing of phase-space trajectories is expected to be at a minimum. The presence of a saddle point leading to a binary decay provides a natural setting for the application of the transition-state theory. Unfortunately, no ternary- or quaternary-saddle points have been found that could provide a similar setting for multifragmentation. Consequently, all of these theories must require a "deus ex machina" that somehow guarantees statistical-chemical equilibrium at some stage that cannot be characterized within the theory itself.

Some attempt has been made recently[45] to represent nuclear fragmentation in terms of percolation theories. In this approach the nucleus is imagined to be composed of nucleons located in a crystal lattice. In a cold nucleus all the sites are occupied. In an excited nucleus one can define an average probability $p \leq 1$ that the lattice sites are occupied. Depending on the value of p, one observes connected clusters of nucleons which are assumed to be the observed fragments. For an infinite system there is a critical value of p above which a cluster extending throughout the system exists (percolating cluster). In a nucleus one can similarly define a critical value of p above which one major fragment is formed and below which many fragments are produced. The similarity of this result with the behavior of systems exhibiting 2nd order phase transitions, like liquid-vapor

systems at the critical temperature, has led to the use of percolation theories to model these transitions. The mass distributions of the clusters near the percolation threshold is given, not surprising, by a power law. Thus it seems that the predictive potential of percolation theories is limited to very generic statistical properties, which are associated with many other models as well. Nonetheless, the analysis of the experimental (and theoretical!) distributions by means of the percolation theory may be of some benefit in helping to discriminate between generic and specific properties of these distributions.

3.2. *Statistical Shattering.* - A bold, different assumption has been proposed by Aichelin and Hüfner[46]. They envisage a brittle kind of nuclei that shatter under a sufficiently hard impact like two glass balls thrown at each other. The physics of shattering of fragile material, let alone nuclei, is poorly understood. However, it has been found empirically that the resulting distribution of fragments, or shards is rather simple, approaching a power-law dependence on the fragment size. The same authors proposed to derive such a distribution from a maximum likelihood or minimum bias principle. Sobotka and Moretto[47] showed that their formulation corresponds to a saddle-point approximation to the Euler problem of number partition (i.e. all the possible ways in which an integer A can be split into integers under the constraint that their sum be A). Incidentally, these partitions multiplied by a temperature-dependent statistical weight, appear also in some of the statistical multifragmentation theories.[38-40]

Despite the lack of theoretical justification for such an ansatz, it is interesting to speculate further on possible improvements which could accomodate a modicum of physical input.

3.3. *The Role of Surface in Nuclear Shattering.* - Among the many shortcomings of this approach

is its lack of an energy dependence and its inability to connect the mass distributions to other observables. A possible way to introduce an energy dependence in this problem is suggested by the fact that it takes energy to produce the extra surface associated with fragment formation. In what follows, a way is shown to evaluate the mass distribution with the constraint of a fixed amount of generated surface.[48]

Similarly to Aichelin,[46] we define a probability P(m,a) of producing a fragment of mass a with multiplicity m. The constraints are:

$$\sum_m P(m,a) = 1 \tag{53}$$

for each a,

$$\sum_m \sum_a ma\, P(m,a) = N, \tag{54}$$

N being the mass of the object being fragmented, and

$$\sum_m \sum_a kma^{2/3} P(m,a) = S, \tag{55}$$

S being the surface produced. The information I, associated with P modified by the constraints is:

$$I = \sum_m \sum_a P(m,a) \ln P(m,a) - K(a) P(m,a) + Dma\, P(m,a) + Ama^{2/3} P(m,a) \tag{56}$$

where K(a), D, and A arise from the introduction of the constraints.

Minimization of the information I gives

$$P(m,a) = e^{[K(a)-1]}\, e^{[-m(Da + Aa^{2/3})]} = C(a)\, e^{[-m(Da + Aa^{2/3})]}. \tag{57}$$

Applying Eqs. 53, 54 and 55 to Eq. 57, one obtains:

$$C(a) = 1 - e^{-(Da + Aa^{2/3})} \tag{58}$$

$$\sum_a \frac{a}{\exp\,[Da + Aa^{2/3}] - 1} = N \tag{59}$$

$$k \sum_a \frac{a^{2/3}}{\exp [Da + Aa^{2/3}] - 1} = S. \tag{60}$$

Summing P(m,a) over m one has:

$$P(a) = \frac{1}{\exp [Da + Aa^{2/3}] - 1} . \tag{61}$$

By solving Eqs. 59 and 60 simultaneously for D and A and substituting the values so obtained in Eq. 61, one arrives at the desired distribution. If no restriction is imposed upon the surface, then A = 0, which defines the unconstrained surface S_0. If a restriction is imposed by fixing S near S_0 one can linearize the problem and obtain an analytical result:

$$\Delta A = \frac{\Gamma(5/3)\zeta(5/3)}{\left[-4/3\, \Gamma(4/3)\zeta(4/3) + \left\{ \frac{[5/3\, \Gamma(5/3)\zeta(5/3)]^2}{2\Gamma(2)\zeta(2)} \right\} \right]} \frac{D_0^{2/3} \Delta S}{S_0} \tag{62}$$

$$\Delta D = - \frac{\Delta A\, 5/3\, \Gamma(5/3)\zeta(5/3)}{2\Gamma(2)\zeta(2)} \tag{63}$$

$$D_0 = \sqrt{\frac{\zeta(2)}{N}} . \tag{64}$$

Numerically, one has

$$\Delta A = - \frac{1.618305\, D_0^{2/3} \Delta S}{S_0} \tag{65}$$

$$\Delta D = -0.971156\, \Delta A \tag{66}$$

$$D_0 = \frac{1.2825}{\sqrt{N}} . \tag{67}$$

As an example, Fig. 7 shows the resulting mass distribution assuming N = 200. The three curves correspond to $\Delta S/S_0 = 0 ; 0.2 ; -0.2$. One can readily see that, by requiring more surface area, one favors the formation of light fragments and by requiring less surface area one enhances the production of heavy fragments.

Lastly, it remains to be established how much energy is invested in surface production in any given reaction. This may not be easy to determine. However, it may be possible to infer that from the determination of the total fragment kinetic energy in the center of mass of the fragmenting nucleus. If the virial theorem can be applied, then a relation should exist between the average total kinetic energy and the average potential energy which is approximately proportional to the average produced surface.

3.4. *Thermal Equilibrium, or the Energy Partition Between Fragments.* - The most trivial case is, of course, that of two fragments in contact. For a given total energy E we can define a partition by giving an amount of energy x to one fragment and the complementary energy E - x to the other.

The statistical weight for this partition is:

$$P(x) \propto \rho_1 (x)\, \rho_2 (E - x) \tag{68}$$

where ρ_1, ρ_2 are the level densities associated with the two fragments. We can approximate the distribution as a Gaussian, in other words we can expand the logarithm of P up to second order about the maximum x_o:

$$\ln P = \ln \rho_1 (x) + \ln \rho_1 (E - x) = - (x - x_o)^2/2\sigma^2 . \tag{69}$$

The maximum probability is defined as:

$$\frac{\partial \ln P}{\partial x} = \frac{\partial \ln \rho_1}{\partial x} + \frac{\partial \ln \rho_2}{\partial x} = 0 \tag{70}$$

or

$$\frac{\partial S_1}{\partial E_1} - \frac{\partial S_2}{\partial E_2} = 0; \quad \frac{1}{T_1} - \frac{1}{T_2} = 0 \tag{71}$$

$$T_1 = T_2 \tag{72}$$

where we have used $\ln \rho = S$ and $\partial S/\partial E = 1/T$.

Thus the parameter characterizing the equilibrium between the fragments is their common temperature. If the specific heat of the nuclear stuff is the same in both fragments, the energy of each fragment is, on the average, proportional to its mass

$$\frac{x_0}{E - x_0} = \frac{A_1}{A_2} . \tag{73}$$

The fluctuations are easy to calculate

$$-\frac{1}{\sigma^2} = -\left[\frac{\partial\, 1/T_1}{\partial x} - \frac{\partial\, 1/T_2}{\partial x}\right] = \frac{1}{T^2}\left[\frac{1}{c_1} + \frac{1}{c_2}\right] \tag{74}$$

or

$$\sigma^2 = T^2 \frac{c_1 c_2}{c_1 + c_2} , \tag{75}$$

where c_1, c_2 are the heat capacities of the fragments. For a Fermi gas nucleus $c = 2aT$, so

$$\sigma^2 = 2T^3\, a_1 a_2/(a_1 + a_2) \qquad (a \approx A/8). \tag{76}$$

This shows that the fluctuations are largest when the two fragments are equal. It is also obvious that the fluctuations are fully anticorrelated, because of energy conservation. Furthermore, the fluctuations are typically rather large because the fragments are rather small and obey the Fermi

statistics.

The generalization to more than one fragment is almost straightforward. A partition is defined by:

$$E = x_i + x_2 + x_3 \ldots = \Sigma x_i. \tag{77}$$

Its probability is:

$$P(x_i) \propto \rho_1(x_1)\, \rho_2(x_2) \ldots\ldots = \Pi\, \rho(x_i). \tag{78}$$

The maximum probability can be obtained by searching for the stationary point with respect to variations in the x_i 's with the constraint:

$$E = \Sigma x_i. \tag{79}$$

In order to do that, we introduce the auxiliary distribution:

$$P'(x_1) = P(x_i) \exp[\, -\beta \Sigma x_i] \tag{80}$$

or

$$\ln P'(x) = \Sigma \ln \rho(x_i) - \beta \Sigma x_i \ . \tag{81}$$

The maximum is given by:

$$\frac{\partial \ln P'(x_i)}{\partial x_i} = 0 \qquad \text{or} \qquad \frac{\partial \ln \rho(x_i)}{\partial x_i} - \beta = 0\,, \tag{82}$$

which can be written as:

$$1/T_i = \beta = 1/T \qquad \text{or} \qquad T_i = T. \tag{83}$$

In other words, all the fragments are at the same temperature $T = 1/\beta$, which can be defined as the temperature of the system.

The most probable fragment excitation energy is then approximately proportional to its mass.

For the fluctuations, one can proceed by taking the second derivative to obtain:

$$\sigma^2_i = T^2 c_i. \tag{84}$$

If the fragments are many, the fluctuations are approximately uncorrelated.

3.5. *Angular Momentum Equilibrium.* - Because of the vectorial nature of angular momentum, the thermodynamic description is somewhat more complicated. We begin with the problem of two spherical fragments, which we shall generalize later to the case of many fragments.

3.5a. *The Dinuclear System: Its Degrees of Freedom and Statistical Mechanics.* - If the nucleus at the saddle point (or for that matter, at the scission point) is considered as a single rigid body, it can be characterized by a total of six degrees of freedom: three translational modes associated with the motion of the center of mass, and three rotational modes. Furthermore, if the nucleus is axially symmetric, as it is commonly assumed, the three rotational degrees of freedom can be reduced to a rotation about the symmetry axis, plus a (doubly degenerate) rotation about an axis perpendicular to the symmetry axis. This requires that the component K of the angular momentum along the symmetry axis be a constant of motion. Thus, the angle between the angular momentum and the symmetry axis is conserved; because of its relevance, such an angle is called the "tilting" angle.

The experimental measurements of fragment angular momentum[49-58], and its alignment, suggest that the rigid body condition must be relaxed, and that intrinsic angular-momentum-bearing modes characteristic of a dinuclear system[59] must be introduced. These modes are easily visualized for a symmetric dinuclear system constituted by two equal spheres in contact[60], although the generalization to an asymmetric system of two touching, unequal spheroids is rather straightforward.

The enumeration of the degrees of freedom of a dinuclear system is immediate: two rigid bodies require 6+6 = 12 degrees of freedom. The condition of contact removes one, which leaves eleven. Of these, three are translational degrees of freedom, so there are eight angular-momentum-bearing modes left. Of these, three are associated with the "rigid" rotation of the dinuclear system. The remaining five degrees of freedom are "intrinsic" angular-momentum-bearing modes. These modes are associated with rotations of one nucleus with respect to the other in such a way that the whole system need not carry a net amount of angular momentum. The five normal modes (plus the tilting mode) are illustrated in Figure 8. They are: two degenerate "bending" modes, two degenerate "wriggling" modes and one "twisting" mode. These names have been chosen to correspond with the normal modes at the saddle point as described by Nix[19,61,62], although the correspondence is not completely obvious.

The bending mode consists in the rotation of one sphere about an axis perpendicular to the symmetry axis, and in the corresponding *counterrotation* of the other sphere. This mode is doubly degenerate.

The twisting mode consists in the rotation of one sphere about the symmetry axis, and in the corresponding *counterrotation* of the other sphere. This mode is not degenerate.

The wriggling mode is somewhat more complicated. Both spheres *corotate* about parallel axes perpendicular to the symmetry axis, and simultaneously *counterrevolve* about each other about an axis parallel to the rotation axes. This mode is doubly degenerate.

In the bending and twisting modes, the spin of one sphere is compensated by that of the other, so that the net angular momentum is always zero. In the wriggling modes, the spins of the two spheres are equal and parallel, and they are exactly compensated by the orbital angular momentum associated with the revolution which is antiparallel to the fragment spins. Therefore, the excitation

of the bending and twisting modes produces fragment spins which are antiparallel, while the excitation of the wriggling (and tilting) modes produces fragment spins that are parallel.

3.5b. *Statistical Coupling Between Orbital and Intrinsic Angular Momenta: The Wriggling Modes.* As we have mentioned above, the coupling between orbital and intrinsic angular momentum is mediated by one wriggling mode. This is illustrated in Figure 9 where it is shown that the addition of orbital motion to an excited wriggling mode leads to a decrease of the orbital and to an increase of the intrinsic angular momentum. If the total angular momentum is I and the fragment spin is s, the energy for an arbitrary partition between orbital and intrinsic angular momentum is:

$$E(s) = \frac{(I-2s)^2}{2\mu r^2} + \frac{2s^2}{2\Im} = \left[\frac{2}{\mu r^2} + \frac{1}{\Im}\right] s^2 - \frac{2I}{\mu r^2} s + \frac{I^2}{2\mu r^2} . \tag{85}$$

The first term is the orbital and the second is the intrinsic rotational energy, $\Im$ being the moment of inertia of one of the two equal spheres. The partition function is:

$$Z \propto \int e^{-E(s)/T}\, ds = \sqrt{\frac{\pi \mu r^2 \Im T}{2\Im + \mu r^2}}\, \exp\left[-\frac{I^2}{2T(2\Im + \mu r^2)}\right] . \tag{86}$$

The average spin for both fragments is given by:

$$2\bar{s} = \frac{2\int s\, e^{-E(s)/T}\, ds}{Z} = \frac{2\Im}{\mu r^2 + 2\Im} I = \frac{2}{7} I = 2 I_R . \tag{87}$$

This is, of course, the rigid-rotation limit. The second moment s^2 is given by:

$$4\overline{s^2} = \frac{2\mu r^2 \Im T}{\mu r^2 + 2\Im} + \frac{4 I^2 \Im^2}{(\mu r^2 + 2\Im)^2} . \tag{88}$$

From this we obtain the standard deviation:

$$4\sigma_s^2 = \frac{2\Im \mu r^2 T}{\mu r^2 + 2\Im} = \frac{10}{7} \Im T . \tag{89}$$

The result in Eq. 87 is temperature independent, as one should expect from the fact that Eg. 85 is quadratic in s. This result could be obtained by solving the equation:

$$\frac{dE}{ds} = 0 . \tag{90}$$

This result corresponds to the mechanical limit of *rigid rotation* when the orbital and the intrinsic angular velocities are matched.

The result in Eq. 89 could have been obtained also by appreciating that the thermal fluctuations about the average in Eq. 87 are controlled by the second derivative of Eq. 85 at the minimum, or:

$$4\,\sigma_s^2 = 4\,T/b \tag{91}$$

where:

$$b = \left[\frac{\partial^2 E}{\partial s^2}\right]_{\bar{s}} . \tag{92}$$

In the case of $I = 0$, the fragments are still going to acquire angular momentum as shown by Eq. 89:

$$\overline{s^2} = \frac{1}{2}\,\frac{\mu r^2 \Im\, T}{\mu r^2 + 2\Im} = \frac{5}{14}\,\Im\, T . \tag{93}$$

Since there are *two* wriggling modes, the mean square angular momentum of each fragment is:

$$\overline{S^2} = 2\,\overline{s^2} = \frac{\mu r^2 \Im\, T}{\mu r^2 + 2\Im} = \frac{5}{7}\Im T . \tag{94}$$

3.5c. *The Bending and Twisting Modes.* - These three degrees of freedom are illustrated in Figure 8. They are degenerate in our two-equal-sphere model. A splitting of the degeneracy could easily occur in the case of fragment deformation. We shall not consider this important possibility at the moment, although it is completely trivial, because of the arbitrariness in the choice of deformation.

The partition function for these three degenerate modes can be written as:

$$Z \propto \int R^2 \; e^{-\frac{R^2}{\Im T}} \, dR \,, \qquad \ln Z = A - \frac{3}{2} \ln \frac{1}{\Im T} \tag{95}$$

from which :

$$\overline{R} = 2\sqrt{\frac{\Im T}{\pi}} \quad , \qquad \overline{R^2} = - \frac{\partial \ln Z}{\partial \left[\frac{1}{\Im T}\right]} = \frac{3}{2}\Im T \tag{96}$$

or 1/2 $\Im T$ per degree of freedom.

Notice that R is the angular momentum of *each* fragment and that, for each mode, the angular momenta of the two fragments cancel out pairwise. Furthermore, for each fragment the resulting angular momentum is randomly oriented. It is worth stressing again that, as for the wriggling modes, this angular momentum can exist even when the total angular momentum is zero because of the pairwise cancellation mentioned above.

At this point the (frequently asked) question may arise: "The bending and twisting modes in the two sphere model have no restoring force. Wouldn't the results be different if we were to introduce them?" The answer is no. Neglecting the degeneracy for the moment, the Hamiltonian would look like:

$$\mathbf{H} = \frac{R^2}{\Im} + \frac{1}{2} k \omega^2 \tag{97}$$

where ω is the conjugate angle and k is the stiffness. The partition function thus factors the kinetic and potential energy components:

$$Z = \int e^{-\frac{R^2}{\Im T}} \, dR \int e^{-\frac{k \omega^2}{2T}} \, d\omega \,. \tag{98}$$

As a consequence, any moment of R is strictly independent of the value of the stiffness k.

3.5d. *The Tilting Mode.* - This mode is unlike the other five "intrinsic" modes in the sense that it cannot confer angular momentum to the fragments, while keeping the total angular momentum equal to zero. However, we treat its statistical mechanics here because of its importance.

In their most stable configuration, the two touching fragments are aligned with their common axis perpendicular to the total angular momentum. Because of thermal fluctuations, this condition can be relaxed. If we now assume that the two fragments are rigidly attached one to the other, the energy is given by:

$$E = \frac{I^2 - K^2}{2\Im_\perp} + \frac{K^2}{2\Im_{||}} = \frac{I^2}{2\Im_\perp} + \frac{K^2}{2\Im_{eff}} \tag{99}$$

where $\Im_\perp = 2\,\Im + \mu r^2$, $\Im_{||} = 2\,\Im$ and $\Im_{eff}^{-1} = \Im_{||}^{-1} - \Im_\perp^{-1}$; K is the projection of the angular momentum I along the line of centers. The partition function is:

$$Z = \sqrt{\pi}\ \exp\left[-\frac{I^2}{2\Im_\perp T}\right] \sqrt{2\Im_{eff} T}\ \operatorname{erf}\left[\frac{I}{\sqrt{2\Im_{eff} T}}\right], \tag{100}$$

from which:

$$\overline{K^2} = \Im_{eff}\, T - \frac{I\sqrt{2\Im_{eff} T}}{\sqrt{\pi}}\ \frac{\exp\left[-\dfrac{I^2}{2\Im_{eff} T}\right]}{\operatorname{erf}\left[\dfrac{I}{\sqrt{2\Im_{eff} T}}\right]}. \tag{101}$$

For small I we have:

$$\overline{K^2} = \frac{1}{3}\, I^2\,, \tag{102}$$

while for large I we have:

$$\overline{K^2} = \Im_{eff}\, T = \frac{14}{5}\Im\, T\,. \tag{103}$$

The total fragment spin is given by:

$$2s = \sqrt{K^2 + \frac{4}{49}\left[I^2 - K^2 \right]} \tag{104}$$

and the averaged square quantity is:

$$4\,\overline{s^2} = \overline{K^2} + \frac{4}{49}I^2 - \frac{4}{49}\overline{K^2} = \frac{45}{49}\overline{K^2} + \frac{4}{49}I^2 \tag{105}$$

and for large I:

$$4\,\overline{s^2} = \frac{18}{7}\Im T + \frac{4}{49}I^2 \,. \tag{106}$$

3.5e. *Summary and Generalization to Asymmetric Dinuclear Systems.* - The overall statistical treatment of the angular-momentum-bearing modes allows us to describe the angular momentum distribution of one of the two fragments as a tridimensional Gaussian distribution in the angular momentum components I_x, I_y, I_z:

$$P(I) \propto \exp -\left[\frac{I_x^2}{2\sigma_x^2} + \frac{I_y^2}{2\sigma_y^2} + \frac{(I_z - \overline{I}_z)^2}{2\sigma_z^2} \right] , \tag{107}$$

where I_z is the rigid rotation component:

$$\overline{I}_z = \frac{\Im_i}{\mu r^2 + 2\Im_i} I = \frac{1}{7} I \tag{108}$$

for equal touching spheres, and:

$$\sigma_x^2 = \sigma_{twist}^2 + \sigma_{tilt}^2 = \frac{1}{2}\Im T + \frac{7}{10}\Im T = \frac{6}{5}\Im T \tag{109}$$

$$\sigma_y^2 = \sigma_{bend}^2 + \sigma_{wrig}^2 = \frac{1}{2}\Im T + \frac{5}{14}\Im T = \frac{6}{7}\Im T \tag{110}$$

$$\sigma_z^2 = \sigma_{bend}^2 + \sigma_{wrig}^2 = \frac{1}{2}\Im T + \frac{5}{14}\Im T = \frac{6}{7}\Im T \,. \tag{111}$$

In the case of an asymmetric system, the results are qualitatively similar. The three variances in

dimensionless units are shown in Figure 10 as a function of mass asymmetry for two touching spheres. The most remarkable feature of this figure is the rapid increase of the variance σ_x^2 with increasing asymmetry. This effect is almost exclusively due to the softening of the tilting mode. As one of the two spheres becomes smaller, the rotational-energy increase associated with an increasing projection K becomes smaller. The corresponding K_0^2 increase for the very asymmetric configurations associated with the emission of an α particle, a proton, or a neutron is responsible for the small anisotropy in the angular distributions of these particles in comparison with those for symmetric fission.

3.6. *Angular Momentum and Multifragmentation.* - Let us now consider a collision giving rise to *n* fragments. In the "expansion" phase, we assume statistical equilibrium, until beyond a critical shape, or mass distribution, the fragments decouple from each other and the equilibrium remains frozen in.

For simplicity, let us suppose that the critical shape is approximately spherical. Then, it is completely general to choose the *z* axis to coincide with the direction of the angular momentum. Also, for simplicity, let us assume that each fragment is spherical. The Hamiltonian of the system can be written as follows:

$$H = \sum H_i = \sum \left[\frac{I_x^2 + I_y^2 + I_z^2}{2\Im} + \frac{\ell_z^2}{2mr^2} + \frac{1}{2m}(p_r^2 + p_z^2) \right], \qquad (112)$$

where the sum Σ is to be carried over the fragments (the corresponding index is omitted for simplicity); I_x, I_y, and I_z are the intrinsic components of the angular momentum for a given fragment with moment of inertia $\Im$; ℓ_z is the z component of the orbital angular momentum of a

fragment of mass m and distance r from the z axis; and p_r and p_z are the other two generalized momenta for the translational motion of a fragment in cylindrical coordinates. The choice of cylindrical coordinates for the relative motion has the advantage of nicely isolating the z component of the orbital angular momentum.

The generalized grand partition function can now be calculated:

$$Z = \int \exp - \left[\sum \frac{H_i}{T} - \mu \sum (I_z + \ell_z) \right] dI_x dI_z dI_y d\ell_z dp_r dp_z , \tag{113}$$

where the constraint of the total angular momentum $I_T = \Sigma (I_z + \ell_z)$ (remember the choice of the z axis) has been introduced by means of the Lagrange multiplier μ. This guarantees that the total angular momentum will be conserved, at least on the average. More explicitly,

$$Z = \prod \int \exp \left[- \frac{I_x^2}{2\Im T} - \frac{I_y^2}{2\Im T} \right] \exp \left[- \frac{1}{2mT} (p_r^2 + p_z^2) \right] \exp - \left[\frac{I_z^2}{2\Im T} - \mu I_z \right]$$

$$x \exp - \left[\frac{\ell_z^2}{2mr^2 T} - \mu \ell_z \right] dI_x dI_y dI_z d\ell_z dp_r dp_z , \tag{114}$$

where the terms in I_z, ℓ_z have been grouped together. Integration yields

$$Z = \prod \left[\sqrt{2\Im T} \right]^2 \left[\sqrt{2mT} \right]^2 \sqrt{2\pi\Im T}\, e^{\mu^2 \Im T/2} \sqrt{2\pi mr^2 T}\, e^{\mu^2 mr^2 T/2} \tag{115}$$

or

$$\ln Z = \sum \left[\ln 2\Im T + \ln 2mT + \frac{1}{2} \ln 2\pi\Im T + \frac{\mu^2}{2} \Im T + \frac{1}{2} \ln 2\pi mr^2 T + \frac{\mu^2}{2} mr^2 T \right] . \tag{116}$$

The value of the Langrange multiplier μ is determined by the equation:

$$\frac{\partial \ln Z}{\partial \mu} = I_T = \mu \sum (\Im T + mr^2 T) \tag{117}$$

$$\mu = \frac{I_T}{T\sum(\Im + mr^2)} . \tag{118}$$

By differentiating once more with respect to μ, one obtains

$$\frac{\partial^2 \ln Z}{\partial \mu^2} = \sigma^2_{I_T} = T\sum(\Im + mr^2) . \tag{119}$$

These are the "spurious" fluctuations in I_T introduced by the grand-canonical approach and can be used to estimate the reliability of the theory in any given situation. Differentiation of the logarithm of the partition function with respect to $\beta = 1/T$ yields the total energy,

$$-\frac{\partial \ln Z}{\partial \beta} = E = \sum\frac{3}{2}T + \sum\frac{3}{2}T + \frac{\mu^2}{2}T^2\sum(\Im + mr^2) \tag{120}$$

or

$$E = \frac{3}{2}nT + \frac{3}{2}nT + \frac{I_T^2}{2\sum(\Im + mr^2)} \tag{121}$$

where n is the number of fragments, the first term refers to the intrinsic rotation energy, the second to the translational energy, and the third to the rigid rotation of the system at the critical shape. Again, the first two terms arise from the classical energy-equipartition theorem, while the third should be interpreted as the energy of a rigidly-rotating body whose moment of inertia is defined by the mass distribution associated with the critical shape. The latter is a distinctly interesting but not altogether unexpected result. It may be worth noticing for the last time how convenient the expression of the translational motion in cylindrical coordinates has turned out to be. The intrinsic spin of each fragment can also be obtained by differentiation:

$$-\frac{\partial \ln Z}{\partial(1/2\Im T)} = \bar{I}^2 = 2\Im T + \Im T + \frac{\mu^2}{4}4\Im^2T^2 \tag{122}$$

or

$$\bar{I}^2 = 3\Im T + \left[\frac{\Im}{\sum(\Im + mr^2)}\right]^2 I_T^2 . \tag{123}$$

This equation says that the fragment angular momentum arises from two contributions: the first is purely statistical and would exist also for zero angular momentum; the second is the share of the total angular momentum going to the fragment under study, dictated by the rigid-rotation condition. The two contributions are added in quadrature. From the structure of Eq. 123, one would also infer that

$$\sigma_x^2 = \sigma_y^2 = \sigma_z^2 = \Im T , \tag{124}$$

the average for I_x and I_y being zero and for I_z being

$$\bar{I}_z = \frac{\Im}{\sum(\Im + mr^2)} I_T . \tag{125}$$

The latter inference can be verified directly. By isolation of the factor containing I_z in the partition function, one has

$$Z_{I_z} = \prod \exp - \left[\frac{I_z^2}{2\Im T} - \mu I_z\right] . \tag{126}$$

Thus,

$$\bar{I}_z = \frac{\partial \ln Z_{I_z}}{\partial \mu} = \mu \Im T = \frac{\Im}{\sum(\Im + mr^2)} I_T \tag{127}$$

as expected. Consequently,

$$\sigma_x^2 = \sigma_y^2 = \sigma_x^2 = \Im T . \tag{128}$$

The results obtained so far allow us to describe the fragment-spin alignment through the relevant components of the polarization tensor:

$$P_{xy} \propto \sigma_x^2 - \sigma_y^2 = 0 , \tag{129}$$

$$P_{zz} = \frac{1}{1 + 3\frac{\sigma^2}{\bar{I}_z^2}} = \frac{1}{1 + 3\Im T\left[\frac{\Sigma(\Im + mr^2)}{\Im I_T}\right]^2} . \tag{130}$$

For small fluctuations, one has

$$P_{zz} \cong 1 - 3\Im T\left[\frac{\Sigma(\Im + mr^2)}{\Im I_T}\right]^2 . \tag{131}$$

For large fluctuations, one has

$$P_{zz} \cong \frac{1}{3\Im T}\left[\frac{\Im I_T}{\Sigma(\Im + mr^2)}\right]^2 . \tag{132}$$

The great simplicity and transparency of the above treatment is marred by the difficulty that one encounters when trying to produce some predictions. The first difficulty is associated with the evaluation of the total moment of inertia $\Sigma(\Im + mr^2)$. This is defined for the critical shape and mass distribution when the decoupling occurs. In the case of the deep-inelastic process, it was not too difficult to guess the critical shape as that of two touching fragments, either spherical or somewhat deformed. In the case of three or more fragments, the problem is much less defined; in fact, the critical shape, even for the same number of fragments, may vary dramatically in going from moderately low-energy collisions to nearly relativistic collisions. Perhaps, with some optimism, one could turn the problem around and, after having looked for good signs of thermalization (see Eq. 121 for inspiration), one might try to infer the critical shape from the observed angular momenta and polarization.

Another difficulty, which is now associated with the entrance channel, is the definition of the angular-momentum window to be considered in analyzing data within the framework of this theory. Some idea may be obtained from the elaborate analyses done for other variables in relativistic

collisions, but at lower energies it is still an unknown.

A comforting last observation arises from Eq. 123. Sizable angular momenta can still be expected even for a "central collision" for which $I_T = 0$. In fact, one might venture to guess that in many instances this will be the case, especially at the lower energy end. The angular momentum may then be directly related to the temperature which can perhaps be inferred from other observables such as the internal and translational energy of the fragments. If this were fortunately to be the case, the picture should be reasonably easy to unscramble.

4. Experimental Evidence For Statistical Decay

4.1. *Compound Nucleus Emission of Complex Fragments at Low Energies.* - In the midst of a confusing experimental situation at intermediate energies, made even less clear by a variety of theoretical claims and counterclaims, a descent to lower energies helped to clarify at least one point, namely the CN emission of complex fragments. The reaction chosen for this purpose, ^{3}He + Ag, presented several advantages.[8,64] On the one hand, the very lightness of the projectile eliminated a source of complex fragments otherwise present with heavier projectiles, namely projectile fragmentation. On the other hand, the reaction Q-value helped to introduce a good amount of excitation energy with a moderate bombarding energy.

The excitation energy of the CN ranged from 50 MeV to 130 MeV, the lower limit being barely 10 MeV above the highest barriers. Complex fragments were detected with cross sections dropping precipitously with decreasing energy. Their kinetic energy spectra resembled closely the shapes predicted by the theory illustrated above. In particular, the shapes evolved from Maxwellian-like for the lowest Z values to Gaussian-like for the highest Z values.

A very effective way to appreciate the nature of the emission and the possible source of these

fragments is to plot their invariant cross section in velocity space. The invariant cross section plots in the $v_{||}$ - $v_{\perp}$ plane shown in Fig. 11, for a variety of fragments at 70 MeV bombarding energy, demonstrate striking Coulomb rings which are the paradigms of many more to follow in the next pages. The essentially binary nature of the decay, its angular isotropy, and the extent of energy relaxation speak suggestively of CN decay. However, the crucial proof is given by the measurement of excitation functions extending down almost to the threshold. These excitation functions, shown in Fig. 12 demonstrate, with their rapid rise with increasing energy, that these fragments originate from CN decay and compete, in their emission, with the major decay channel, namely neutron emission.

The CN fits shown in the same figure, demonstrate quantitatively the agreement with the CN hypothesis, and allow one to extract the conditional barriers. The extracted barriers are presented in Fig. 13 together with two calculations.[20] The standard liquid-drop model fails dramatically in reproducing the barriers, while the finite-range model, accounting for the surface-surface interaction (so important for these highly indented conditional saddle shapes) reproduces the experimental values almost exactly. This is a most important result, since it determines with great precision crucial points in the potential-energy surface and lends confidence to a model that can be used to calculate the same potential-energy landscape. The oscillations seen in the data are bigger than the experimental errors and are believed to be due to shell effects associated with the conditional saddle shapes.

Additional studies at low energies demonstrated the role of the potential energy along the ridge line.[9] The charge distribution is U-shaped or has an additional maximum at symmetry depending on whether the system is below or above the Businaro-Gallone point. The three reactions ^{74}Ge, ^{93}Nb and ^{139}La + ^{9}Be studied at 8.5 MeV/u produce CN well below, near, and well above the

Businaro-Gallone point, respectively. The observed fragments are emitted from a source with CN velocity and are characterized by center-of-mass Coulomb-like energies. Their charge distributions are shown in Fig. 14 together with the corresponding CN calculations. As expected, the U-shaped distributions prevailing at or below the Businaro-Gallone point as exemplified by the $^{76}Ge + ^{9}Be$ and $^{93}Nb + ^{9}Be$ reactions, develop in the case of $^{139}La + ^{9}Be$ a central peak, characteristic of systems above the Businaro-Gallone point. The solid curves in the same figure represent calculations based on the CN hypothesis.

4.2. *Compound Nucleus Emission of Complex Fragments at Intermediate Energies.* - The verification of CN emission of complex fragments at low energy carries in itself the unvoidable consequence of an even more abundant emission at higher energies, provided that CN are indeed formed.

Part of the initial confusion about complex fragment emission at intermediate energies may have been due to the broad range of compound and non compound nucleus sources associated with the onset and establishment of incomplete fusion. This problem can be minimized to some extent by the choice of rather asymmetric systems. In such systems, the range of impact parameters is geometrically limited by the nuclear sizes of the reaction partners. Furthermore, the projectile-like spectator, if any, is confined to very small masses, and does not obscure other sources of complex fragments.

With this in mind, we are going to follow the CN emission of complex fragments, as well as other processes, from the lowest energies up to 50 MeV/u. The reactions studied were ^{63}Cu, ^{93}Nb, $^{139}La + ^{9}Be$, ^{12}C, ^{27}Al from 8.5 MeV/u up to 100 MeV/u.[10-16] These reactions were studied in reverse kinematics in order to facilitate the detection of fragments over most of the c.m. angular

range. The use of reverse kinematics is particularly useful because it carries a most powerful signature for binary decays producing fragments with Coulomb-like energies. Figure 15 gives an example of such a signature, as it appears on-line from the output of a ΔE-E telescope. For each atomic number, characterized by its own hyperbola, two energy components are clearly visible. The explanation of these components is given in Fig. 16. In this figure we show a schematic diagram of the invariant cross section in the $v_{\|}$ - $v_{\perp}$ plane for the CN binary emission of a given fragment. The circle represents the expected Coulomb ring associated with binary isotropic CN emission in the center of mass. The radius of the circle decreases monotonically with increasing fragment charge. A given angle in the lab system intersects each circle in two points. In other words, a given lab angle corresponds to two c.m. angles, one forward, and the other backward. This explains the two components observed in Fig. 15. As the radius of the Coulomb circle decreases, the two solutions progressively come closer together, until they coincide and eventually disappear altogether.

As can be readily seen, the presence of the two components in the ΔE-E plane suggests immediately a variety of conclusions: 1) The fragments are emitted from a source with a well defined velocity; 2) The fragments are emitted in a binary decay; 3) the fragment's Coulomb energy indicates a complete thermal relaxation characteristic of a CN decay or completely damped deep-inelastic reaction. In this sense we believe that plots like those of Fig. 15 represent a powerful signature for CN emission. As we mentioned above, reverse kinematics allows one to cover a large c.m. angular range with only a moderate coverage of lab angles. Consequently, it is possible to reconstruct invariant cross sections in the $v_{\|}$ - $v_{\perp}$ plane for each atomic number rather readily. A few examples are shown in Figs. 17 -19. For all the reactions studied so far one has observed beautifully developed Coulomb rings which indicate that, up to the highest bombarding

energies, the fragments do in fact arise from binary CN decay. Only the fragments in the neighborhood of the target atomic number show the presence of an additional component at backward angles (big foot), that can be attributed to quasi-elastic and deep-inelastic processes, and/or to the spectator target-like fragment in the incomplete fusion reactions prevailing at higher bombarding energies.

The centers of these rings provide us with the source velocities for each Z value. For a variety of reactions, these source velocities are shown in Figs. 20 & 21 as a function of the fragment's atomic number. For all bombarding energies the source velocity is independent of the fragments' Z value. Up to 18 MeV/A, one can conclude that a single source with CN velocity is responsible for the emission of all the fragments.

The radii of the Coulomb rings give the emission velocities in the center of mass. These mean velocities with their standard deviations are shown as a function of Z value in Figs. 20 & 21 for a variety of reactions. The almost linear dependence of these velocities upon fragment Z value is a clear indication of their Coulomb origin. This is also supported by their independence on bombarding energy, as shown in the same figures. The Coulomb calculations (lines), which well reproduce the data, further illustrate the degree of relaxation of the c.m. kinetic energy. The variances of the velocities arise from a variety of causes, among which the inherent Coulomb energy fluctuation due to the shape fluctuations of the "scission point", and the fragment recoil due to sequential evaporation of light particles.

4.3. *Angular Distributions.* - The most important feature of the angular distributions providing diagnostic information regarding CN emission is their symmetry about 90^{o} in the center of mass. Because of the rather large angular momenta involved in these reactions, one also expects the

angular distributions to be of the form $d\sigma/d\Omega = 1/\sin\theta$ or $d\sigma/d\theta$ = constant. In contrast, the angular distributions of projectile-like fragments and target-like fragments produced in quasi- or deep-inelastic processes should show a backward and a forward peaking, respectively.

The available data are sufficiently complete to provide information on the angular distribution of individual fragments. Some of these angular distributions are shown in Fig. 22a&b. In general, one observes angular distributions with a $1/\sin\theta$ dependence ($d\sigma/d\theta$ = constant), except in the vicinity of the target or projectile Z value where quasi-elastic, deep-inelastic and target-spectator fragments manifest themselves with a forward or backward peaking.

The backward peaking of the target-like fragment is quite visible in the case of $^{139}La + ^{12}C$ at 18 MeV/u, where it is most prominent for Z = 4,5 and vanishes for $Z \geq 10$. In the reaction $^{139}La + ^{27}Al$ at 18 MeV/u, the backward peaking extends up to Z = 16 due to the larger atomic number of the target (Z = 13). Thus the use of a higher Z target tends to mask the CN component of a larger number of products with quasi-elastic and deep-inelastic products. Substantial contributions of the quasi-elastic and deep-inelastic components at atomic numbers near that of the projectile are visible in the reaction $^{139}La + ^{27}Al$ for the highest Z-values.

4.4. *Cross Sections.* - All of the evidence presented so far for the intermediate-energy complex fragment emission points rather convincingly towards a CN process. However, the most compelling evidence for this CN mechanism lies in the statistical competition between complex fragment emission and the major decay channels, like n, p, and ^4He emission. The simplest and most direct quantity testing this hypothesis is the absolute cross section.

Absolute cross sections as a function of Z value are shown in Figs. 23 & 24. At first glance one can observe a qualitative difference between the charge distributions from the Nb-induced and

the La-induced reactions. The former distributions portray a broad minimum at symmetry whereas the latter show a broad central fission-like peak that is absent in the former distributions. This difference can be traced to the fact that the former systems are below or near the Businaro-Gallone point, while the latter systems are well above.

In general, for a given system, the cross sections associated with the charge distributions increase in magnitude rapidly at low energies, and very slowly at high energy, in a manner consistent with Eq. 19. However, the shape of the distributions is rather insensitive to the bombarding energy over the energy range explored, although one observes a flattening of the distributions with increasing bombarding energy as predicted by Eq. 19.

As was said above, the most important information associated with these cross sections is their absolute value and their energy dependence. Through them, the competition of complex fragment emission with the major decay channels, like n, p, and α decay is manifested. This is why we attribute a great deal of significance to the ability to fit such data. Examples of these fits are shown in Figs. 23&24. The calculations are performed with an evaporation code GEMINI[13] extended to incorporate complex fragment emission. Angular-momentum dependent finite-range barriers are used.[21] All the fragments produced are allowed to decay in turn both by light particle emission or by complex-fragment emission. In this way higher chance emission, as well as sequential binary emission, are accounted for. The cross section is integrated over ℓ waves up to a maximum ℓ value that provides the best fit to the experimental charge distributions. In all cases shown here, the quality of the fits is exceptionally good and the fitted values of ℓ_{max} correspond very closely to those predicted by the Bass model[66] or by the extra push model.[67] In similar reactions, but with ^{27}Al targets, the calculation falls short of the experimental cross section even when one reaches the ℓ wave at which the lowest barrier (at symmetry) goes to zero. In this case, one may have to

advocate fast fission to complement the CN emission.

These calculations allow one to evaluate the contribution to the charge distributions of the pure evaporation residues arising solely from the emission of fragments with mass $A \leq 4$. This contribution is shown in Figs. 23 & 24 by the dashed curves. One should note that for these asymmetric reactions below 20 MeV/u, evaporation residues are predicted to be the dominant products of the CN decay.

This remarkable success in reproducing the absolute charge distributions demonstrates that the CN mechanism characterized at the lowest energies dominates the picture at intermediate energies. It seems fair to say that, for atomic numbers between projectile and target, the CN mechanism accounts for all of the fragment emission, while for the remaining Z range it constitutes an important component, together with the quasi-elastic and deep-inelastic processes which are abundantly represented in this region. As we have seen, in the range of reactions considered so far, binary decay is dominant. However, it is an easy prediction that, even when we enter the energy range where ternary and higher multiplicity events dominate, the CN mechanism will account for a great deal if not all of the fragment emission through sequential-binary decay. This will be shown below.

4.5. *Coincidence Data.* - If any doubt still remains concerning the binary nature of the decay involved in complex fragment production, it can be removed by the detection of binary coincidences. Examples of Z_1 - Z_2 correlations are shown in Figs. 25 & 26. The corresponding $Z_1 + Z_2$ spectra are also shown in Fig. 27. One can observe the binary band in the Z_1 - Z_2 correlation as a general feature for all systems. The binary nature is proven by the correlation angles as well as by the sum of the fragments' atomic numbers which accounts for most of the

target + projectile charge. The missing charge can be accounted for by the extent of incomplete fusion and by the sequential evaporation of light charged particles ($A \leq 4$). A particularly interesting example of this verification is shown in Fig. 28 for the reactions $^{93}Nb + {}^{9}Be, {}^{27}Al$. In this figure, the average charge sum $Z_1 + Z_2$ is shown as a function of Z_2. The dashed lines indicate the charge of the CN obtained in an incomplete fusion process as calculated from the measured source velocities. The solid lines show the reduction in charge brought about by evaporation from the hot primary fragments formed in the binary decay. The excitation energy of the fragments was evaluated on the basis of the source velocity, which tells about the extent of incomplete fusion. The remarkable agreement of these calculations with the data, which is retained over a large range of excitation energies speaks for the internal consistency of such an analysis.

4.6. *Complex Fragment Emission at Higher Energies.* - As we have seen above, the evidence for the CN origin of complex fragments at low and intermediate energies is extensive. As the bombarding energy is increased above 18 MeV/u up to 100 MeV/u, new features come into play. First of all, incomplete fusion replaces complete fusion. Despite that, the incomplete fusion product seems to decay like a CN, so that the "binary" signature for complex fragment emission is still retained, at least for a while. In singles, the only noticeable feature due to the onset of incomplete fusion is the source velocity. The invariant cross section plots in $v_{\parallel} - v_{\perp}$ space still show well developed Coulomb rings like those shown in Figs. 17-19.

Also the coincidence data give a strong indication of "binary" decay. In Fig. 29 the $Z_1 - Z_2$ correlation diagrams are shown as they evolve from 18 MeV/u to 100 MeV/u for the reaction $^{139}La + {}^{12}C$. At 18 MeV/u the "binary" band is narrow and near the value of $Z_1 + Z_2 = Z_{Total}$. As the

bombarding energy increases, the binary band remains visible but broadens substantially and shifts to the left, indicating less and less charge associated with the "binary" event. The progessively higher abundance of events outside the "binary" band indicates the increasing presence of ternary, quaternary, etc. events. These features can be better appreciated in Fig. 30 where the $Z_1 + Z_2$ spectra are given for the same bombarding energies as in Fig. 29. The sum peak is very sharp at 18 MeV/u and close to the total charge of the CN, while it shifts down and becomes quite broad at 100 MeV/u.

While the majority of events are still binary, can they still be interpreted as due to the decay of a CN? The angular distributions shown in Fig. 31 are not symmetric about 90^o, rather they evolve very smoothly from backward to forward peaked, as the atomic number of the fragment increases. This suggests that at least part of the cross section is not purely statistical. On the other hand, Fig. 32 shows that the 90^o symmetric component of the cross section as a function of Z-value is well reproduced by the Gemini code at 50 and 80 MeV/u, and even at 100 MeV/u, except for the cross section associated with the lower atomic numbers. These very preliminary observations are very suggestive, but the exact nature of the non-equilibrium component is not clear.

At 80 and 100 MeV/u a sizeable number of ternary and quaternary events are observed. Fig. 33 shows the spectrum of the sum charge for binary, ternary and quaternary events. The astounding conclusion is that these spectra are essentially the same, as if there were only one class of objects decaying into two, or three, or four fragments. This would suggest a statistical process whereby binary, ternary and quaternary events compete statistically among each other, either in a process of sequential statistical decay or of statistical multifragmentation. Figure 34 gives the rapidity distribution of the centers of mass of binary, ternary, and quaternary events. Again, these distributions are essentially identical and reinforce the suggestions mentioned above. But this may

be a long story of which the data have given us so far but a glimpse.

5. High-Energy γ-Ray Emission

High-energy γ rays associated with intermediate-energy heavy-ion reactions were studied initially in order to observe the theoretically predicted[69,70] "coherent bremsstrahlung" associated with the collective deceleration of the two partners in the collision. Nature's lack of cooperation forced the interpretation of the data back to the less exalted "incoherent nucleon-nucleon bremsstrahlung"[69] which had at least the glamour of being associated with the entrance channel. This interpretation is probably correct in many cases. However, in reviewing the data available in the literature, we were struck by the possibility that some of the high energy γ rays could come from the excited CN present in the exit channel. Unfortunately in all of these experiments the exit channels were too poorly characterized to permit any serious analysis of this sort.

Eventually we found an experiment, ^{92}Mo + ^{92}Mo at 19.5 A MeV[71], where the exit channel was well characterized. In this reaction the two nuclei undergo a deep-inelastic collision. The dissipated energy which may amount to as much as 800 MeV (400 MeV/fragment!) is disposed of mainly by sequential light-particle emission. This emission is a true evaporation from the two deep inelastic fragments and has been studied in detail as a function of exit-channel kinetic energy.[72] At times these excited fragments emit complex fragments giving rise to a 3-body and a 4-body exit channel.[73] This emission is also statistical and is in competition with the main decay channels of n, p, and α-particle emission. This can be inferred from the probability of 3-body decay as a function of dissipated energy. All this is to prove that there are honest-to-goodness CN in the exit channel which decay as such, not only insofar as the common n, p, and α-particle channels are concerned, but also with respect to the more exotic complex fragment emission as well.

Coming back to γ rays, the experiment measured them up to E_γ = 60 MeV for 10 bins of total-kinetic-energy loss (TKEL). The ungated γ rays look very much like those measured in other reactions, which have been interpreted in terms of nucleon-nucleon bremsstrahlung. However, when these spectra are gated with different bins of TKEL, a very different picture emerges, suggesting an exit-channel rather than an entrance-channel origin.

In Fig. 35 three spectra are shown covering the TKEL range of the experiment. Notice how the high excitation energy bin is associated with the stiffest γ-ray tail while the low excitation energy bin is associated with the softest. In Fig. 36a this is shown more clearly by plotting the slope parameters vs TKEL. The square root-like dependence of these two quantities is very suggestive and one is tempted (and should be!) to interpret the slope parameter as a temperature. When, the integrated multiplicities with lower bounds of 15 and 30 MeV are plotted versus the fragment excitation energy (see Fig. 36b), they reveal a dependence typical of CN decay.

This evidence does not come totally unexpected. We know that there are two CN in the exit channel. We also know that they decay as such by light-particle emission and by complex fragment emission. Why should they not decay by γ-ray emission? Perhaps there are additional sources for the γ rays, like incoherent bremsstrahlung, etc., but we know for sure that those compound nuclei must emit γ rays. So let us calculate this emission probability. We can calculate the γ-ray decay width in an "almost" model independent way from detailed balance and the inverse cross section:

$$P(\varepsilon_\gamma) = \frac{\Gamma(\varepsilon_\gamma)}{\hbar} = \frac{8\pi}{c^2 h^3 \rho(E)} \sigma(\varepsilon_\gamma)\, \rho(E-\varepsilon_\gamma)\, \varepsilon_\gamma^2 \qquad (133)$$

$$\cong \frac{8\pi}{c^2 h^3} \sigma(\varepsilon_\gamma)\, \varepsilon_\gamma^2\, e^{-\varepsilon_\gamma/T} \,. \qquad (134)$$

The inverse cross section is fairly well known experimentally. In the low energy region between 6 - 20 MeV, it is dominated by the giant dipole resonance, while above this energy the quasideuteron

mechanism prevails. The temperature T can be calculated from the excitation energy as $E_x = aT^2$. In the actual decay, γ-ray emission competes with n, p and α-particle emissions which can be calculated in a similar fashion. In this way we can generate the "first chance" γ-ray emission probability vs. excitation energy:

$$P_\gamma(\varepsilon_\gamma) = \frac{\Gamma(\varepsilon_\gamma)}{\Gamma_T} \cong \frac{\Gamma(\varepsilon_\gamma)}{\Gamma_n + \Gamma_p + \Gamma_\alpha + \ldots.} \quad . \tag{135}$$

At this point one proceeds trivially to calculate the 2nd, 3rd etc. chance emission probability. The overall sum can be compared with experiment. In Fig. 35 we see that this calculation reproduces almost perfectly the γ-ray energy spectra from 15 MeV up to 60 MeV for all the TKEL bins, both qualitatively and quantitatively. The slope parameters of the calculated spectra can also be compared with the data. This is shown in Fig. 36a and again the fit is essentially perfect. The solid line in the figure represents the initial calculated temperature. The actual slope parameter is somewhat smaller due to the substantial presence of higher chance emission at the highest energies. Similarly the integrated γ-ray multiplicities are equally well reproduced by the calculation, (see Fig. 36b). We are left with the inescapable conclusion that all of the γ rays observed experimentally actually come from the statistical emission of the fragments. No room is left here for any other mechanism, or if anything else is there, it must be buried deep!

Somebody might object by saying, and perhaps by showing, that "other" theories fit the data almost as well and that there is no reason to choose one "theory" over another. The point is that our calculation is really no theory to speak about. We know that there are two CN in the exit channel, emitting light particles and complex fragments, because their decay products have been measured and their statistical properties verified. Therefore, we know that these CN must also emit γ rays. All we have done is to calculate, as it were, the "background" γ rays coming from CN decay. Any

other "theory" should be tested only after this "background" has been subtracted. In this case nothing noticeably above "background" seems to be visible.

5.2. *Pion Emission and Energy Fluctuations.* - It would be interesting to check how much of the π^0, $\pi^{\pm}$ production in intermediate-energy heavy-ion reactions can be explained in terms of emission from the CN present in the exit channel. Unfortunately, this will have to wait for more complete experiments, although it is an easy guess that, in certain low energy reactions, the CN contribution may not be negligible and must be evaluated.

In the case of γ-ray emission discussed above, two hot fragments are assumed to be present in the exit channel. The calculation was performed by assigning to each fragment one-half of the available energy. This may be correct on the average, but fluctuations may be present, thermal or otherwise, that may have surprising effects. In general, the role of the fluctuations in the energy distribution between two or more fragments becomes more important as the barrier or negative Q value for the decay under consideration becomes bigger. Such would be the case in pion emission where the emitter must invest an energy at least equal to the pion mass in order to emit it. Let us consider the case of two nuclei in the exit channel with mass $A_1 = A_2 = A$ and with average excitation energy $E_1 = E_2 = E$. The probability of emitting a pion is given by:

$$\frac{\Gamma_\pi}{\Gamma_n + \Gamma_p + \Gamma_\alpha + \ldots} \tag{136}$$

which is controlled by the ratio of the width Γ_π to that of the most probable channel like Γ_n.

The integrated neutron decay width can be written as:

$$\Gamma_n = \frac{2}{2\pi\rho(E)} \frac{8\pi m_n}{h^2} \sigma_n T_n^2 \rho(E - B_n) \tag{137}$$

where m_n and B_n are the neutron mass and binding energy respectively, σ_n is the inverse cross section; $\rho(E)$, $\rho(E - B_n)$ are the level densities of the CN and of the residual nucleus, respectively, and T_n is the temperature of the residual nucleus at excitation energy $E - B_n$.

The differential pion decay width is:

$$\Gamma_\pi(\varepsilon) = \frac{1}{2\pi\rho(E)} \frac{8\pi m_\pi \sigma_\pi}{h^2} \varepsilon \rho(E - m_\pi - \varepsilon) \tag{138}$$

where m_π, ε are the pion mass and kinetic energy, respectively, σ_π the inverse cross section and the other quantities are the same as in the previous equation.

For the ratio we have:

$$\frac{\Gamma_\pi(\varepsilon)}{\Gamma_n} = \frac{1}{2}\frac{m_\pi}{m_n}\frac{\sigma_\pi}{\sigma_n}\frac{1}{T_n^2}\frac{\varepsilon \rho(E - m_\pi - \varepsilon)}{\rho(E - B_n)} . \tag{139}$$

Now let us suppose that a fluctuation in the energy partition occurs such that fragment 1 has energy $E + x$ and fragment 2 has energy $E - x$. The emission probability per fragment becomes:

$$\frac{\Gamma_\pi(\varepsilon, x)}{\Gamma_n} = \frac{1}{2}\frac{\Gamma_\pi(\varepsilon)}{\Gamma_n}\left[\frac{\exp x/T_\pi}{\exp x/T_n} + \frac{\exp -x/T_\pi}{\exp -x/T_n}\right] = \frac{\Gamma_\pi(\varepsilon)}{\Gamma_n} \cosh x/T_{eff} . \tag{140}$$

where T_π is the temperature calculated for an energy $E - m_\pi - \varepsilon$ and

$$T_{eff}^{-1} = T_\pi^{-1} - T_n^{-1} . \tag{141}$$

If the fluctuations are distributed as:

$$P(x) = \frac{1}{\sqrt{2\pi\sigma^2}} \exp -x^2/2\sigma^2 , \tag{142}$$

the average emission probability becomes:

$$\frac{\overline{\Gamma_\pi(\varepsilon)}}{\Gamma_n} = \frac{\Gamma_\pi(\varepsilon)}{\Gamma_n} \frac{1}{\sqrt{2\pi\sigma^2}} \int \exp -x^2/2\sigma^2 \cosh x/T_{eff}\, dx \tag{143}$$

$$= \frac{\Gamma_\pi(\varepsilon)}{\Gamma_n} \exp \frac{\sigma^2}{2T_{eff}^2} = \frac{\Gamma_\pi(\varepsilon)}{\Gamma_n} F(\sigma, T_{eff}) \ . \tag{144}$$

For thermal fluctuations the variance is:

$$\sigma^2 = 2T^3 \frac{a_1 a_2}{a_1 + a_2}, \tag{145}$$

where T is the common temperature of the fragments before any emission has occurred, and a_1, a_2 are the level density parameters of the fragments. For a symmetric system

$$\sigma^2 = aT^3 \tag{146}$$

and

$$F = \exp \frac{aT^3}{2T_{eff}^2} \ . \tag{147}$$

In Fig. 37, we have plotted the thermal enhancement factor in pion emission as a function of the total excitation energy of the fragments. The enhancement, of course, rapidly increases with decreasing excitation energy. Similarly in Fig. 38 we have plotted the expected pion spectra if two fragments of mass A = 100 each share a total of 800 MeV excitation energy. In one case we have assumed an exact partition of the energy and in the other we have allowed for thermal energy fluctuations. The two slope parameters are quite different, the fluctuations allowing for a substantially larger spectral temperature.

The rather spectacular increase in spectral temperature appears less spectacular when one considers that its origin lies mainly in the error introduced by the sharp energy partition. Should one consider the combined system on one hand and the two fragments in contact on the other, one has the obvious equality:

$$\rho_{c.s.}(E) = \int \rho_1(x)\, \rho_2(E - x)\, dx\,, \tag{148}$$

where $\rho_{c.s.}(E)$ is the level density of the two fragments considered as one combined system. In other words the folding of the level densities of the two fragments calculated over the whole range of energy fluctuations is equal to the level density of the combined system at the fixed total energy E. This means that it does not matter if one has one, two, or more fragments in thermal equilibrium. Therefore, the spectral temperature of the pions emitted by the two fragments cannot exceed the spectral temperature that would arise if the pions were emitted by the combined system. This is true only if the energy fluctuations are thermal. If the fluctuations are dynamical in nature and larger than the corresponding thermal fluctuations, then the spectral temperature can indeed be larger than the upper limit described above.

These general consideration cast some doubts on thermal models that rely on exit channel clusterization to achieve high pion emission probabilities.

6. Conclusions

It is always preferable to draw none, but to let the audience draw their own. But if something must be said anyhow, then, in a valedictorian spirit, one could suggest that it pays to know thermodynamics and statistical mechanics. This is for two reasons, one subjective, the other objective. The first is that these disciplines are relatively easy and their application requires little specific knowledge about the system. The second is the strong penchant of Nature towards equilibrium, so that, if She is not quite there yet, She will get there pretty soon and us with Her. So cheer up! Post iucundam inventutem, post molestam senectutem, nos habebit humus!

***Acknowledgements**

This work was supported by the Director, Office of Energy Research, Office of High Energy and Nuclear Physics, Nuclear Physics Division of the U. S. Department of Energy, under contract DE-AC03-76SF00098.

References

1 V. F.Weisskopf: *Phys. Rev.*, **52**, 295 (1937).

2 V. F.Weisskopf and D. H. Ewing: *Phys. Rev.*, **57**, 472 (1940).

3 V. F.Weisskopf: *Phys. Acta*, **23**, 187 (1950).

4 V. F.Weisskopf: *Arts Sci.*, **82**, 360 (1953).

5 J. A.Wheeler: *Fast neutron physics part II* (Interscience, New York) pp. 2051 (1963).

6 L. G. Moretto: *Phys. Lett.*, **40B**, 185 (1972).

7 L. G. Moretto: *Nucl. Phys.*, **A247**, 211 (1975).

8 L. G. Sobotka, M. L. Padgett, G. J. Wozniak, G. Guarino, A. J. Pacheco, L. G. Moretto, Y. Chan, R. G. Stokstad, I. Tserruya, and S. Wald: *Phys. Rev. Lett.*, **51**, 2187 (1983).

9 L. G. Sobotka, M. A. McMahan, R. J. McDonald, C. Signarbieux, G. J. Wozniak, M. L. Padgett, J. H. Gu, Z. H. Liu, Z. Q. Yao, and L. G. Moretto: *Phys. Rev. Lett.*, **53**, 2004 (1984).

10 R. J. Charity, M. A. McMahan, D. R. Bowman, Z. H. Liu, R. J. McDonald, G. J. Wozniak, L. G. Moretto, S. Bradley, W. L. Kehoe, A. C. Mignerey, and M. N. Namboodiri: *Phys. Rev. Lett.*, **56**, 1354 (1986).

11 R. J. Charity, D. R. Bowman, Z. H. Liu, R. J. McDonald, M. A. McMahan, G. J. Wozniak, L. G. Moretto, S. Bradley, W. L. Kehoe, and A. C. Mignerey: *Nucl. Phys.*, **A476**, (1988).

12 D. R. Bowman, W. L. Kehoe, R. J. Charity, M. A. McMahan, A. Moroni, A. Bracco, S. Bradley, I. Iori, R. J. McDonald, A. C. Mignerey, L. G. Moretto, M. N. Namboodiri, and G. J. Wozniak: *Phys. Lett.*, **B189**, 282 (1987).

13 R. J. Charity, M. A. McMahan, G. J. Wozniak, R. J. McDonald, L. G. Moretto, D. G. Sarantites, L. G. Sobotka, G. Guarino, A. Pantaleo, L. Fiore, A. Gobbi, and K. D. Hildenbrand: *Nucl. Phys.*, **A483**, 371 (1988).

14 H. Y. Han, K. X. Jing, E. Plagnol, D. R. Bowman, R. J. Charity, L. Vinet, G. J. Wozniak, and L. G. Moretto: *Nucl. Phys.*, **A492**, 138 (1989).

15 E. Plagnol, L. Vinet, D. R. Bowman, Y. D. Chan, R. J. Charity, E. Chavez, S. B. Gazes, H. Han, W. L. Kehoe, M. A. McMahan, L. G. Moretto, R. G. Stokstad, and G. J. Wozniak: *Phys. Lett.*, **221**, 11 (1989).

16 R. J. Charity, N. Colonna, M. A. McMahan, G. J. Wozniak, R. J. McDonald, L. G. Moretto, G. Guarino, A. Pantaleo, L. Fiore, A. Gobbi, and K. Hildenbrand (1989), Lawrence Berkeley Laboratory preprint # LBL-26859.

17 S. Cohen, F. Plasil, and W. J. Swiatecki: *Proc. Third Conf. on Reactions Between Complex Nuclei*, ed. A. Ghiorso, R. M. Diamond and H. E. Conzett (University of California Press), pp. 325, UCRL-10775 (1963).

18 S. Cohen, F. Plasil and W. J. Swiatecki: *Ann. Phys.*, **82**, 557 (1974).

19 J. R. Nix, and W. J. Swiatecki: *Nucl. Phys.*, **71**, 1 (1965).

20 A. J. Sierk: *Phys. Rev. Lett.*, **55**, 582 (1985).

21 A. J. Sierk: *Phys. Rev.*, **C33**, 2039 (1986).

22 U. L. Businaro and S. Gallone: *Nuovo Cimento*, **1**, 1277 (1955).

23 L. G. Moretto and G. J. Wozniak: *Prog. in Part. and Nucl. Phys.*, **38**, 401 (1988).

24 A. Shor, E. F. Barasch, J. B. Carroll, T. Hallman, G. Igo, G. Kalnins, P. Kirk, G. F. Krebs, P. Lindstrom, M. A. McMahan, V. Perez-Mendez, H. Stroeher, S. Trentalange, F. J. Urban, and Z. F. Wang: (1989) to be published.

25 M. Barranco, and J. R. Buchler: *Phys. Rev.*, **C20**, 1729 (1980).

26 M. Barranco, and J. R. Buchler: *Phys. Rev.*, **C24**, 24 (1981).

27 M. Brack: *Phys. Rev. Lett.*, **53**, 119 (1984).

28 W. A. Friedmann: *Phys. Rev.*, **C27**, 569 (1983).

29 D. Q. Lamb, J. M. Lattimer, C. J. Pethick, and D. G. Ravenhall: *Nucl. Phys.*, **A360**, 459 (1981).

30 G. Sauer, H. Chandra, and U. Mosel: *Nucl. Phys.*, **A264**, 221 (1976).

31 W. Band: *J. Chem. Phys.*, **7**, 324 (1939).

32 J. Frenkel: *J. Chem. Phys.*, **7**, 200 (1939).

33 T. L. Hill: *Statistical Mechanics*, McGraw Hill Inc., pp. 149 (1956).

34 M. E. Fischer: *Phys.*, **3**, 255 (1967).

35 M. E. Fischer: *Rep. Prog. Phys.*, **67**, Vol. 30, 615 (1967).

36 P. Bonche, S. Levit, and D. Vautherin: *Nucl. Phys.*, **A436**, 265 (1985).

37 S. Levit, and P. Bonche: *Nucl. Phys.*, **A437**, 426 (1985).

38 J. P. Bondorf, R. Donangelo, I. N. Mishustin, C. J. Pethick, H. Schulz, and K. Sneppen: *Proc. of the IInd Int. Conf. on Nucleus-Nucleus Collisions* , (Visby, 1985). Contribution p. 28-29 and preprint NBI-85-3.

39 J. P. Bondorf, R. Donangelo, I. N. Mishustin, C. J. Pethick, H. Schulz, and K. Sneppen: *Nucl. Phys.*, **A443**, 321 (1985).

40 J. P. Bondorf, R. Donangelo, I. N. Mishustin, C. J. Pethick, and H. Schulz: *Nucl. Phys.*, **A444**, 460 (1985).

41 D. H. E. Gross, L. Satpathy, Ta Chung Meng, and M. Satpathy: *Z. Phys.*, **A309**, 41 (1982).

42 D. H. E. Gross: *Phys. Scr.*, **T5**, 213 (1983).

43 D. H. E. Gross: *Nucl. Phys.*, **A428**, 313c (1985).

44 J. Randrup, and S. F. Koonin: *Nucl. Phys.*, **A356**, 23 (1981).

45 X. Campi, J. Desbois, and E. Lipparini: *Proceedings XXIII Winter Meeting on Nuclear Physics* (Bormio, 1985).

46 J. Aichelin, and J. Hüfner: *Phys. Lett.*, **136B**, 15 (1984).

47 L. G. Sobotka, and L. G. Moretto: *Phys. Rev.*, **C31**, 668 (1985).

48 L. G. Moretto, and D. R. Bowman: *Proc. of the XXIV Inter. Winter Meeting of Nuclear Physics*, ed. by I. Iori, Ricerca Scientifica ed Educazione Permanente, Supplemento N. 49, pp. 126 (1986).

49 C. Lauterbach, W. Dunnweber, G. Graw, W. Hering, H. Puchta, and W. Trautmann: *Phys. Rev. Lett.*, **41**, 1774 (1978).

50 R. A. Dayras, R. G. Stokstad, C. B. Fulmer, D. C. Hensley, M. L. Halbert, R. L. Robinson, A. H. Snell, D. G. Sarantities, L. Westerberg, and J. H. Barker: *Phys. Rev. Lett.*, **42**, 697 (1979).

51 P. Aguer, R. P. Schmitt, G. J. Wozniak, D. Habs, R. M. Diamond, C. Ellegaard, D. L. Hillis, C. C. Hsu, G. J. Mathews, L.G. Moretto, G. U. Rattazzi, C. P. Roulet, and F. S. Stephens: *Phys. Rev. Lett.*, **43**, 1778 (1979).

52 M. N. Namboodiri, J. B. Natowitz, P. Kasiraj, R. Eggers, L. Adler, P. Gonthier, C. Ceruti, and S. Simon: *Phys. Rev.*, **C20**, 982 (1979).

53 H. Puchta, W. Dunnweber, W. Hering, C. Lauterbach, and W. Trautmann: *Phys. Rev. Lett.*, **43**, 623 (1979).

54 R. A. Dayras, R. G. Stokstad, D. C. Hensley, M. L. Halbert, D. G. Sarantites, L. Westerberg, and J. H. Barker: *Phys. Rev.*, **C22**, 1485 (1980).

55 R. J. Puigh, H. Doubre, A. Lazzarini, A. Seamster, R. Vandenbosch, M. S. Zisman and T. D. Thomas: *Nucl. Phys.*, **A336**, 279 (1980).

56 G. J. Wozniak, R. J. McDonald, A. J. Pacheco, C. C. Hsu, D. Morrissey, L. G. Sobotka, L. G. Moretto, S. Shih, C. Schuck, R. M. Diamond, H. Kluge, and F. S. Stephens: *Phys. Rev. Lett.*, **45**, 1081 (1980).

57 R. J. McDonald, A. J. Pacheco, G. J. Wozniak, H. H. Bolotin, and L. G. Moretto: *Nucl. Phys.*, **A373**, 54 (1982).

58 A. J. Pacheco, G. J. Wozniak, R. J. McDonald, R. M. Diamond, C. C. Hsu, L. G. Moretto, D. J. Morrissey, L. G. Sobotka, and F. S. Stephens: *Nucl. Phys.*, **A397**, 313 (1983).

59 G. Wolschin and W. Norenberg: *Phys. Rev. Lett.*, **41**, 691 (1978).

60 L. G. Moretto and R. P. Schmitt: *Phys. Rev.*, **C21**, 204 (1980).

61 J. R. Nix: *Nucl. Phys.*, **A130**, 241 (1969).

62 J. R. Nix: PhD Thesis, Report UCRL-11338, (1964) unpublished.

63 D. J. Morrissey, G. J. Wozniak, L. G. Sobotka, A. J. Pacheco, R. J. McDonald, C. C. Hsu, and L. G. Moretto: *Nucl. Phys.*, **A389**, 120 (1982).

64 M. A. McMahan, L. G. Moretto, M. L. Padgett, G.J . Wozniak, L. G. Sobotka, and M. G. Mustafa: *Phys. Rev. Lett.*, **54**, 1995 (1985).

65 V.E.Viola, B. B. Back, K. L. Wolf, T. C. Awes, C. K. Gelbke, and H. Breuer: *Phys. Rev.*, **C26**, 178 (1982).

66 R. Bass: *Nucl. Phys.*, **A231**, 45 (1974).

67 W. J. Swiatecki: *Nucl. Phys.*, **A376**, 275 (1982).

68 Bowman, D. R., thesis, LBL- (1989).

69 W. Cassing, T. Biro, U. Mosel, M. Tahyama, and W. Bauer: *Phys. Lett.*, **181B**, 217 (1986).

70 H. Nifenecker and J. P. Bondorf: *Nucl. Phys.*, **A442**, 478 (1985).

71 N. Herrmann, R. Bock, H. Emling, R. Freifelder, A. Gobbi, E. Grosse, K. D. Hildenbrand, R. Kulessa, R. Matulewicz, F. Rami, R. S. Simon, H. Stelzer, J. Wessels, P. R. Maurenzig, A. Olmi, A. A. Stefanini, w. Kühn, V. Metag, R. Novotny, M. Gnirs, D. Pelte, P. Braun-Munizinger, and L. G. Moretto: *Phys. Rev. Lett.*, **60**, 1630 (1988).

?72 K.D. Hildenbrand et al., Proc. Int. Workshop on Gross Properties of Nuclei and Nuclear Reactions XIII, Hirschegg, Austria, edited by H. Feldmeier (1985) 111.

?73 A. Olmi et al., Europhys. Lett. 4 (1987) 1121. A. Olmi, Proceedings of the 8th High Energy Heavy Ion Study (1988) 288, Lawrence Berkeley Laboratory, LBL-24580.

74 L. G. Moretto and G. J. Wozniak: *Nucl. Phys.*, **A488**, 337c (1988).

Figure Captions

Fig. 1 Schematic ridge line potentials (solid curve) and calculated yields (dashed curve) for: a) a heavy CN above the Businaro-Gallone point; and b) a light CN below the Businaro-Gallone point as a function of the mass-asymmetry coordinate (Z_{asy}).

Fig. 2 Theoretical mass distributions from comminution calculations of the deexcitation of a CN with mass 100 at several excitation energies. Notice the power-law behavior at small masses.

Fig. 3 Exponent τ of the power-law dependence as a function of excitation energy. See Fig. 2.

Fig. 4 Examples of the production of a) 4-body and b) 3-body events from the sequential decay of the compound nucleus ^{145}Eu (ℓ_{max} = 60$\hbar$) at 600 and 900 MeV excitation energy, respectively, as calculated by the statistical model code GEMINI. Evaporated neutrons and light charged particles ($Z \leq 2$) are shown by the filled and open circles, respectively. Residue nuclei and complex fragments are labelled by their mass and charge numbers.

Fig. 5 Probability of producing exactly one, two, three, four fragments a) with A>4, b) A>10 as a function of excitation energy for ^{145}Eu (ℓ_{max} = 60$\hbar$).

Fig. 6 Invariant cross sections[24] for π^-, K^-, K^+ and $\bar{p}$ production as a function of the "channel" energy $E^* = E_{thres} - KE_{c.m.}$

Fig. 7 The predicted mass distribution assuming N = 200. The three curves[48] correspond to $\Delta S/S_0 = 0; 0.2; -0.2$.

Fig. 8 *(Left)* Schematic illustrating the twisting and the doubly degenerate bending modes for a two-equal-spheres model. In each case the spin vectors of the fragments (symbolized by the shorter arrows) are of equal length but point in opposite directions. *(Right)* Schematic illustrating the tilting mode and the doubly degenerate wriggling modes for a two-equal-spheres model. The long arrows originating at the point of tangency of the two spheres represents the orbital angular momentum vectors[60].

Fig. 9 Schematic showing how the addition of orbital angular momentum (symbolized by the long arrow) to an excited wriggling mode leads to a decrease of the orbital angular momentum and an increase of the intrinsic angular momentum.

Fig. 10 The heavy fragment spin variances for a dinuclear complex are shown as a function of mass asymmetry. The variances are shown in dimensionless units after division by $\Im_{sym}T$, the moment of inertia of a mass symmetric spherical fragment times the temperature[63].

Fig. 11 Invariant cross section plots ($\sim V^{-2}\,\partial^2\sigma/\partial\Omega\partial V$) for representative ejectiles (Li, ^{9}Be, B, and C) for the reaction indicated above. The diameter of the dots is proportional to the logarithm of the cross section and the x's indicate the peak of the velocity distributions. The large arcs are sections of circles centered on the c.m. velocity (center arrow) appropriate for complete fusion. The beam direction (0^o) is indicated by the c.m. velocity vector.[8]

Fig. 12 Dependence of the total integrated cross sections (symbols) for emission of complex fragments on the center-of-mass energy, $E_{c.m.}$, in the reaction $^{3}He + ^{nat}Ag$. The curves are CN fits to the data.[64]

Fig. 13 Calculated[20] and experimental[64] conditional fission barriers as a function of the lighter fragment charge for the fission of ^{111}In. The experimental values are obtained from the fits in Fig. 12. The calculated curves for the liquid drop and Yukawa plus exponential models are shown. The dotted portions of the curves are extrapolations.

Fig. 14 Center-of mass cross sections[9] for products from the ^{74}Ge, ^{93}Nb, $^{139}La + ^{9}Be$ systems detected at $\theta_{lab} = 7.5^{o}$. The solid line is a CN calculation of the fragment yield at $\theta_{c.m.} = 30^{o}$. The arrows indicate the entrance-channel asymmetry. Data below $Z_{asy} = 0.15$ were not obtained for the $^{139}La + ^{9}Be$ system, because of the limited dynamic range of the telescope.

Fig. 15 Density plot of ΔE-E for the reaction 18 MeV/u $^{93}Nb + ^{27}Al$ for fragments detected from 4^{o} to 10^{o}. Notice the two kinetic energy components associated with each element characterized by a hyperbolic ridge in the distribution.[13]

Fig. 16 Schematic representation of reverse kinematics for the emission of a complex fragment in a CN binary decay. V_s is the lab source velocity, V_e is the Coulomb-like velocity of the fragment in the source frame, while V_a and V_b are the two velocity components at the laboratory angle θ.

Fig. 17. Contours of the experimental cross section $(\partial^2\sigma/\partial V_{\|}\partial V_{\perp})$ in the $V_{\|}$-$V_{\perp}$ plane for representative fragments detected in the reaction E/A = 12.6 MeV $^{63}Cu + ^{12}C$. The beam direction is vertical towards the top of the figure. The dashed lines show the maximum and minimum angular thresholds and the low velocity threshold of the detectors. The magnitudes of the contour levels indicated are relative.[14]

Fig. 18 Contours of the experimental cross section $(\partial^2\sigma/\partial V_{\|}\partial V_{\perp})$ in the $V_{\|}$-$V_{\perp}$ plane for representative fragments detected in the 18.0 MeV/u $^{93}Nb + ^{27}Al$ reaction.[13] See Fig. 17.

Fig. 19. Contours of the experimental cross section $(\partial^2\sigma/\partial V_{\|}\partial V_{\perp})$ in the $V_{\|}$-$V_{\perp}$ plane for representative fragments detected in the 18.0 MeV/u $^{139}La + ^{12}C$ reaction.[16]

Fig. 20 Source velocities extracted from the Coulomb velocity rings for each Z-species produced in the 12.6 MeV/u $^{63}Cu + ^{12}C$ & ^{27}Al reactions.[13] The small error bar on each point indicates the statistic error associated with the extraction process. The single large error bar for each data set indicates the possible systematic error due to the mass parameterization and energy calibrations. The velocities corresponding to the beam and complete fusion are shown as horizontal lines. In the lower portion of the figure, are shown the extracted Coulomb velocities and widths. For comparison a calculation based on the Viola systematics[65] without (dashed line) and with angular momentum effects (solid line) is shown.

Fig. 21 Source velocities extracted from the Coulomb velocity rings for each Z-species produced

in the 18.0 MeV/u $^{139}La + ^{12}C$ & ^{27}Al reactions.[16]

Fig. 22. Angular distributions ($d\sigma/d\theta$) in the source frame for representative Z values from the 14.7 &18.0 MeV/u ^{139}La + a) ^{12}C and b) ^{27}Al reactions.[16] The backward rise at low Z values is attributed to target-like and projectile-like quasi and deep inelastic products. Note that the cross sections are flat for a large range of Z values intermediate between the target and the projectile. The solid lines are to guide the eye.

Fig. 23 Angle-integrated charge distributions of complex fragments associated with fusion-like reactions of ^{93}Nb and ^{12}C at three bombarding energies.[13] The experimental data are indicated by the solid circles and the values calculated with the code GEMINI are shown by the histograms. The dashed curve indicates the cross section associated with classical evaporation residues which decay only by the emission of light particles ($Z \leq 2$). Note the value of the excitation energy (E^*) corresponding to complete fusion and the value of J_{max} assumed to fit the data.

Fig. 24 Angle-integrated cross sections (solid circles) plotted as a function of the fragment Z-value for the 14.7 & 18 MeV/u $^{139}La + ^{12}C$ reactions.[16] See Fig. 23.

Fig. 25 Representative Z_1-Z_2 contour plots for coincidence events from the reactions $^{93}Nb + ^{9}Be$ & ^{27}Al at 11.4 and 18.0 MeV/u. Z_1 and Z_2 refer to the Z-values of fragments detected in two detectors at equal angles on opposite sides of the beam.[13]

Fig. 26 Representative Z_1-Z_2 contour plots for coincidence events from the reactions $^{139}La + ^{12}C$ & ^{27}Al at 14.7 and 18.0 MeV/u. Z_1 and Z_2 refer to the Z-values of fragments detected in two detectors at equal angles on opposite sides of the beam.[16]

Fig. 27 The relative yield of coincidence events plotted as a function of the sum of the atomic charges of the two coincident fragments for the $^{139}La + ^{12}C$ & ^{27}Al reactions at 18 MeV/u.[16]

Fig. 28 The mean sum $\langle Z_1 + Z_2 \rangle$ of coincidence events plotted as a function of Z_2 for the $^{93}Nb + ^{9}Be$ & ^{27}Al reactions at 25.4 and 30.3 MeV/u. The dashed lines indicate the average charge of the source system estimated from the mass transfer. The charge loss for binary events due to sequential evaporation was estimated using the evaporation code PACE, and the residual $Z_1 + Z_2$ values are indicated by the solid curves.[11]

Fig. 29 Contour diagrams of the experimental $Z_1 - Z_2$ correlation for coincident fragments detected at symmetric angles on opposite sides of the beam in the $^{139}La + ^{12}C$ reactions at 18, 50, 80, and 100 MeV/u.[12,16,68]

Fig. 30 The relative yield of coincidence events plotted as a function of the sum of the atomic charges of the two coincident fragments for the $^{139}La + ^{12}C$ reactions at 18, 50, 80 and 100 MeV/u.[12,16,68]

Fig. 31 Angular distributions in the c.m. system for the representative Z-values from the 80 & 100 MeV/u $^{139}La + ^{12}C$ reactions.[68]

Fig. 32 Angle-integrated charge distributions for the 50, 80 & 100 MeV/u $^{139}La + ^{12}C$ reactions. The histograms represent calculations with the statistical code GEMINI.[13]

Fig. 33 The extracted summed charge distributions for binary (solid) ternary (dashed) and quaternary (dotted curve) events from the 80 & 100 MeV/u $^{139}La + ^{12}C$ reactions.[68]

Fig. 34 The extracted rapidity distributions for binary (solid), ternary (dashed) and quaternary (dotted curve) events from the 80 & 100 MeV/u $^{139}La + ^{12}C$ reactions.[68] The vertical arrows denote the beam and complete-fusion velocities.

Fig. 35 γ-ray spectra for three different bins in total kinetic enegy loss (TKEL) for the reaction $^{100}Mo + ^{100}Mo$ at 19.5 MeV/u. The solid curves represent statistical model calculations. The dotted curve is obtained in the same way as the solid curve except for the elimination of the quasideuteron component in the γ-ray cross section.[71]

Fig. 36 a) "Temperatures" of Boltzman fits to measured (open circles) and calculated (stars) γ-ray spectra. The solid line denotes the primary temperature of the fragments which has been calculated from the energy loss. b) Experimental and theoretical multiplicities of hard photons with energies $\geq$ 15 (squares) and $\geq$ 30 MeV (circles), respectively. The different lines are the result of a statistical model calculation and show the first chance contribution (dotted line), the sum over all generations (solid line) and the effect of the experimental binning of the excitation energy (dashed line).[71]

Fig. 37 Thermal-fluctuations enhancement factor in the emission of pions as a function of the total excitation energy.[74]

Fig. 38 Pion spectra calculated with and without the enhancement factor due to thermal fluctuations.[74]

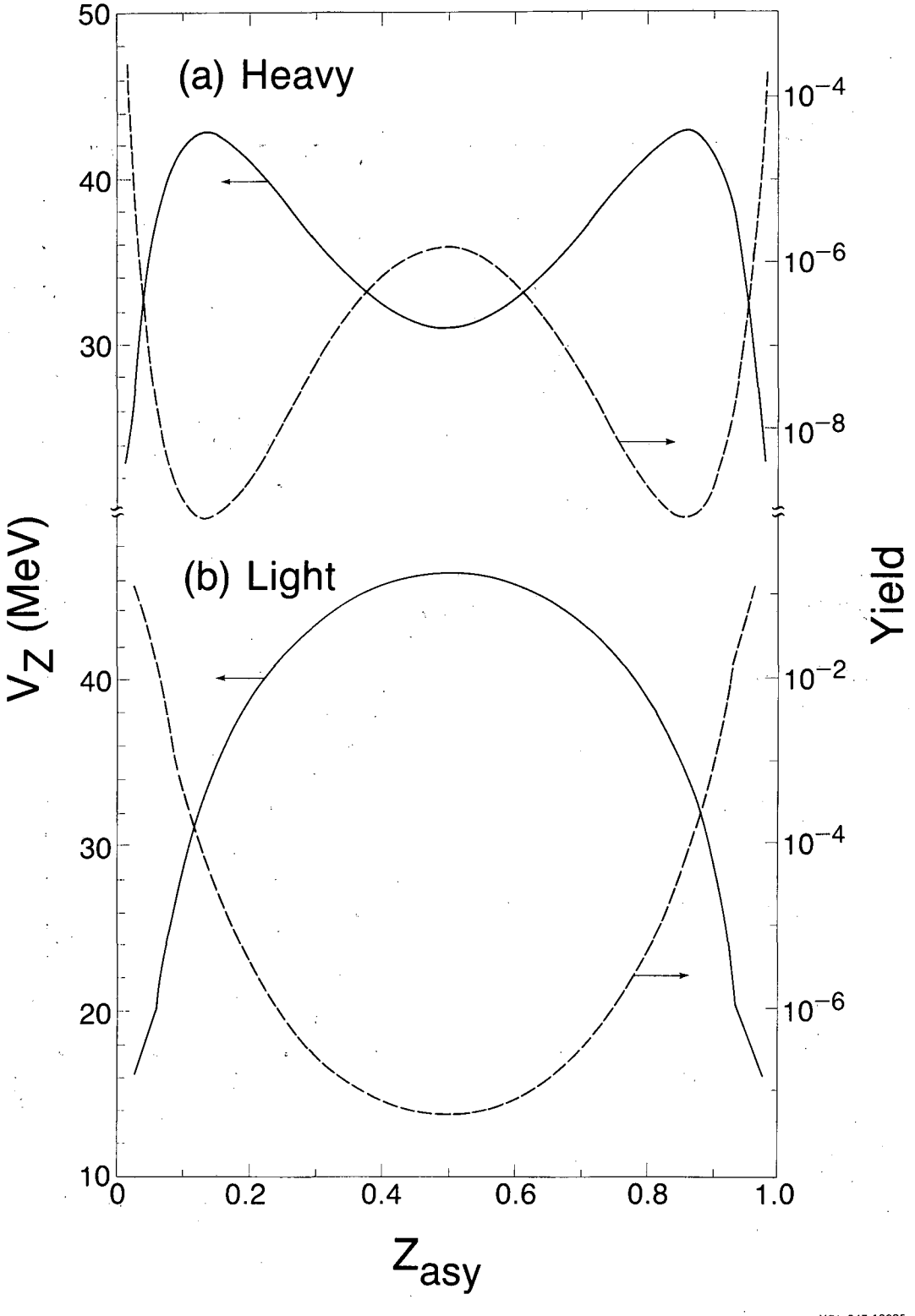
(a) Heavy
(b) Light
V_Z (MeV)
Z_{asy}
Yield
50
40
30
10
20
0
0.2
0.4
0.6
0.8
1.0
10^{-4}
10^{-6}
10^{-8}
10^{-2}
XBL 847-10685

Fig. 1

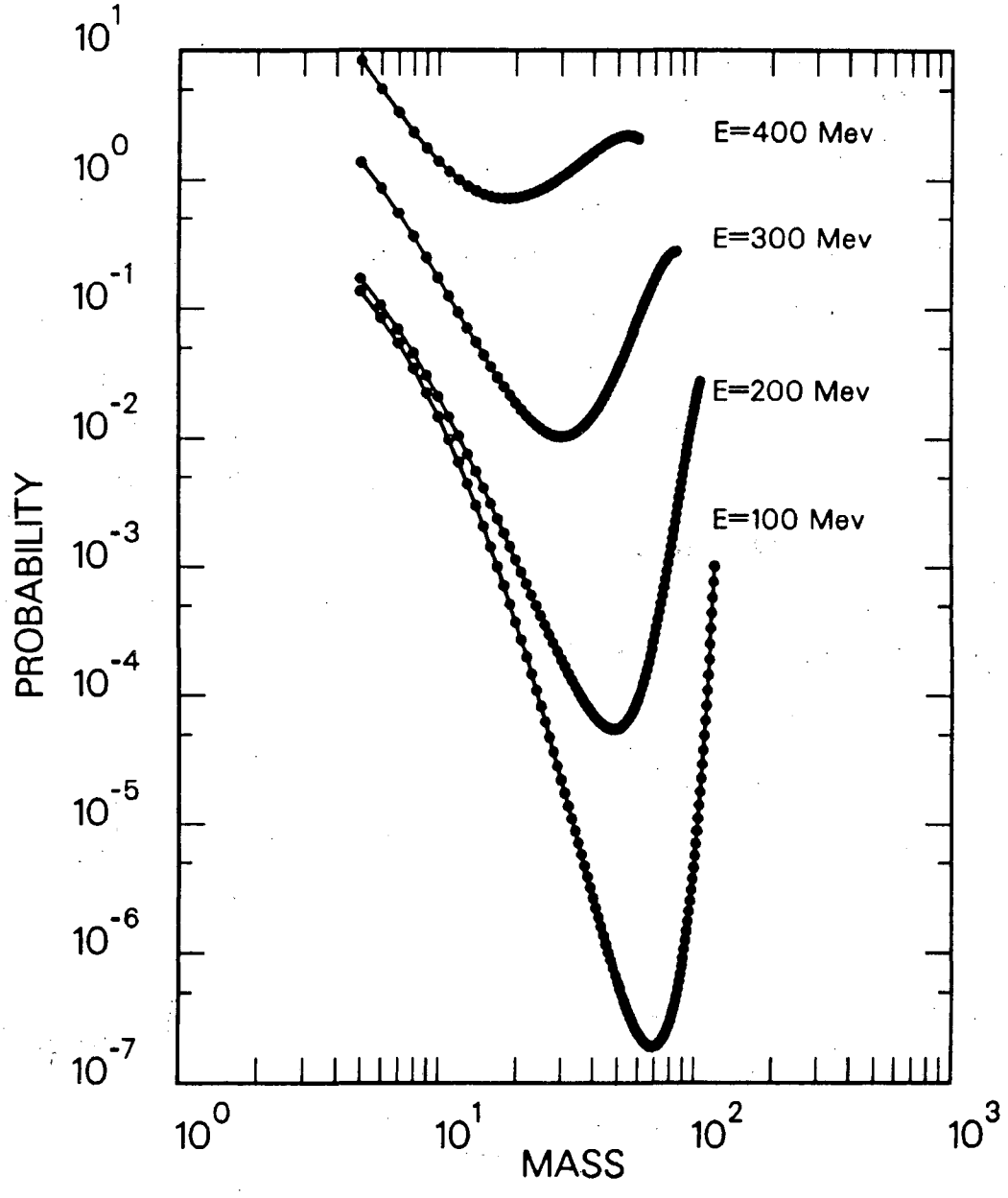

XBL 885-1804

Fig. 2

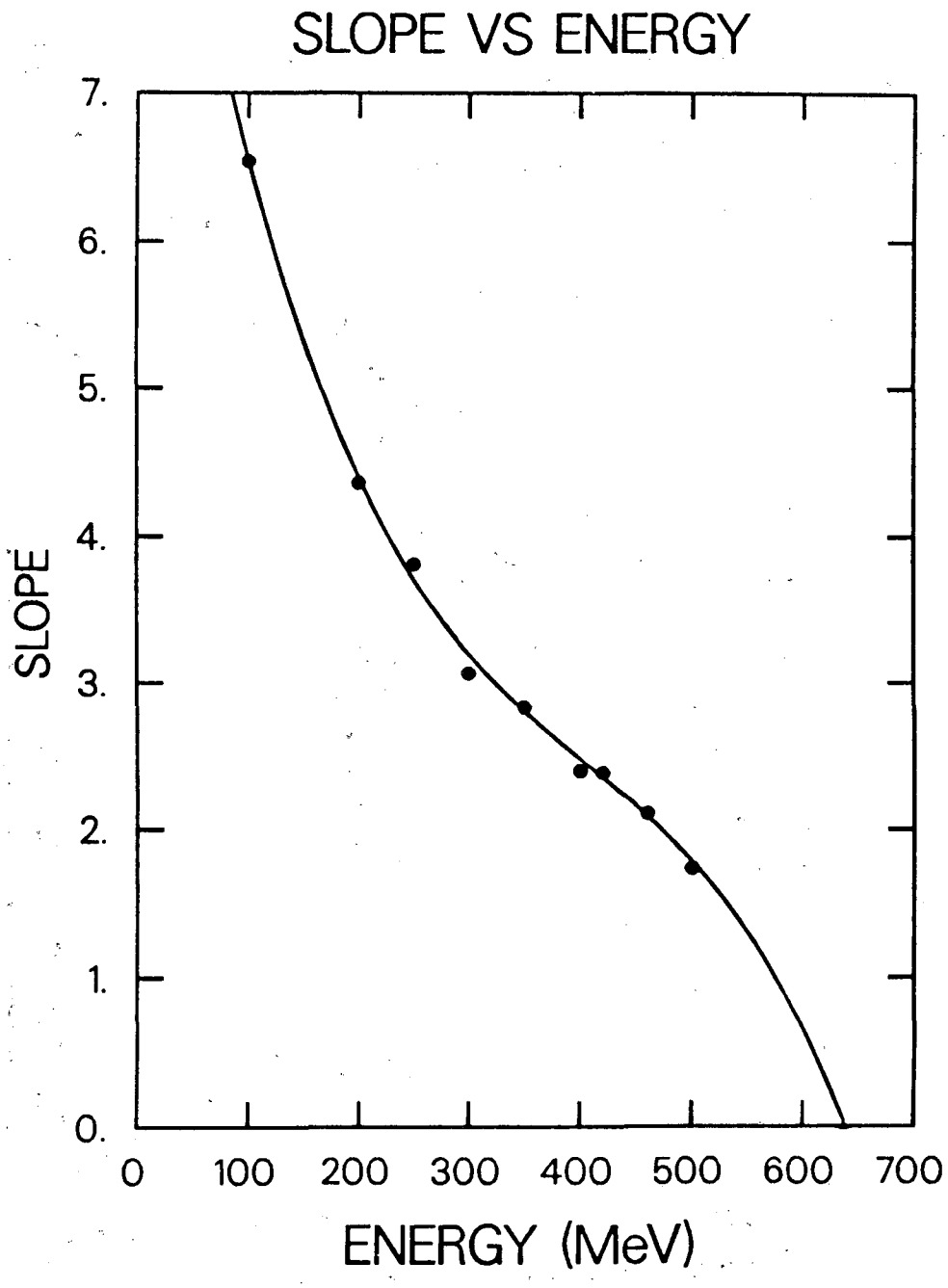

XBL 885-1805

Fig. 3

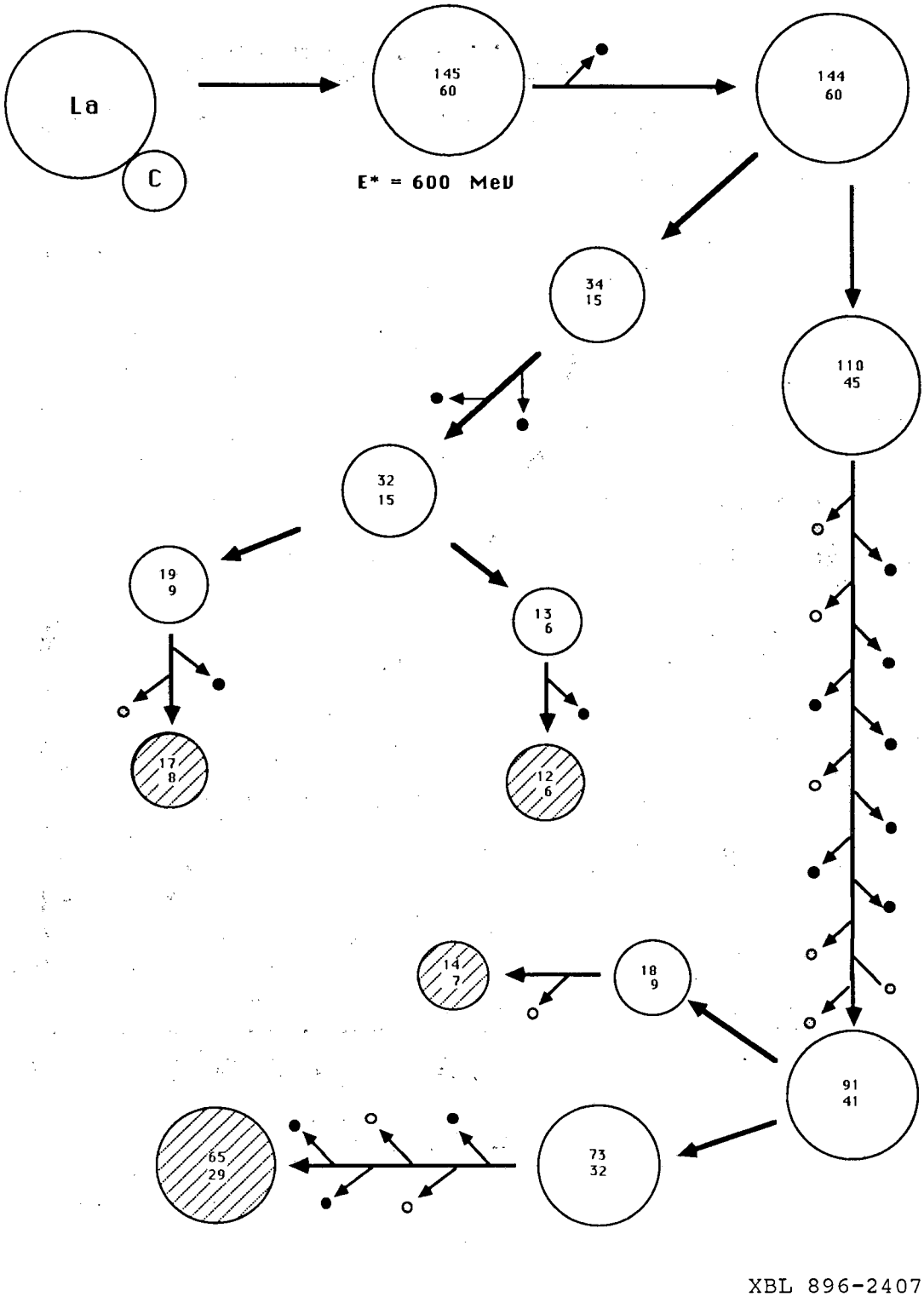
La
C
145
60
E* = 600 MeV
144
60
34
15
110
45
32
15
19
9
13
6
17
8
12
6
14
7
18
9
91
41
65
29
73
32
XBL 896-2407

Fig. 4a

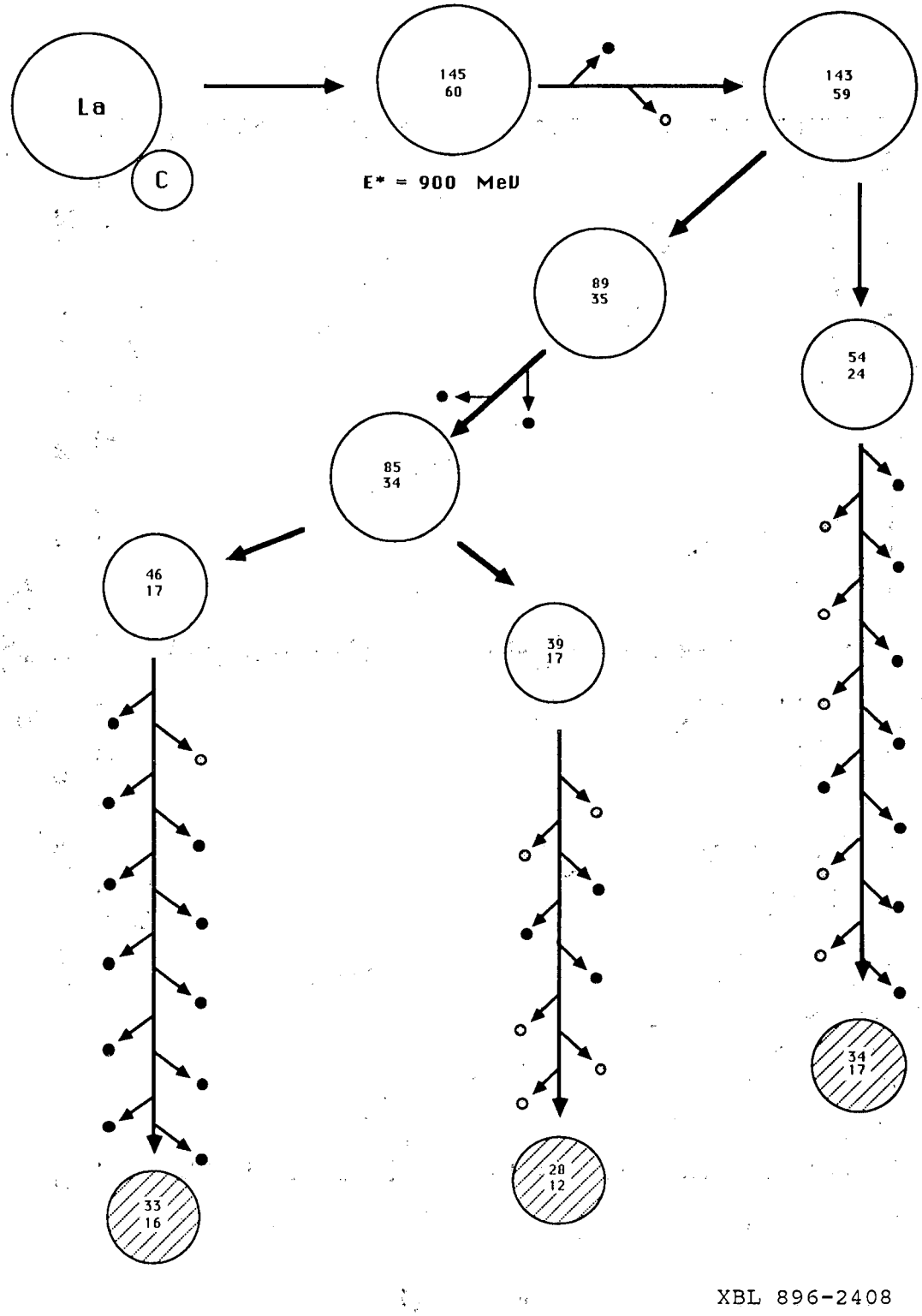
La
C
145
60
E* = 900 MeV
143
59
89
35
54
24
85
34
46
17
39
17
34
17
28
12
33
16
XBL 896-2408

Fig. 4b

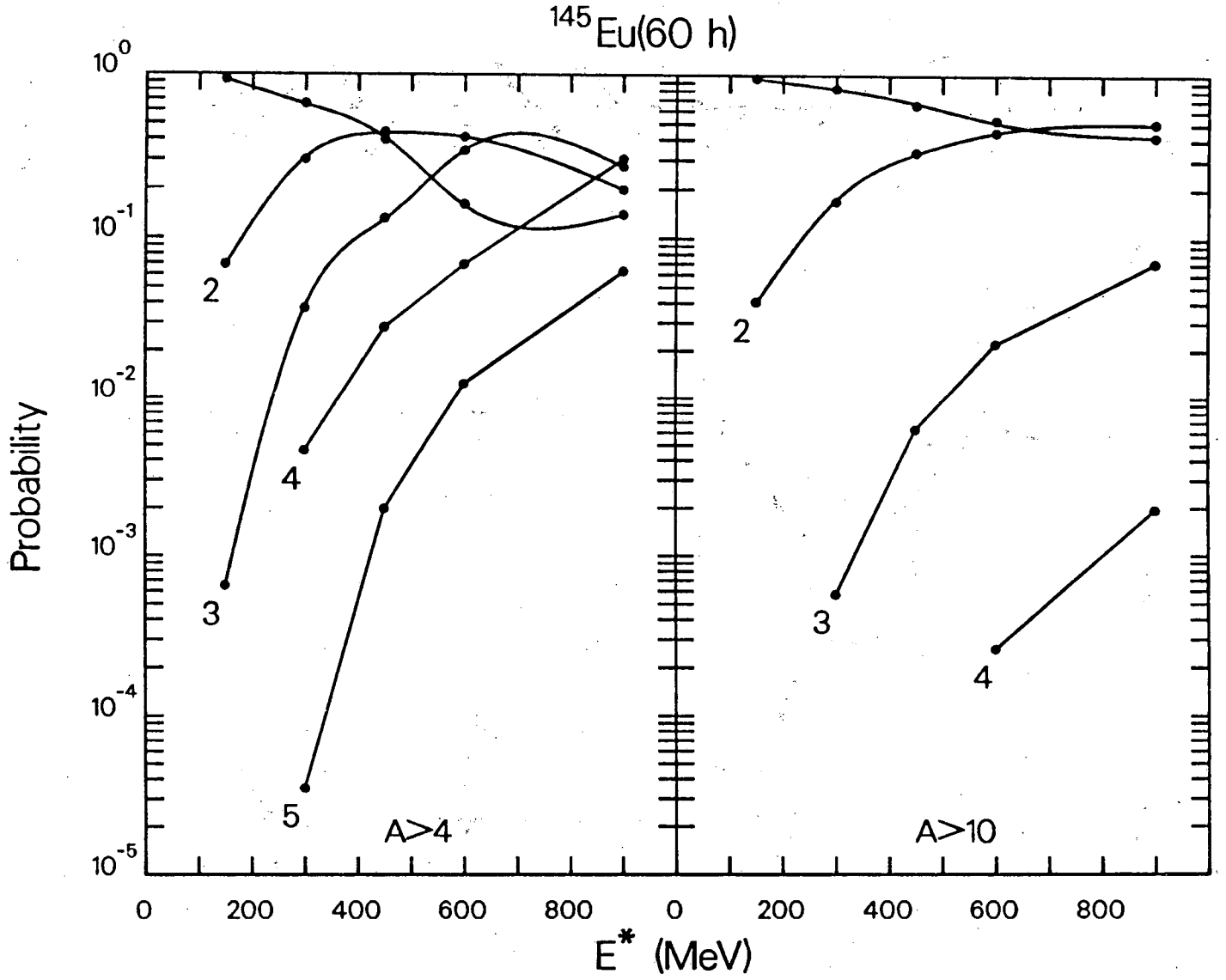

XBL 896-2409

Fig. 5

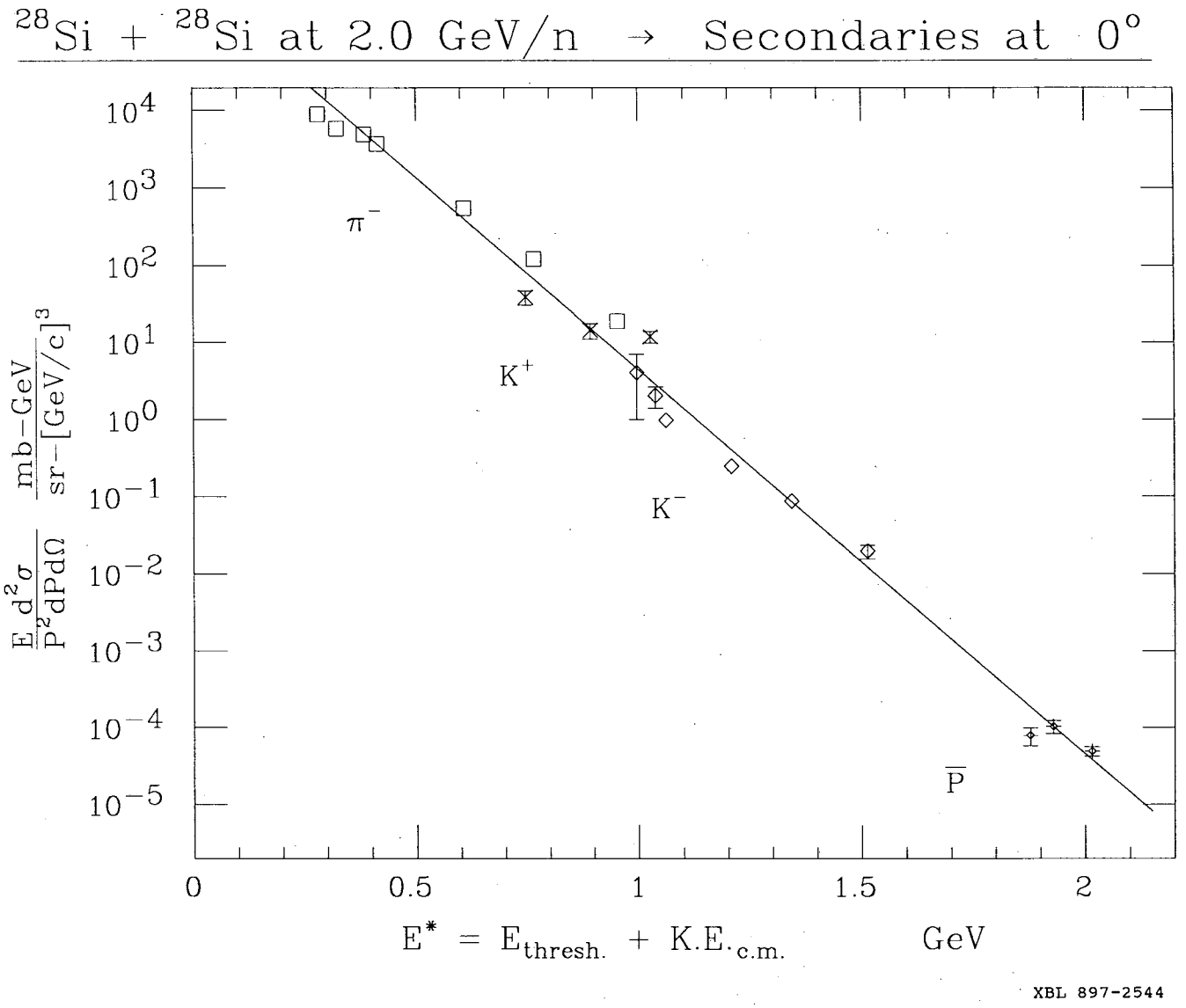
$^{28}Si + {}^{28}Si$ at 2.0 GeV/n → Secondaries at 0°
$\frac{E}{P^2}\frac{d^2\sigma}{dPd\Omega}$ $\frac{mb-GeV}{sr-[GeV/c]^3}$
10^4
10^3
10^2
10^1
10^0
10^{-1}
10^{-2}
10^{-3}
10^{-4}
10^{-5}
π^-
K^+
K^-
$\overline{P}$
0
0.5
1
1.5
2
$E^* = E_{thresh.} + K.E._{c.m.}$ GeV
XBL 897-2544

Fig. 6

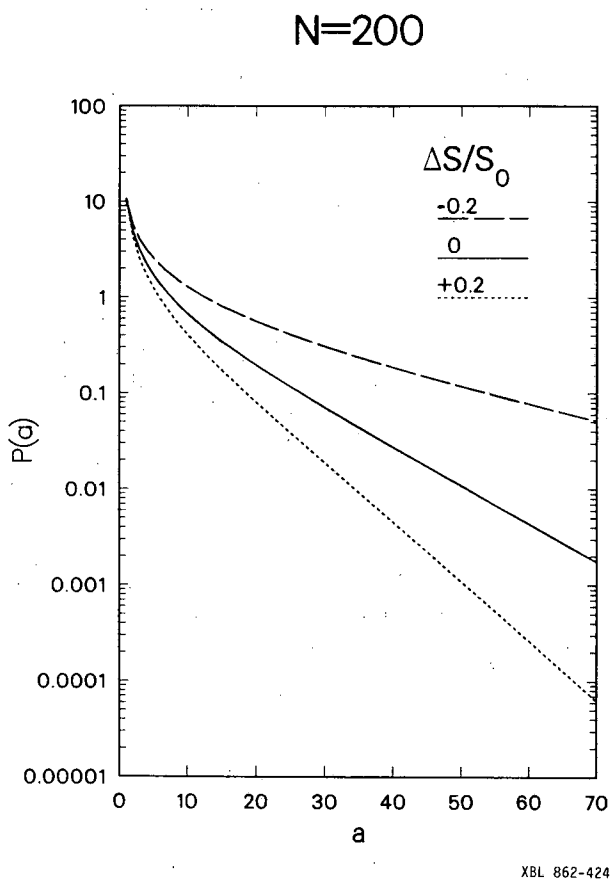
N=200
100
10
1
0.1
0.01
0.001
0.0001
0.00001
P(a)
0
10
20
30
40
50
60
70
a
ΔS/S0
-0.2
0
+0.2
XBL 862-424

Fig. 7

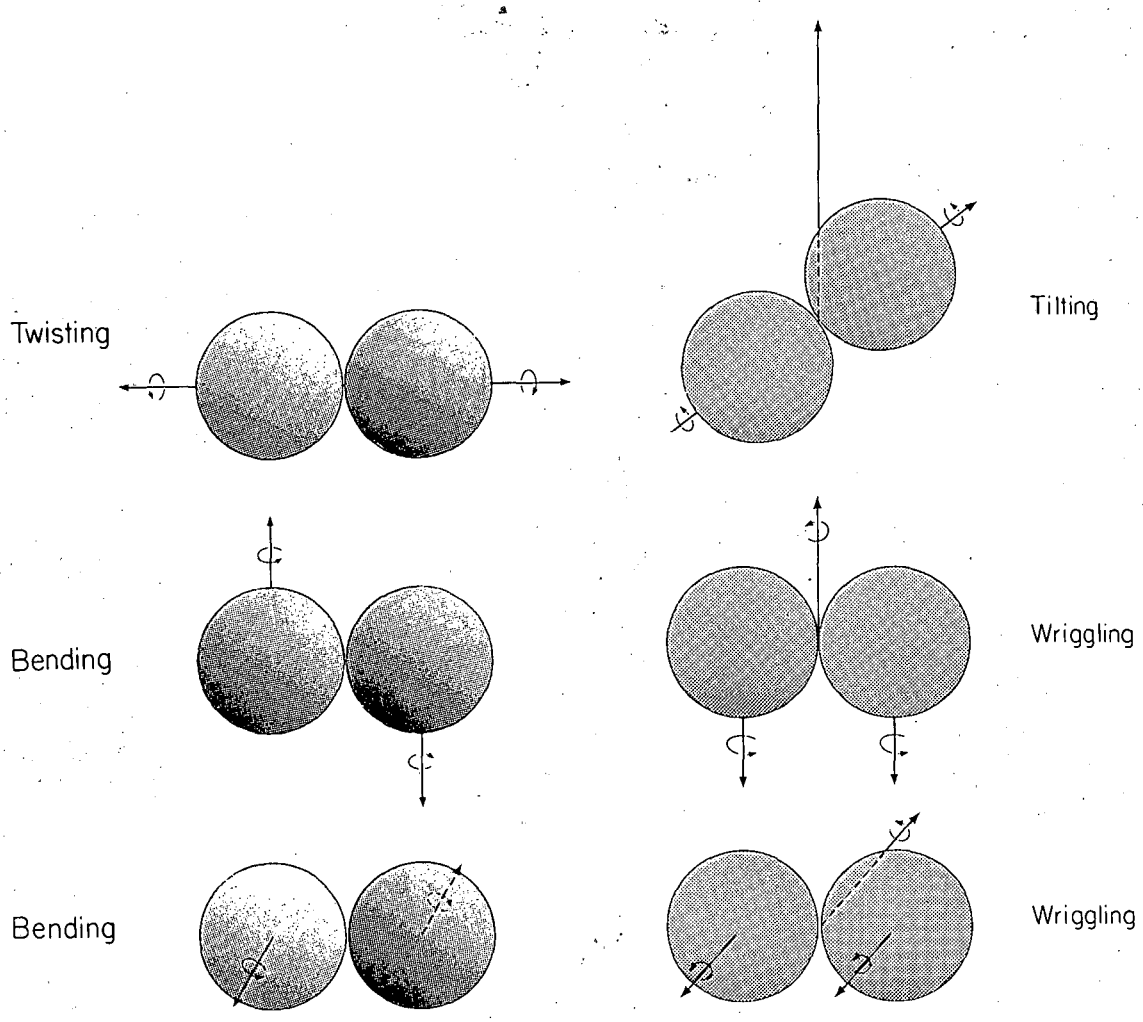
Twisting
Tilting
Bending
Wriggling
Bending
Wriggling
XBL 793-824A

Fig. 8

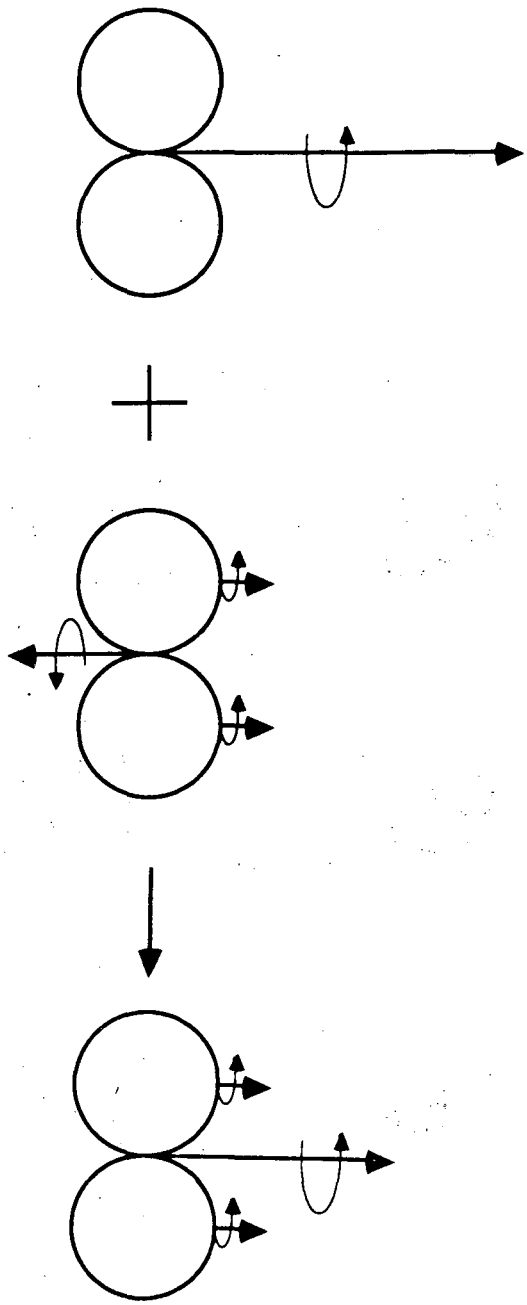

XBL 896-2410

Fig. 9

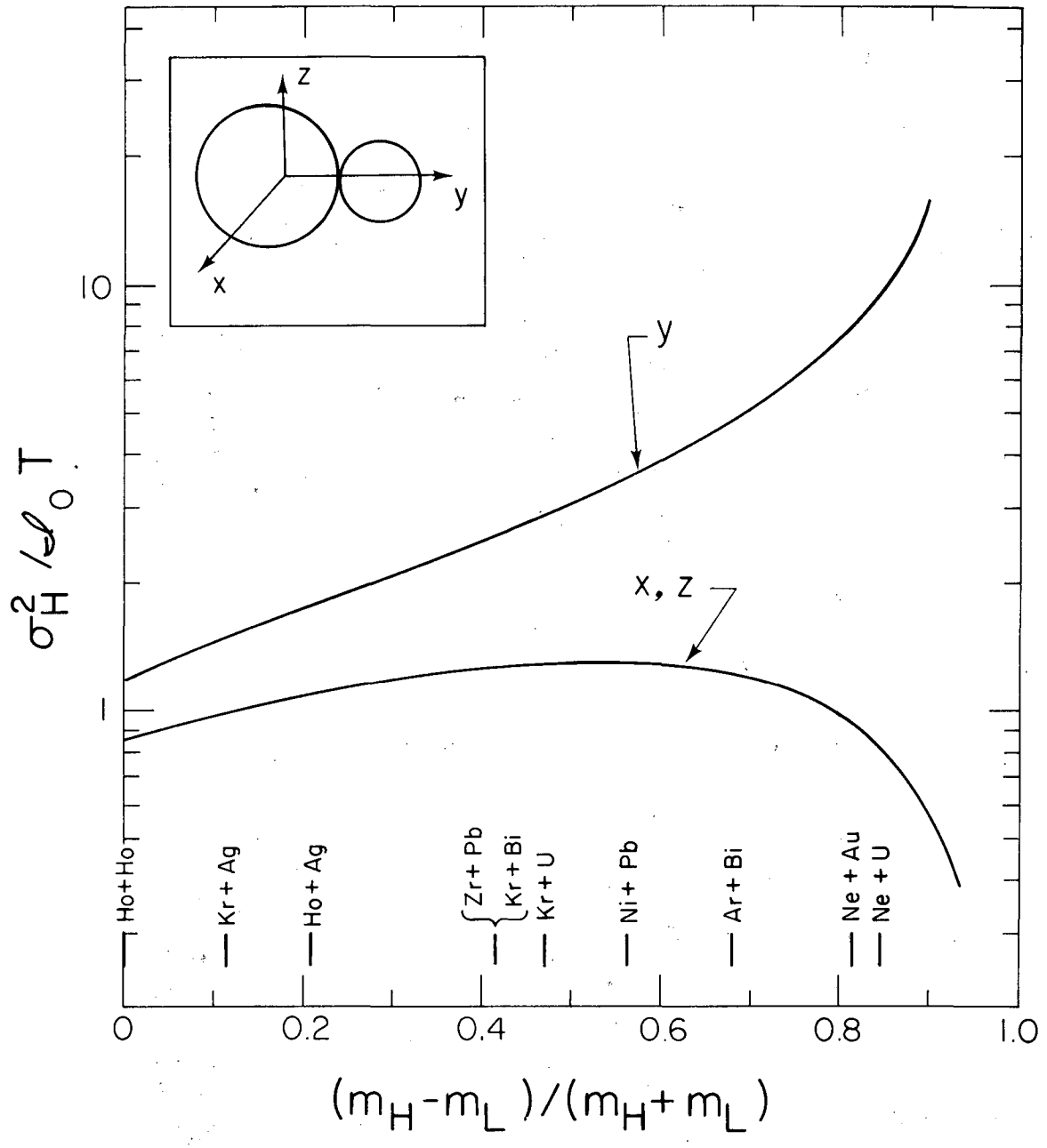

XBL 821-4405A

Fig. 10

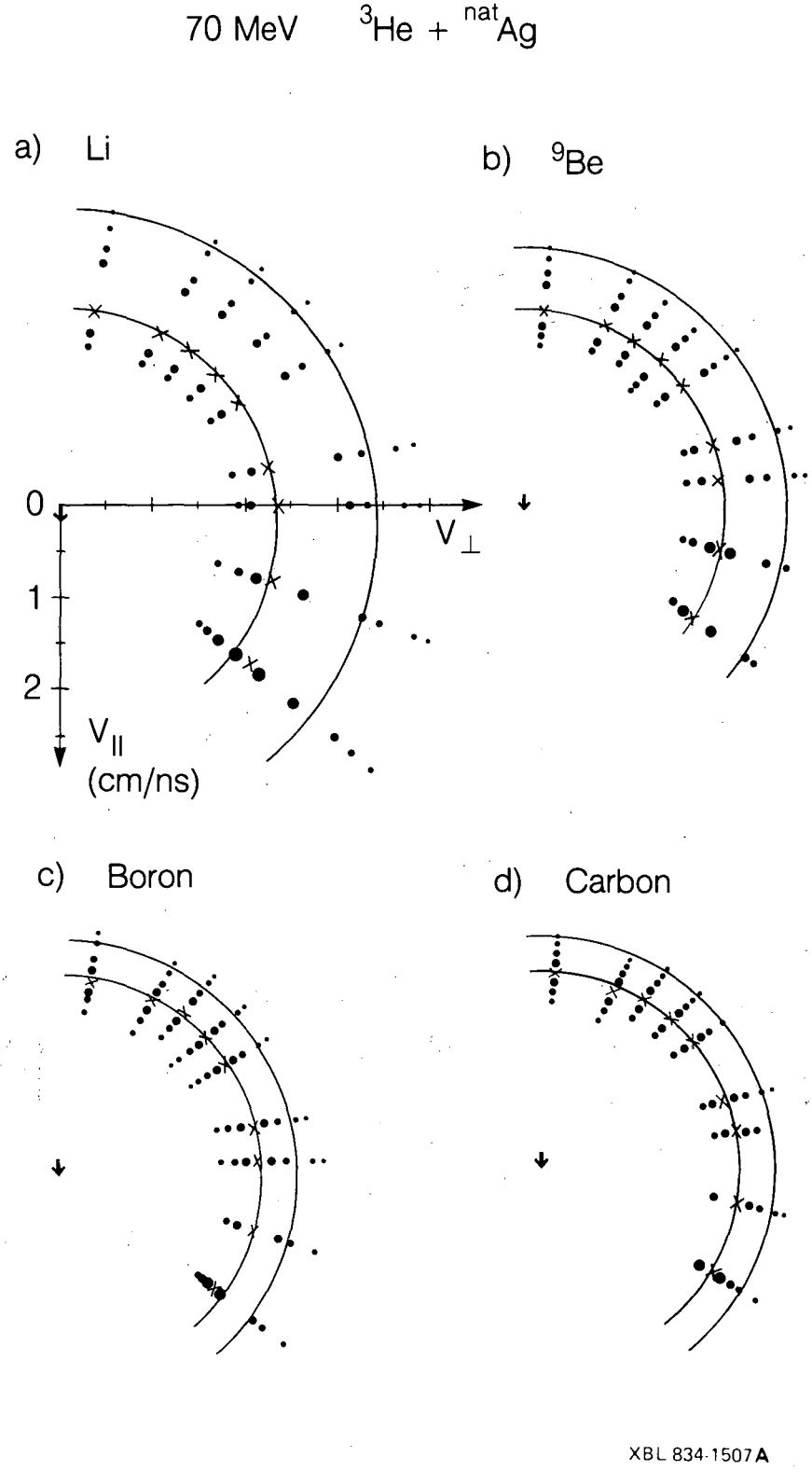
70 MeV $^{3}He + ^{nat}Ag$
a) Li
b) ^{9}Be
0
1
2
$V_{\perp}$
$V_{\parallel}$
(cm/ns)
c) Boron
d) Carbon
XBL 834-1507A

Fig. 11

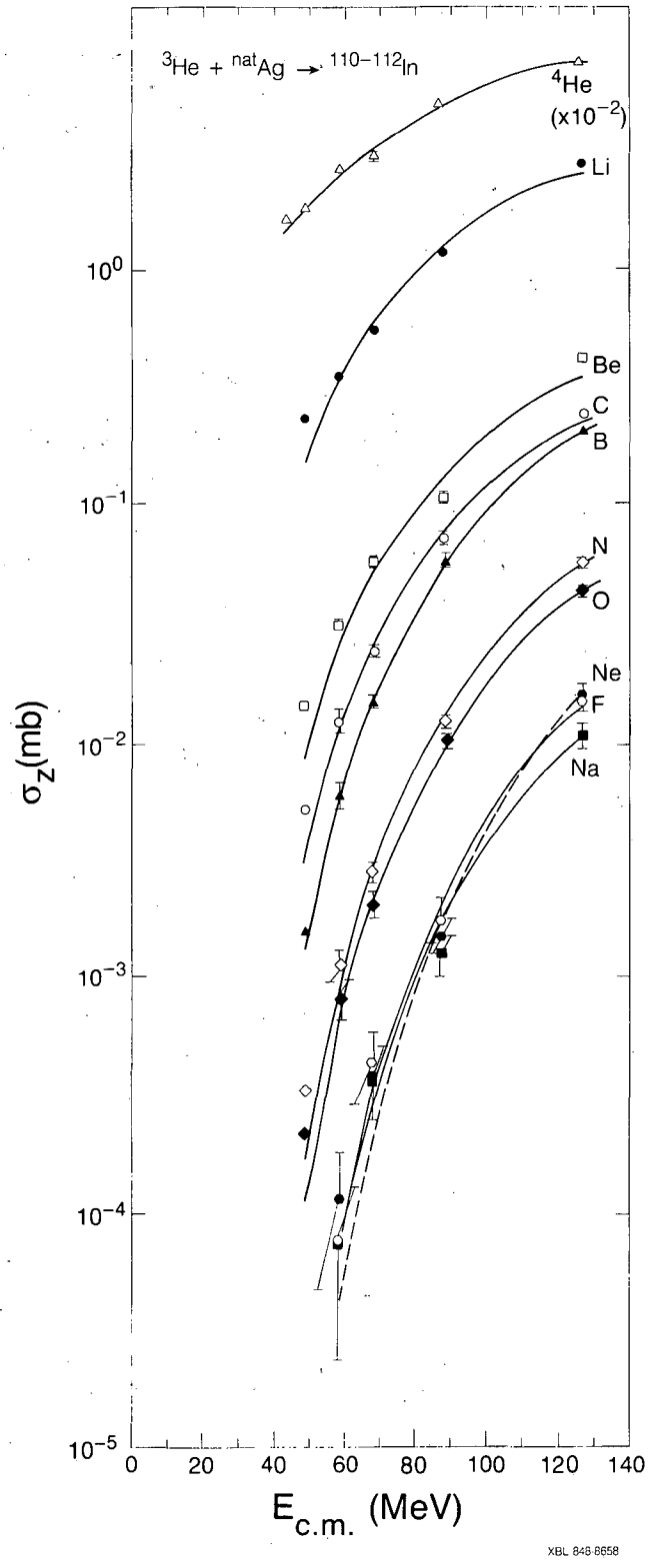
$^3He + ^{nat}Ag \rightarrow ^{110-112}In$
^4He (x10^{-2})
Li
Be
C
B
N
O
Ne
F
Na
σ_z(mb)
10^0
10^{-1}
10^{-2}
10^{-3}
10^{-4}
10^{-5}
0
20
40
60
80
100
120
140
$E_{c.m.}$ (MeV)
XBL 848-8658

Fig. 12

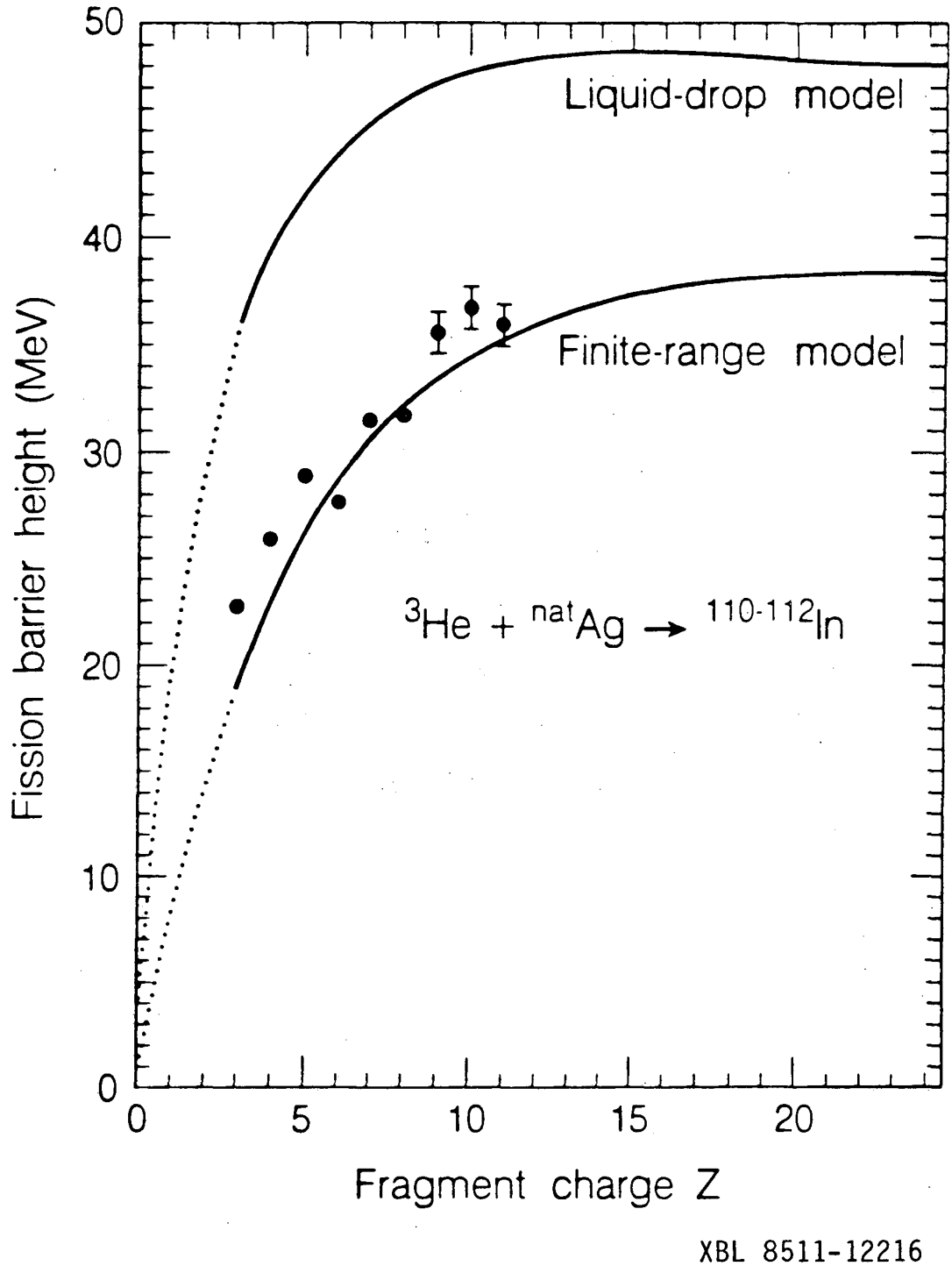
Liquid-drop model
Finite-range model
$^{3}He + {}^{nat}Ag \rightarrow {}^{110\text{-}112}In$
Fission barrier height (MeV)
Fragment charge Z
0
10
20
30
40
50
0
5
10
15
20
XBL 8511-12216

Fig. 13

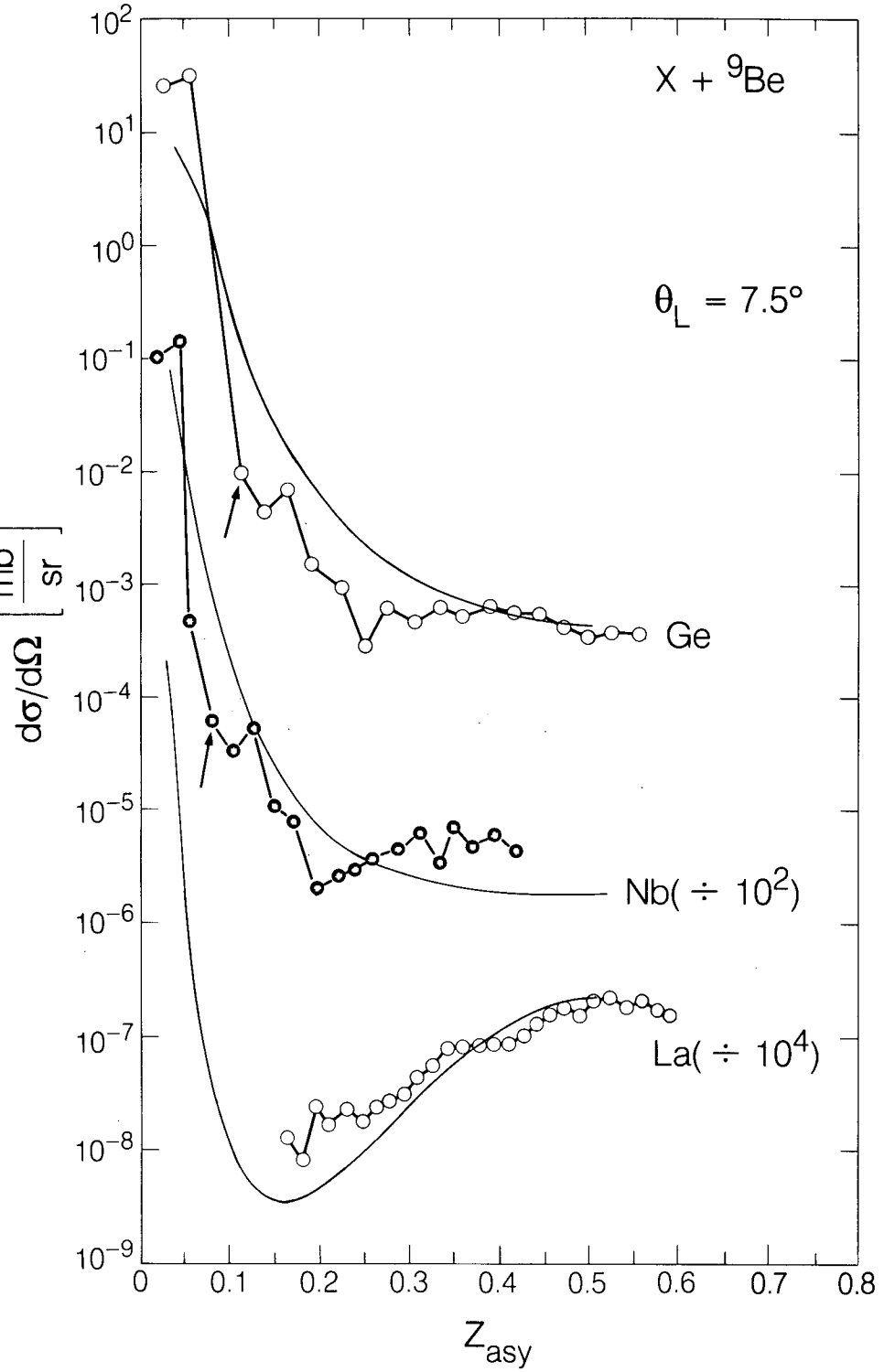

Fig. 14

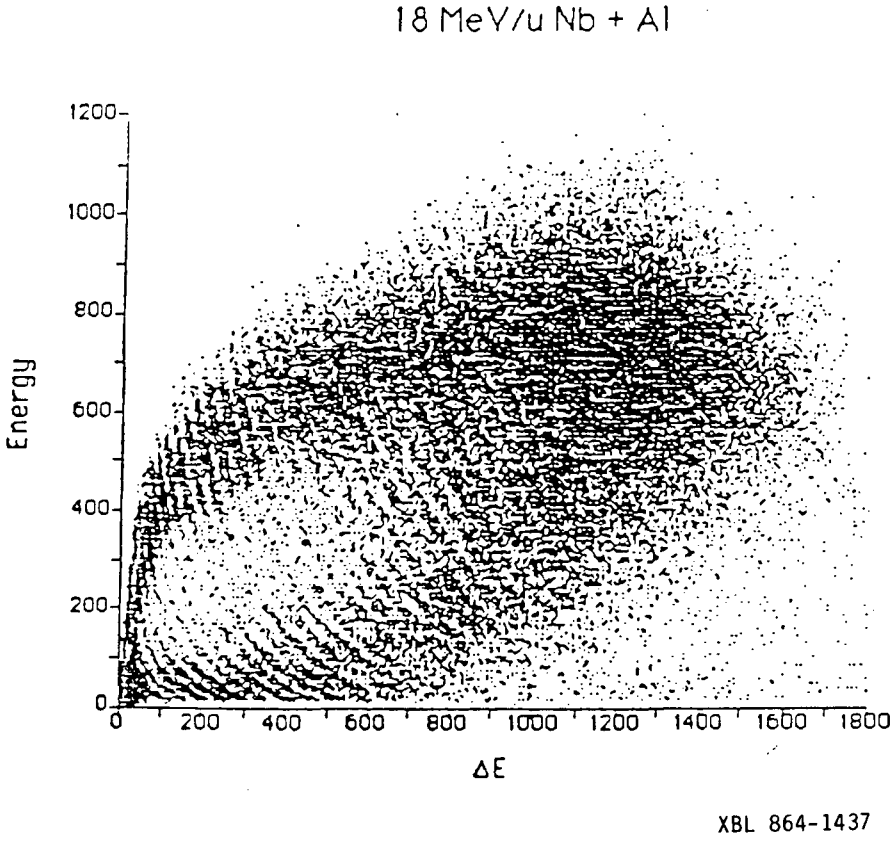
18 MeV/u Nb + Al
Energy
1200
1000
800
600
400
200
0
0
200
400
600
800
1000
1200
1400
1600
1800
ΔE
XBL 864-1437

Fig. 15

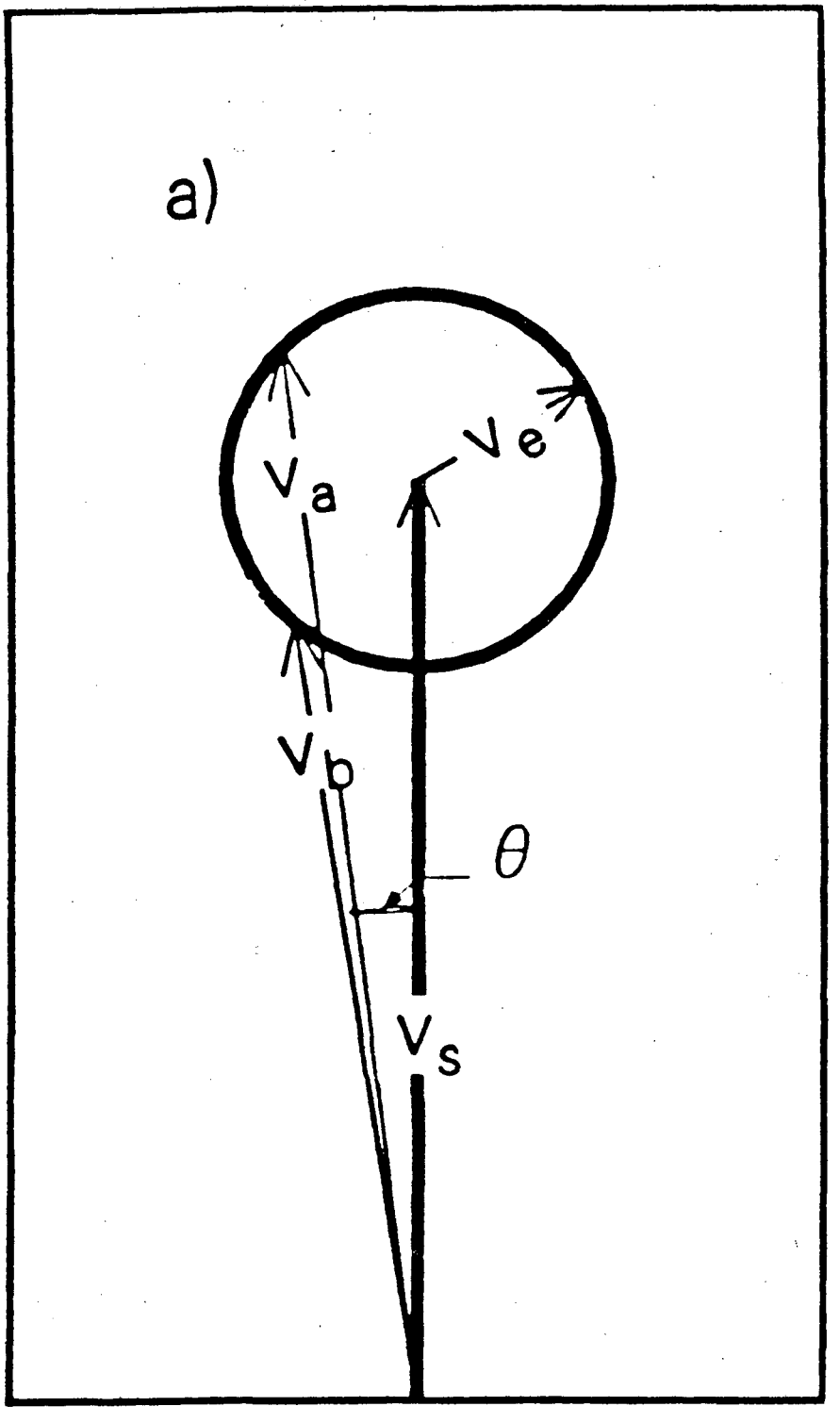

XBL 875-2329 B

Fig. 16

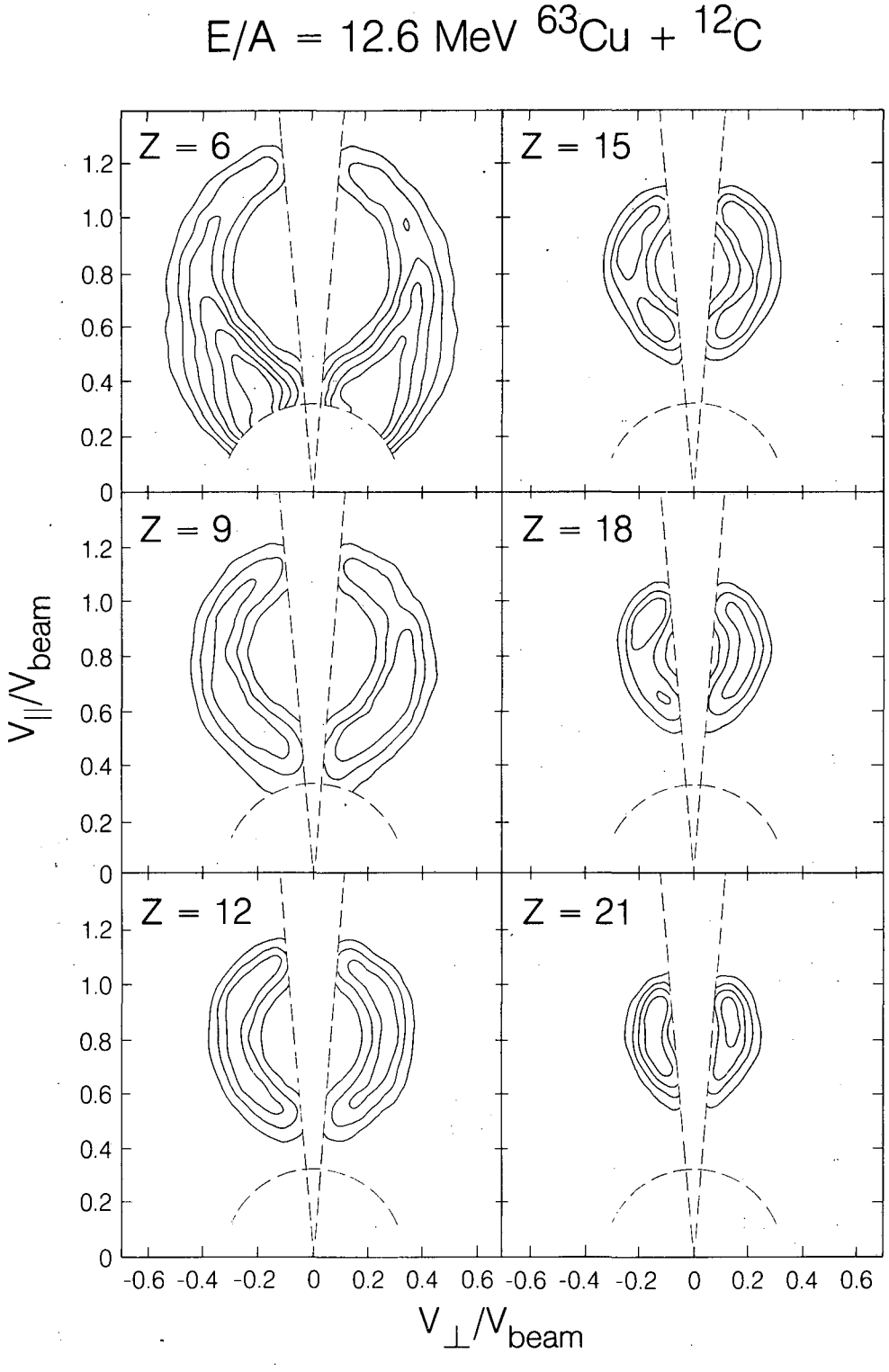
E/A = 12.6 MeV ^{63}Cu + ^{12}C
Z = 6
Z = 15
Z = 9
Z = 18
Z = 12
Z = 21
$V_{||}/V_{beam}$
$V_{\perp}/V_{beam}$
0
0.2
0.4
0.6
0.8
1.0
1.2
-0.6 -0.4 -0.2 0 0.2 0.4 0.6
XBL 881-8012

Fig. 17

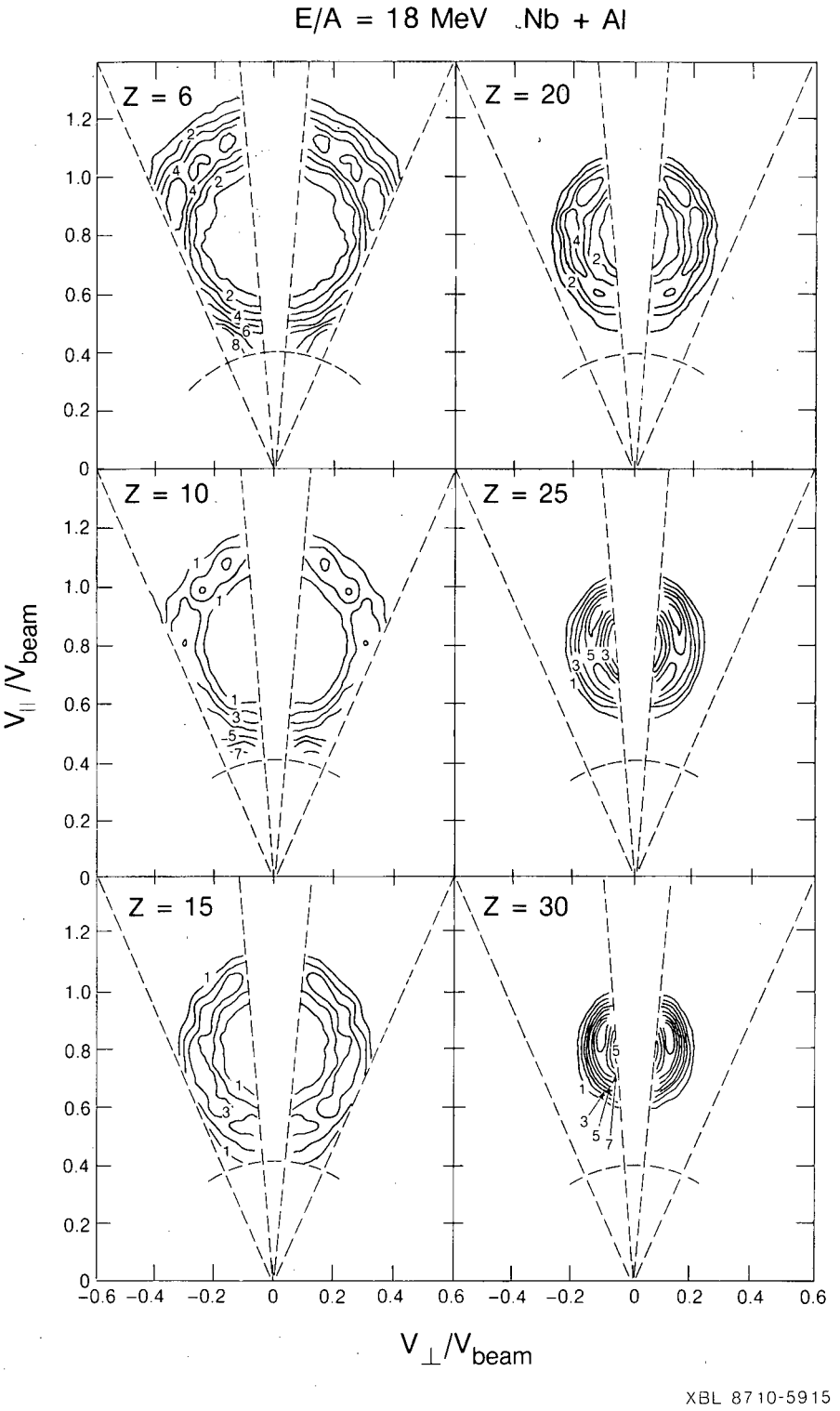
E/A = 18 MeV Nb + Al
Z = 6
Z = 20
Z = 10
Z = 25
Z = 15
Z = 30
$V_{\parallel}/V_{beam}$
$V_{\perp}/V_{beam}$
XBL 8710-5915

Fig. 18

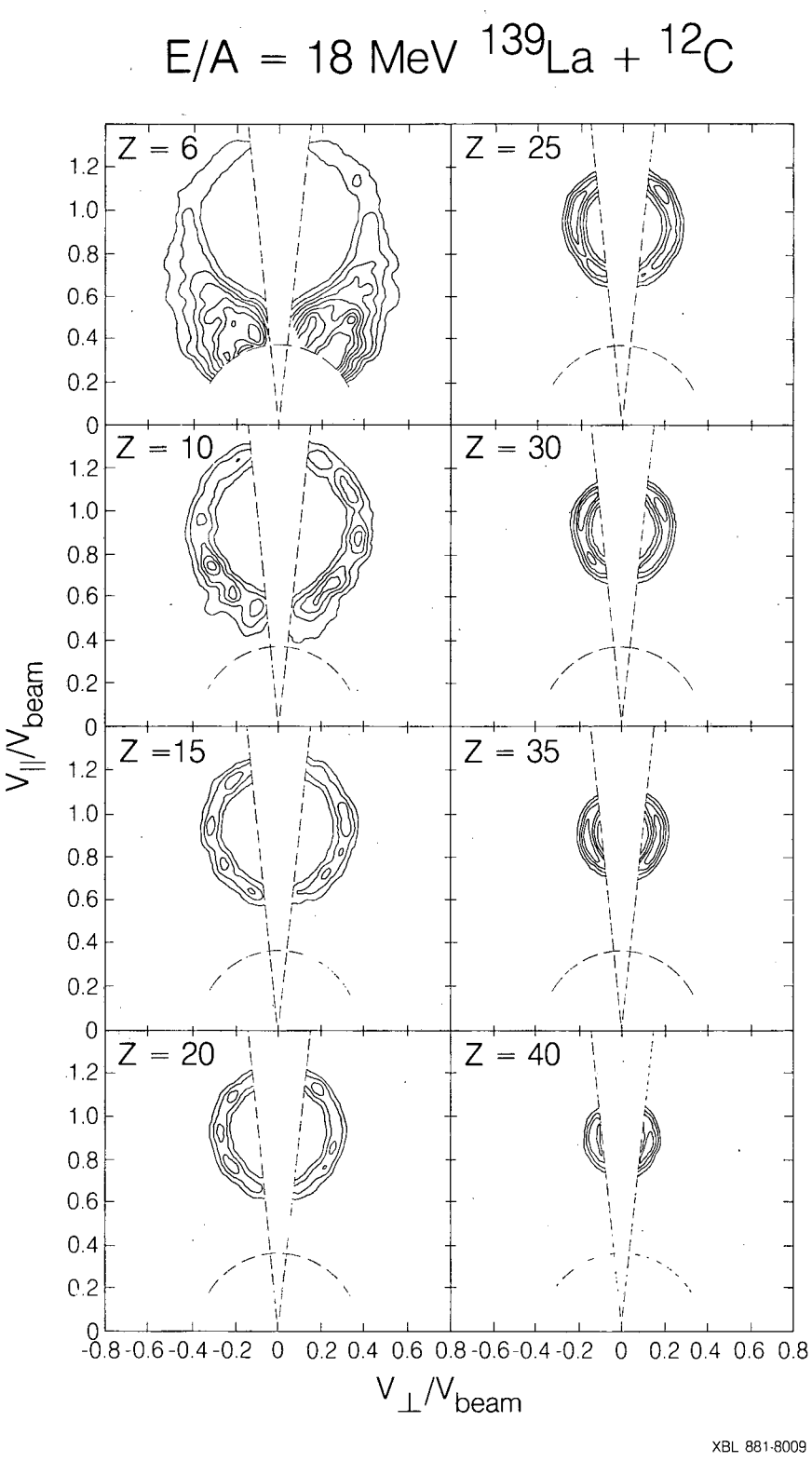
E/A = 18 MeV ^{139}La + ^{12}C
Z = 6
Z = 25
Z = 10
Z = 30
Z =15
Z = 35
Z = 20
Z = 40
$V_{||}/V_{beam}$
$V_{\perp}/V_{beam}$
XBL 881-8009

Fig. 19

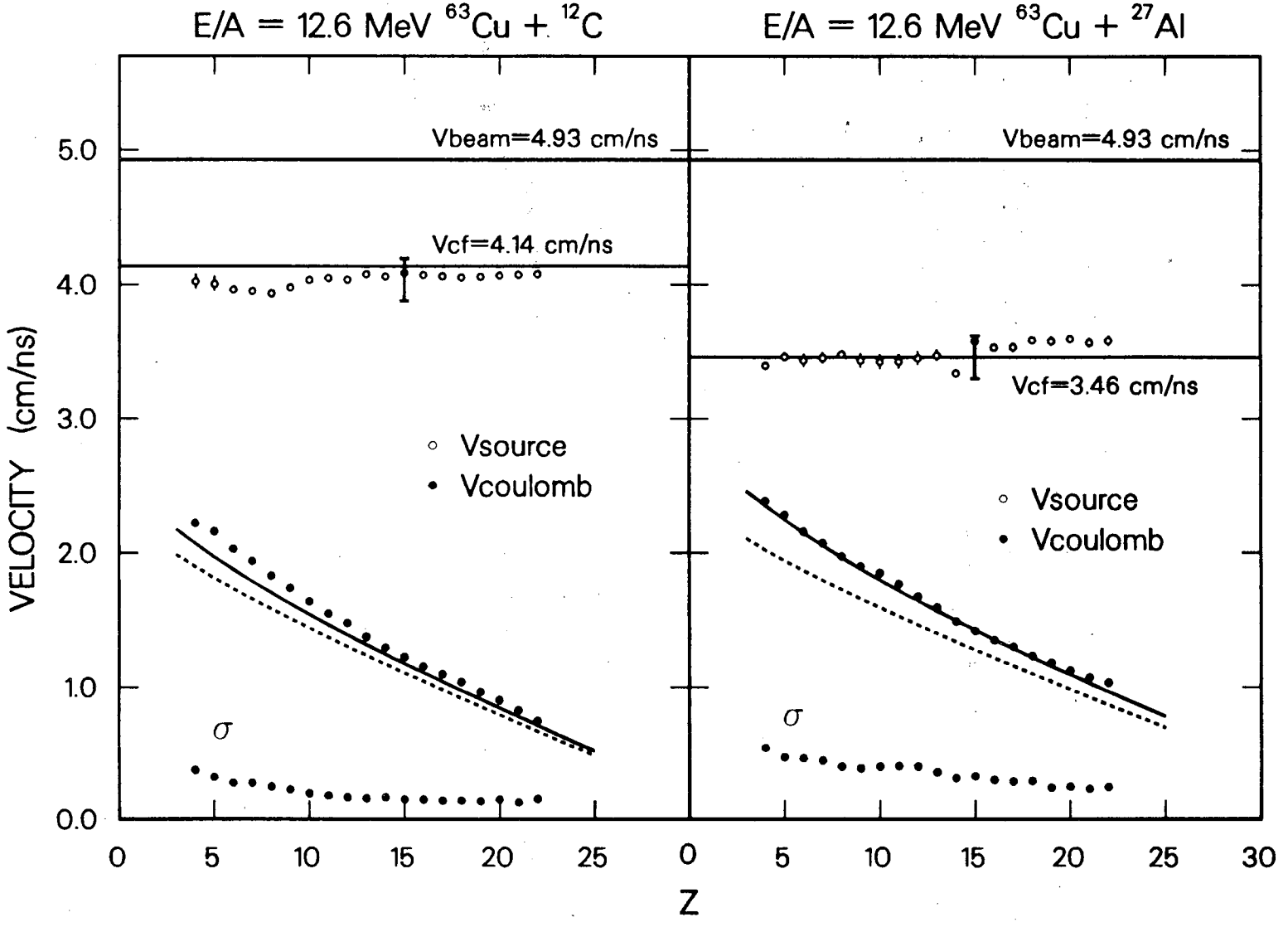
E/A = 12.6 MeV ^{63}Cu + ^{12}C
E/A = 12.6 MeV ^{63}Cu + ^{27}Al
Vbeam=4.93 cm/ns
Vcf=4.14 cm/ns
Vcf=3.46 cm/ns
Vsource
Vcoulomb
σ
VELOCITY (cm/ns)
Z
XBL 883-938

Fig. 20

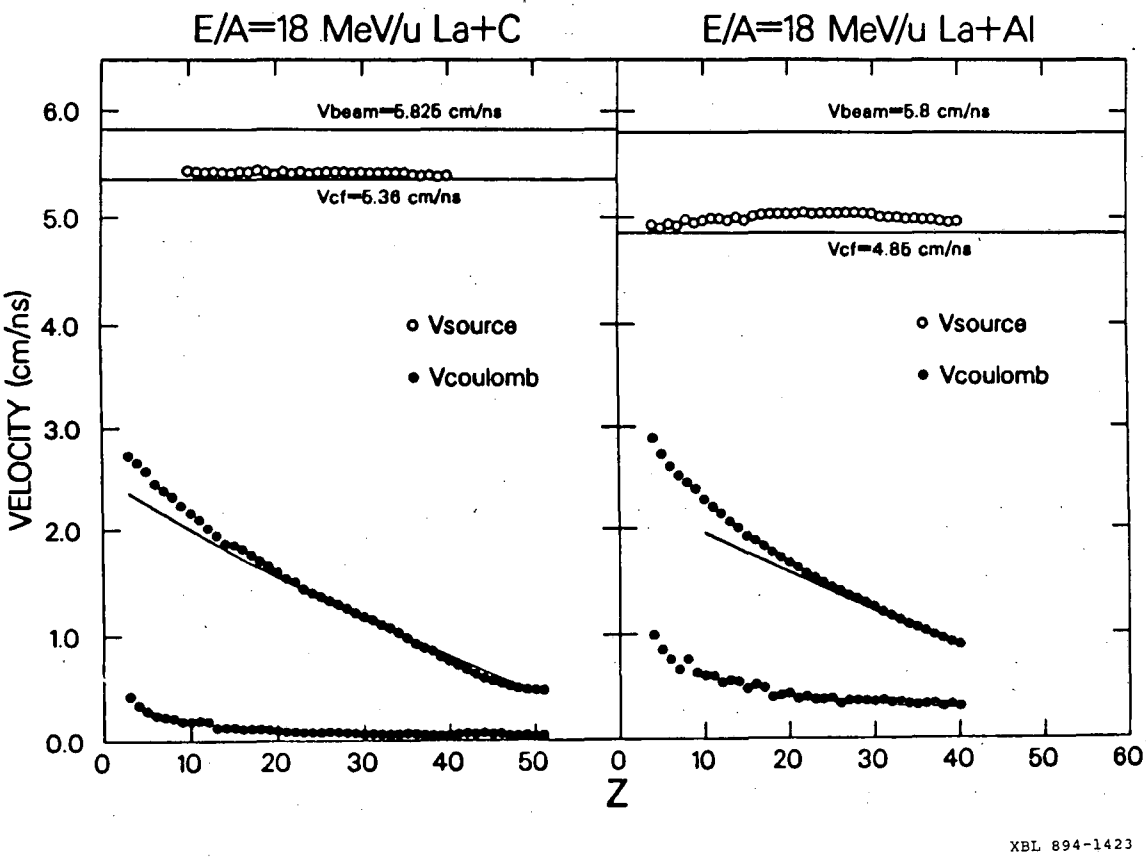
E/A=18 MeV/u La+C
E/A=18 MeV/u La+Al
Vbeam=5.825 cm/ns
Vcf=5.36 cm/ns
Vbeam=5.8 cm/ns
Vcf=4.85 cm/ns
Vsource
Vcoulomb
Vsource
Vcoulomb
VELOCITY (cm/ns)
Z
XBL 894-1423

Fig. 21

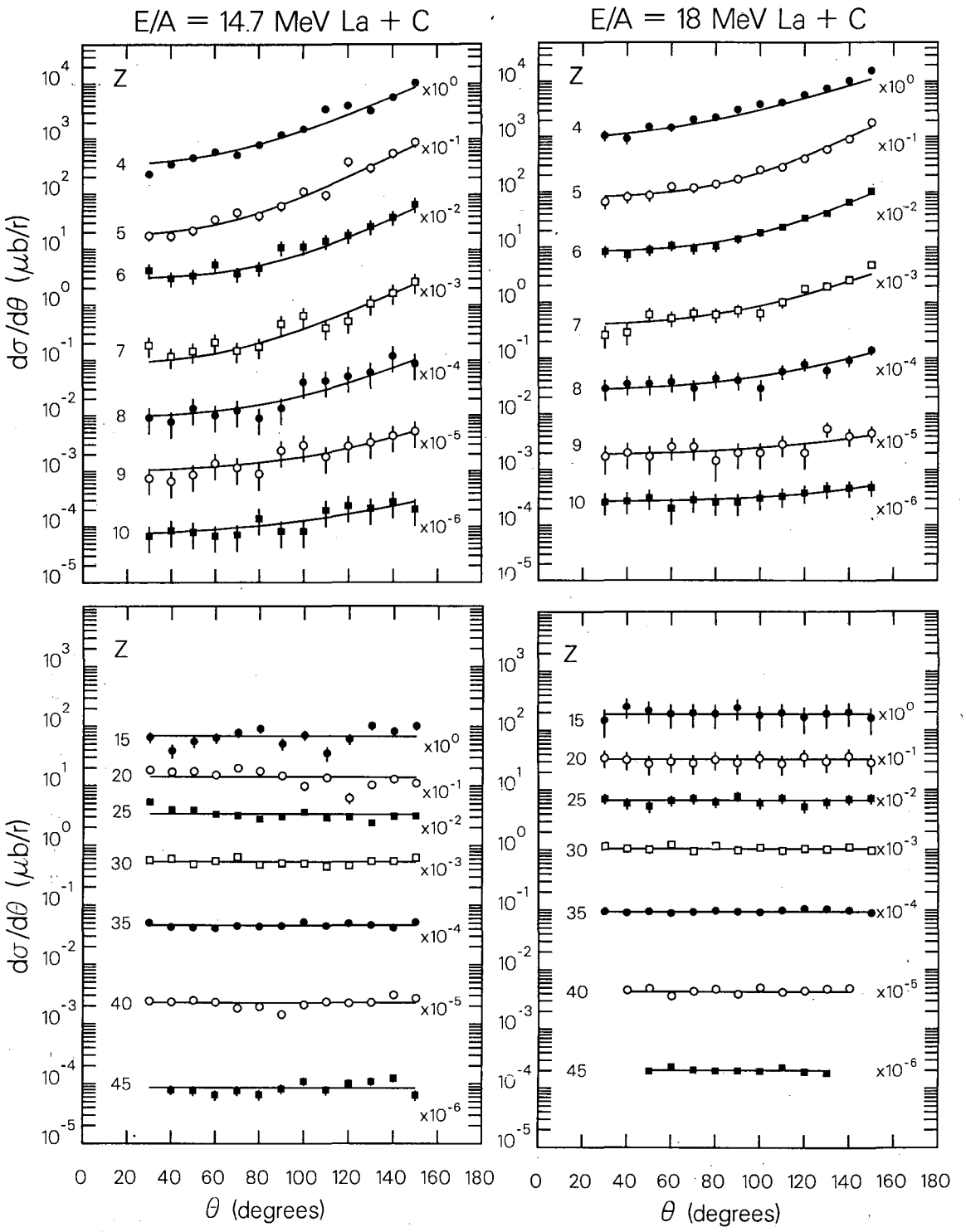

Fig. 22a

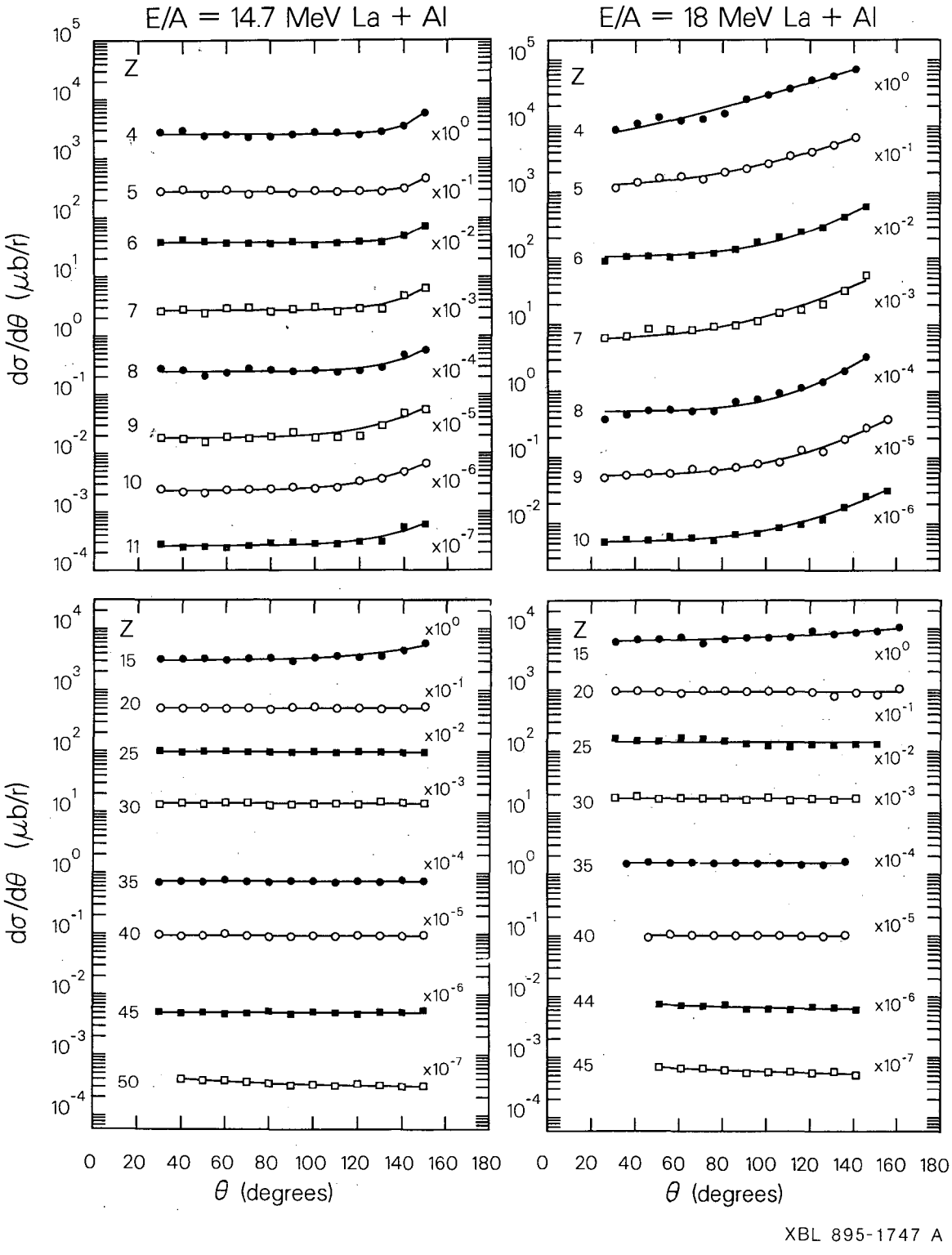
E/A = 14.7 MeV La + Al
E/A = 18 MeV La + Al
dσ/dθ (μb/r)
θ (degrees)
Z
XBL 895-1747 A

Fig. 22b

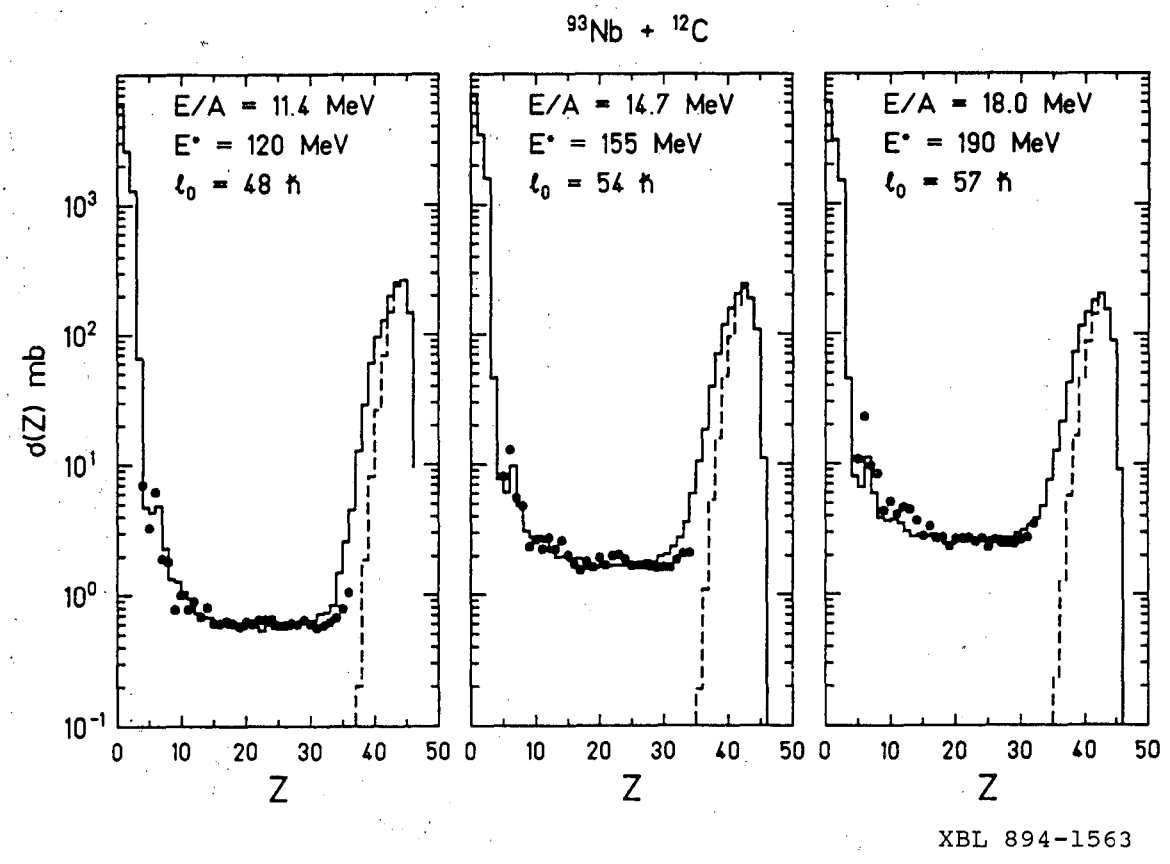
^{93}Nb + ^{12}C
E/A = 11.4 MeV
E* = 120 MeV
ℓ_0 = 48 ħ
E/A = 14.7 MeV
E* = 155 MeV
ℓ_0 = 54 ħ
E/A = 18.0 MeV
E* = 190 MeV
ℓ_0 = 57 ħ
σ(Z) mb
Z
XBL 894-1563

Fig. 23

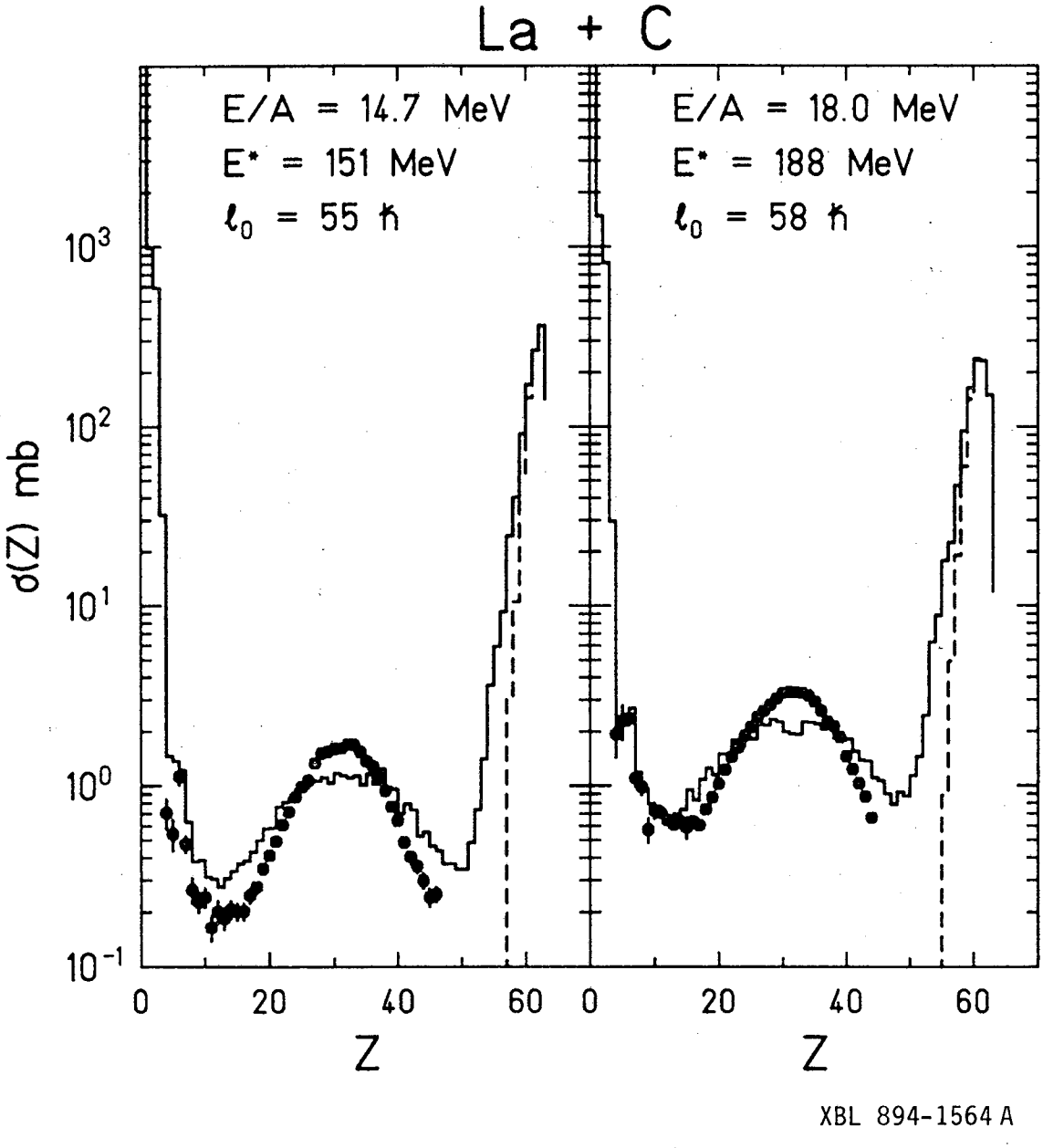
La + C
E/A = 14.7 MeV
E* = 151 MeV
ℓ_0 = 55 ħ
E/A = 18.0 MeV
E* = 188 MeV
ℓ_0 = 58 ħ
σ(Z) mb
10^3
10^2
10^1
10^0
10^{-1}
0
20
40
60
Z
XBL 894-1564 A

Fig. 24

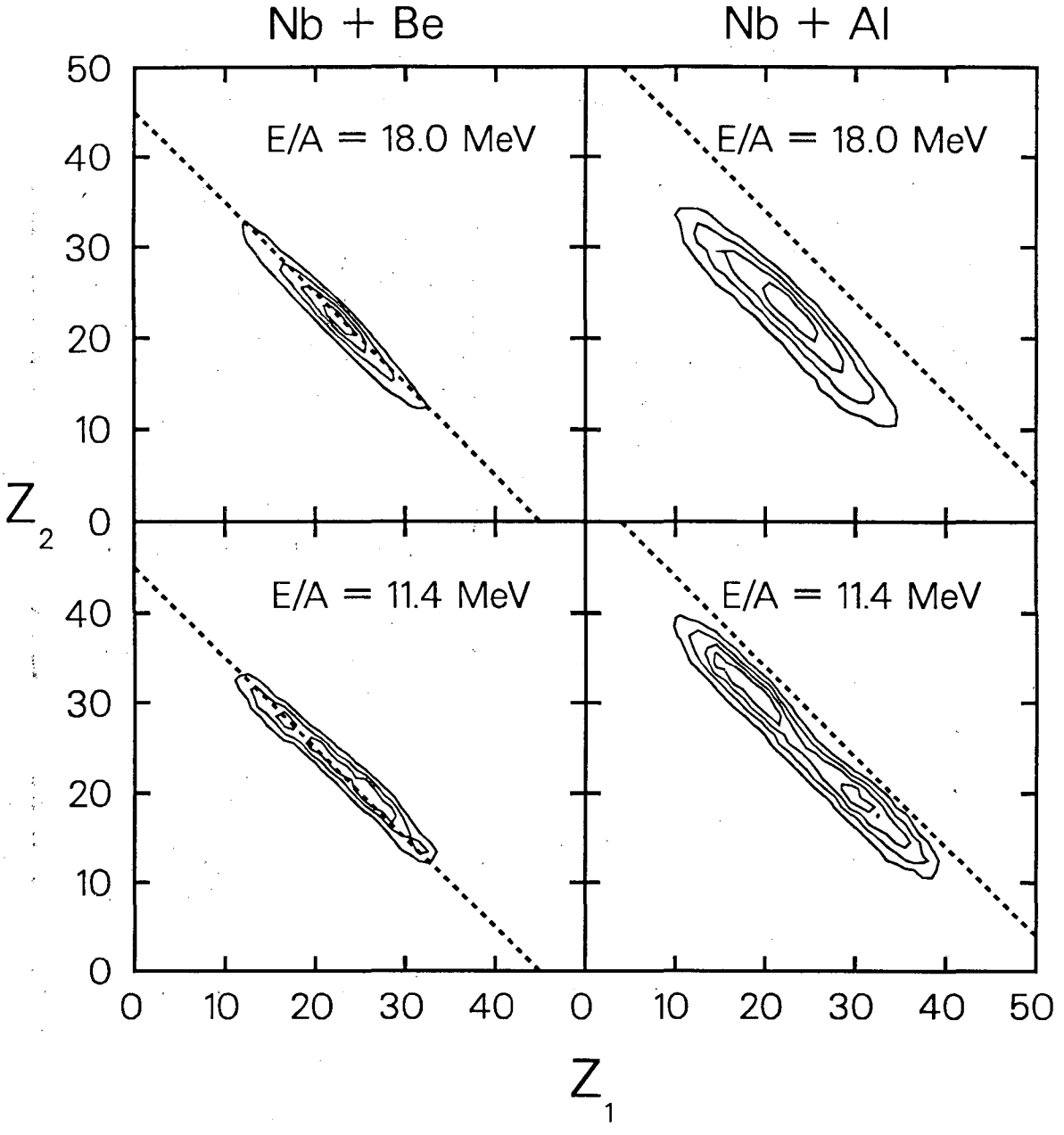

XBL 8710-4393

Fig. 25

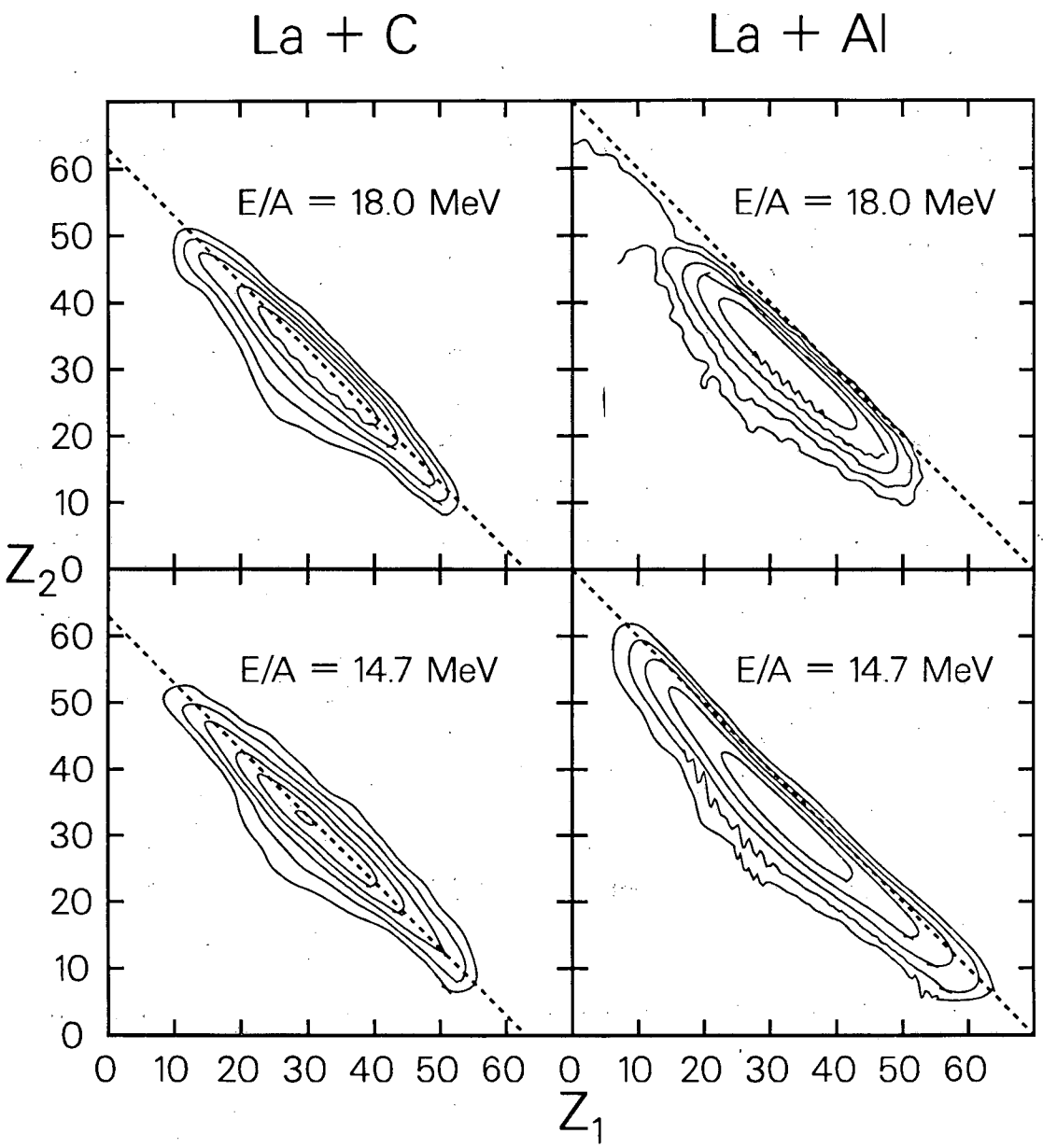
La + C
La + Al
E/A = 18.0 MeV
E/A = 18.0 MeV
E/A = 14.7 MeV
E/A = 14.7 MeV
Z_2
Z_1
0
10
20
30
40
50
60
XBL 895-1745

Fig. 26

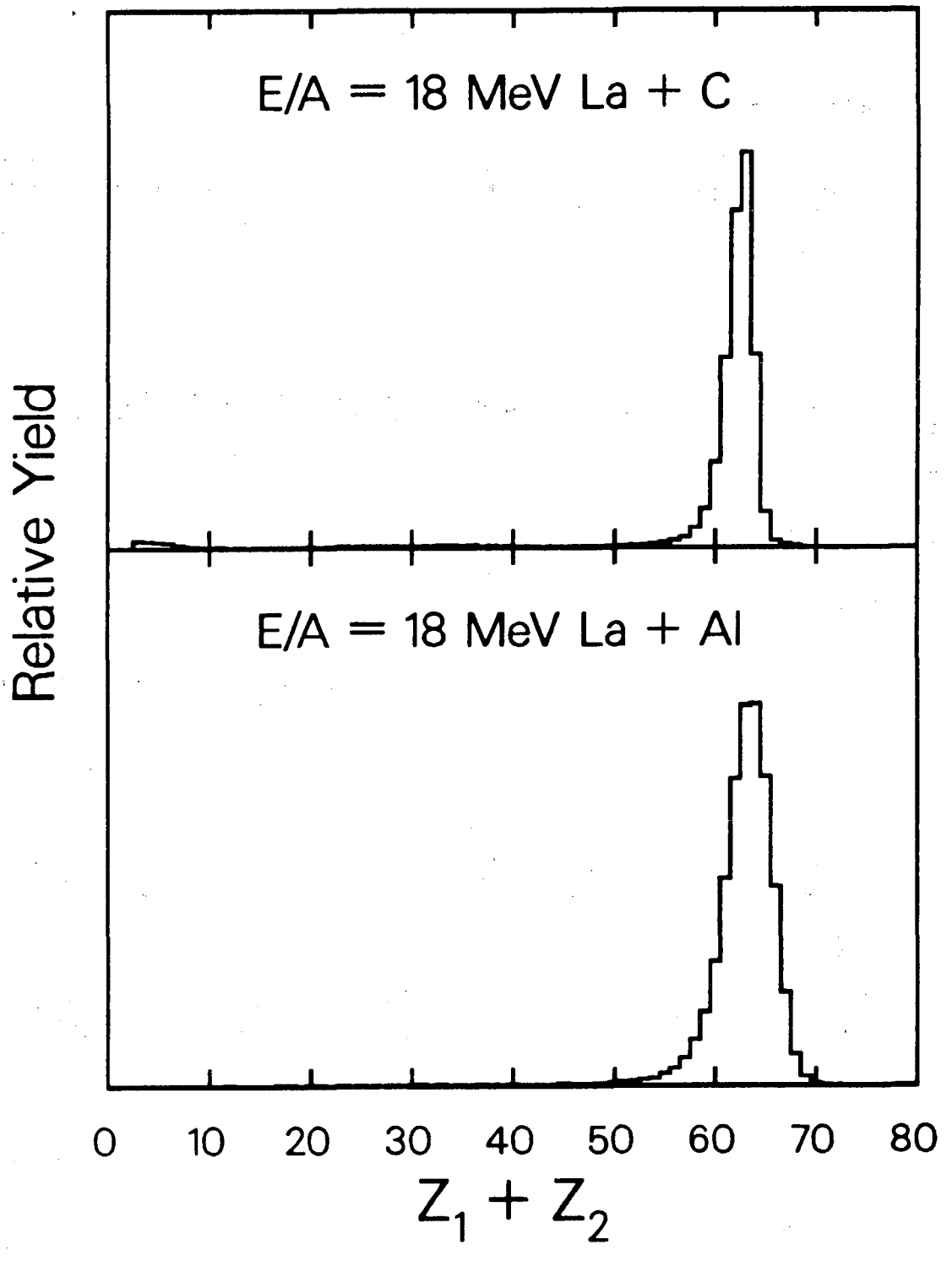

XBL 8712-5372

Fig. 27

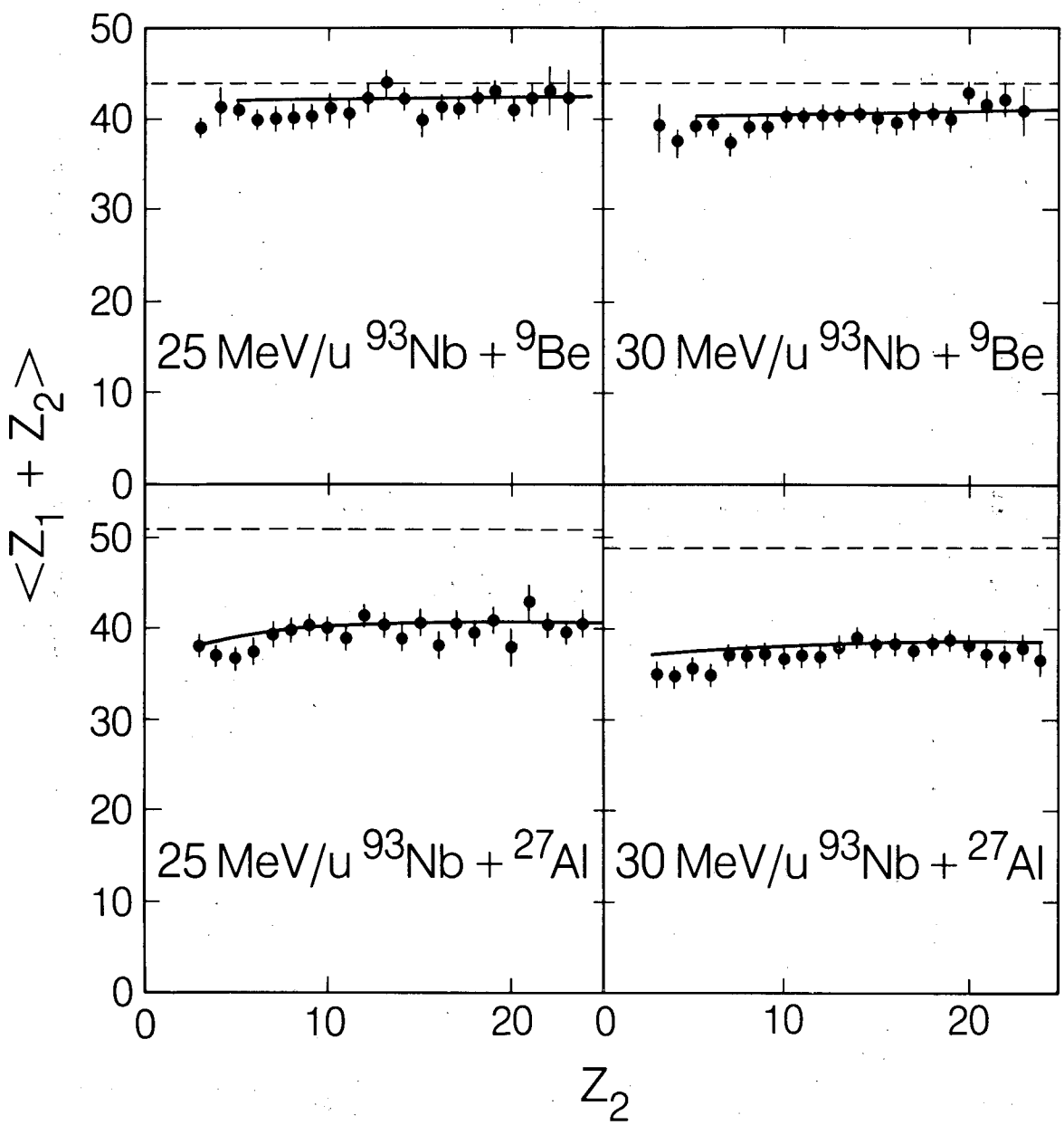

XBL 859-8977

Fig. 28

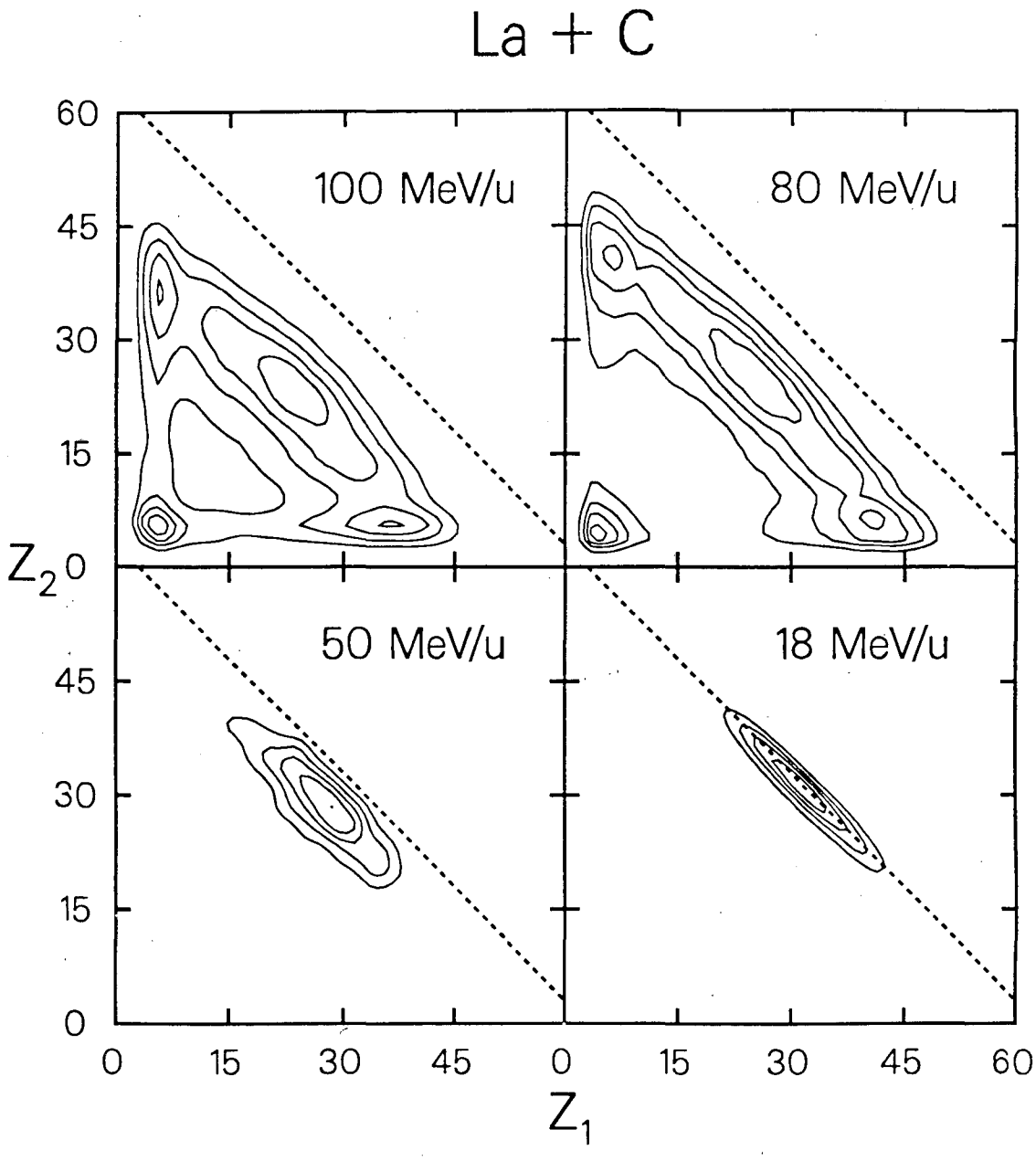
La + C
100 MeV/u
80 MeV/u
50 MeV/u
18 MeV/u
Z_2
Z_1
0
15
30
45
60
XBL 896-2411

Fig. 29

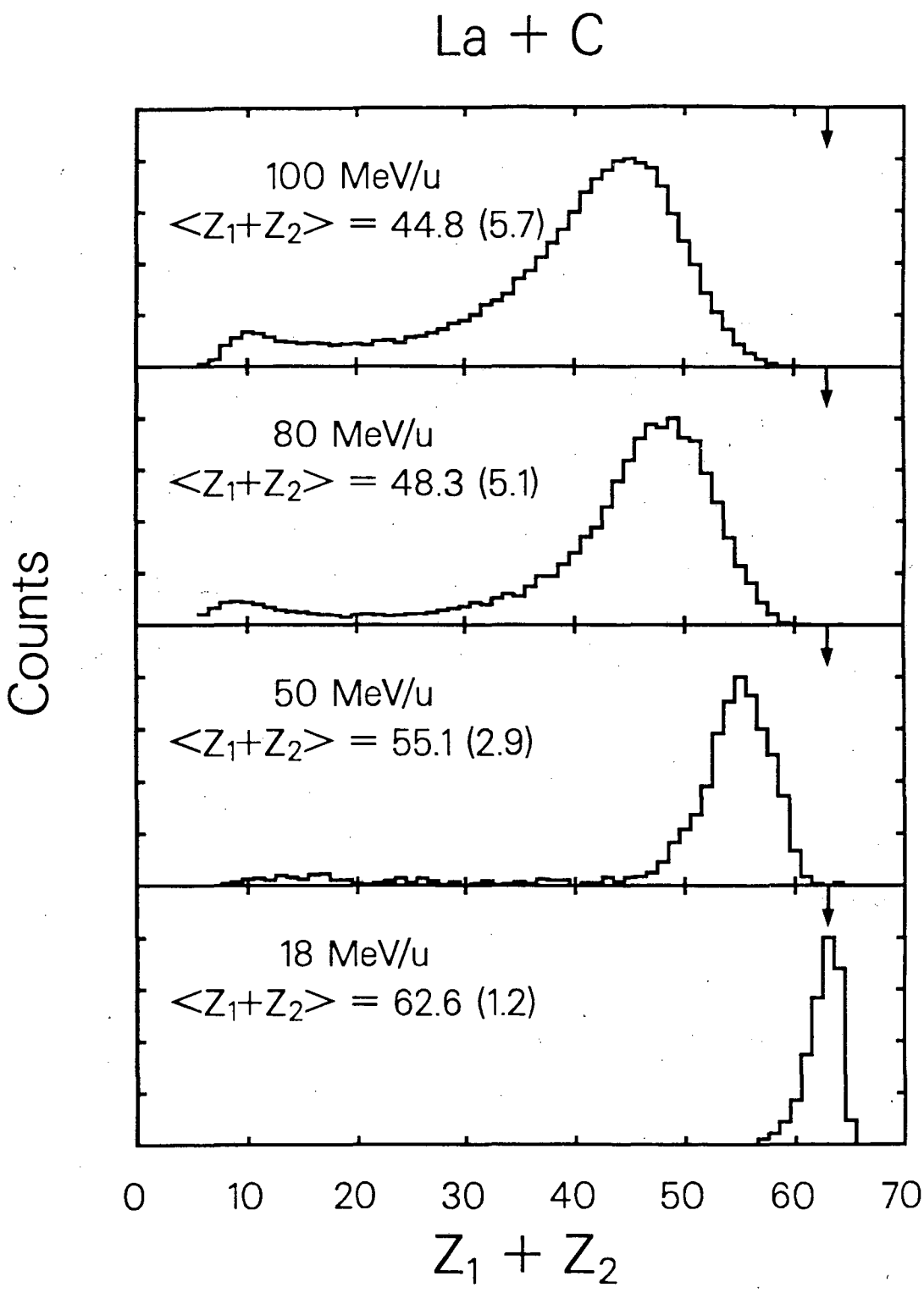
La + C
100 MeV/u
<Z1+Z2> = 44.8 (5.7)
80 MeV/u
<Z1+Z2> = 48.3 (5.1)
50 MeV/u
<Z1+Z2> = 55.1 (2.9)
18 MeV/u
<Z1+Z2> = 62.6 (1.2)
Counts
0
10
20
30
40
50
60
70
Z1 + Z2
XBL 896-2412

Fig. 30

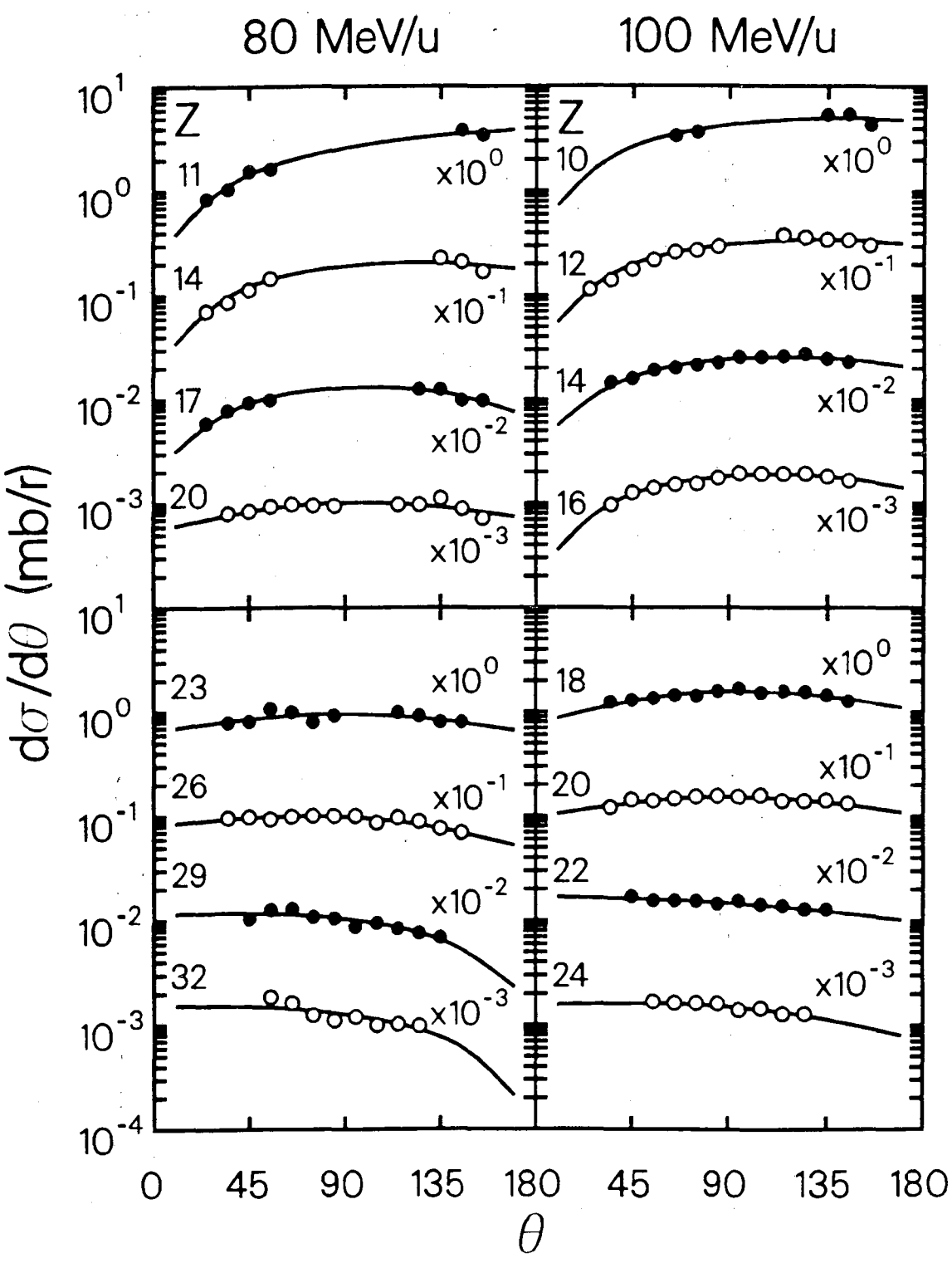

XBL 896-2413

Fig. 31

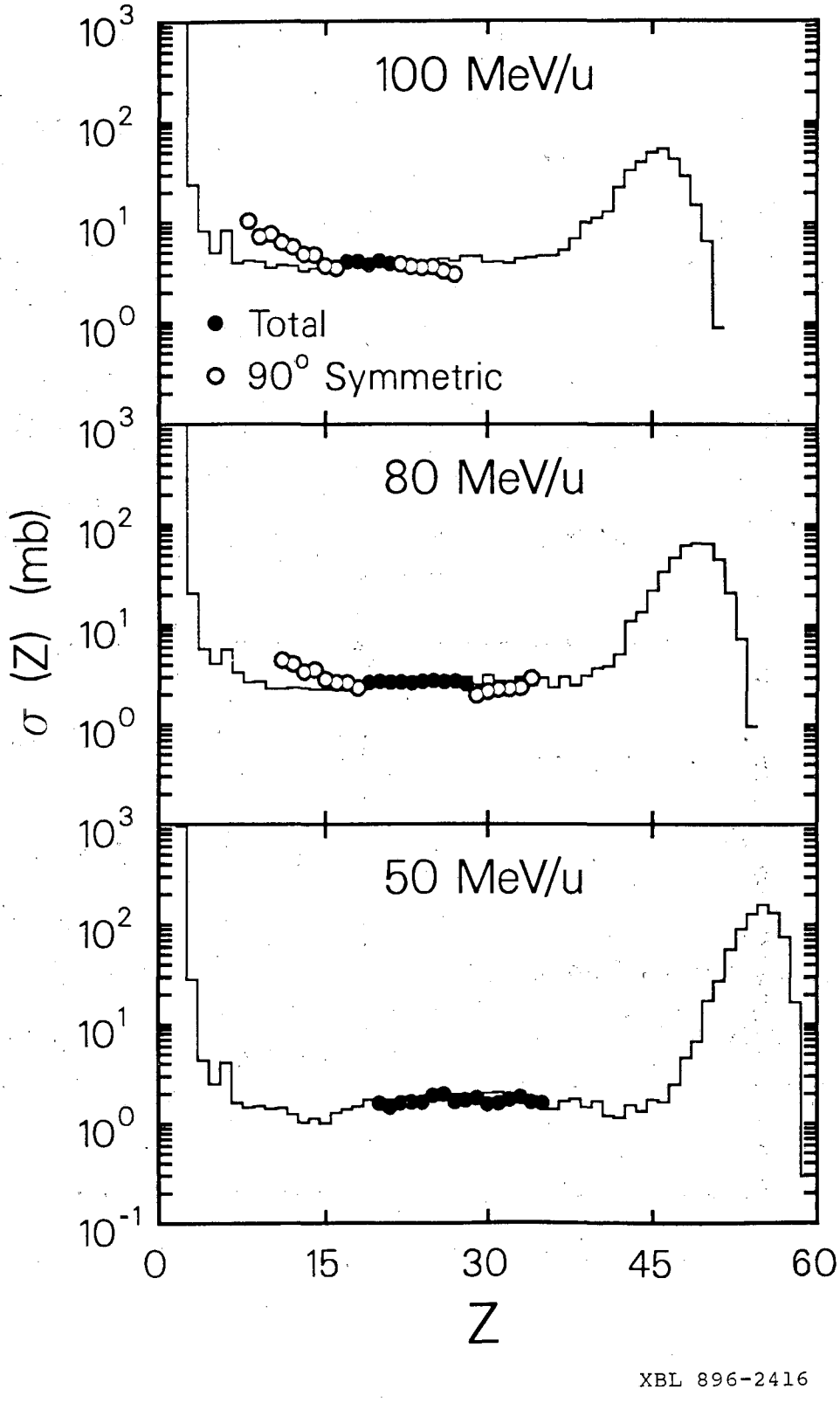
100 MeV/u
80 MeV/u
50 MeV/u
Total
90° Symmetric
σ (Z) (mb)
Z
XBL 896-2416

Fig. 32

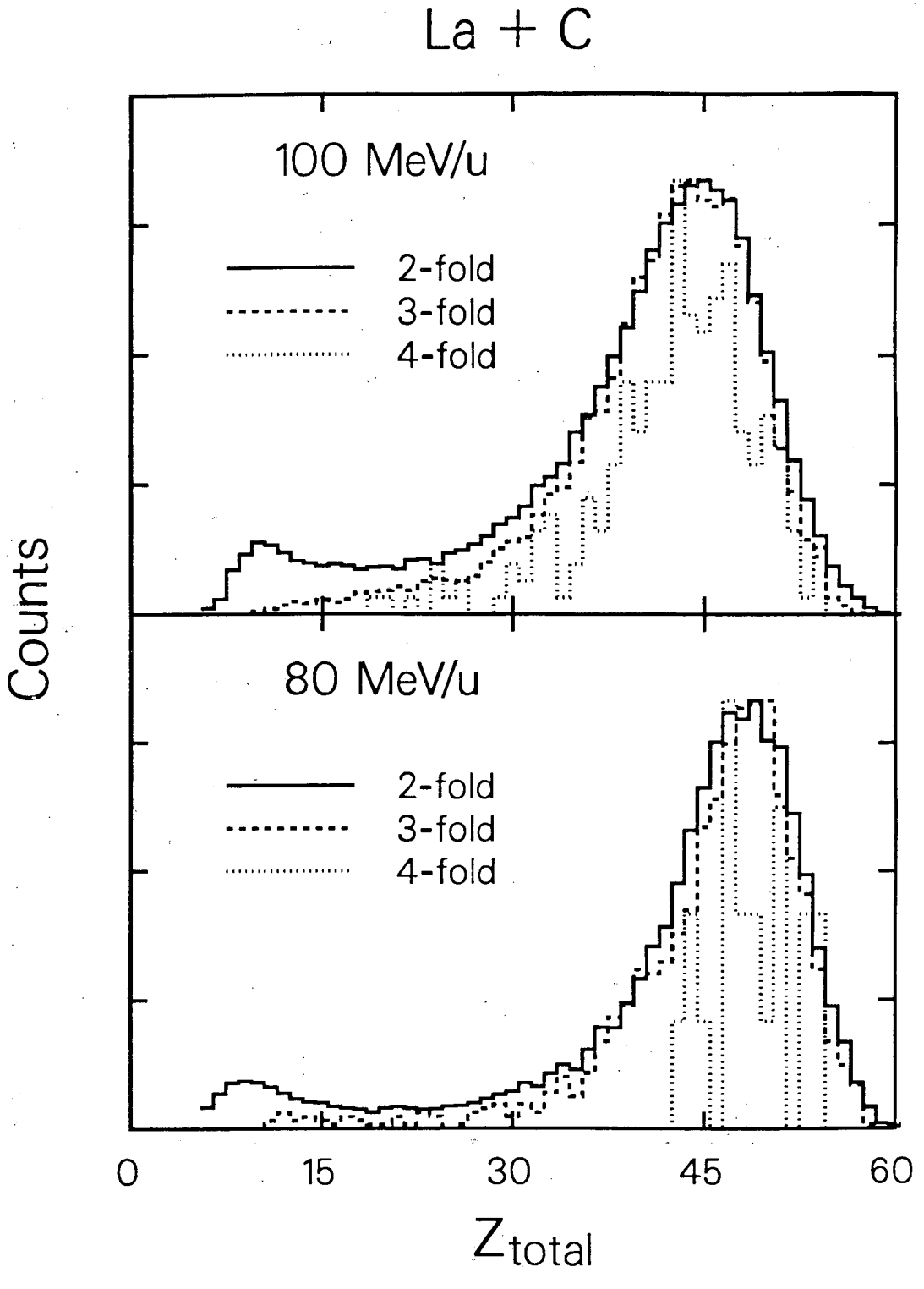
La + C
100 MeV/u
2-fold
3-fold
4-fold
80 MeV/u
2-fold
3-fold
4-fold
Counts
0
15
30
45
60
Ztotal
XBL 896-2414

Fig. 33

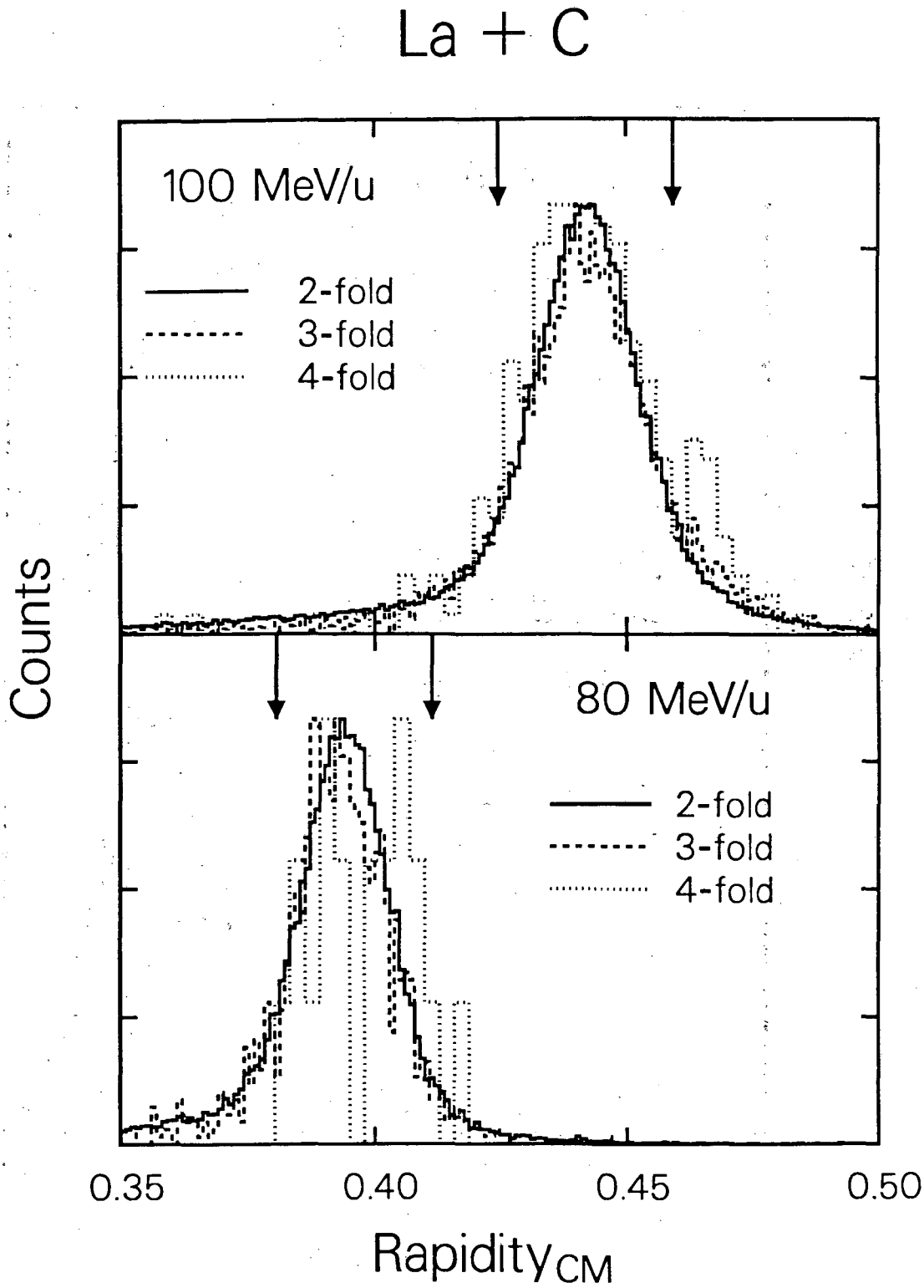
La + C
100 MeV/u
2-fold
3-fold
4-fold
80 MeV/u
2-fold
3-fold
4-fold
Counts
0.35
0.40
0.45
0.50
Rapidity$_{CM}$
XBL 896-2415

Fig. 34

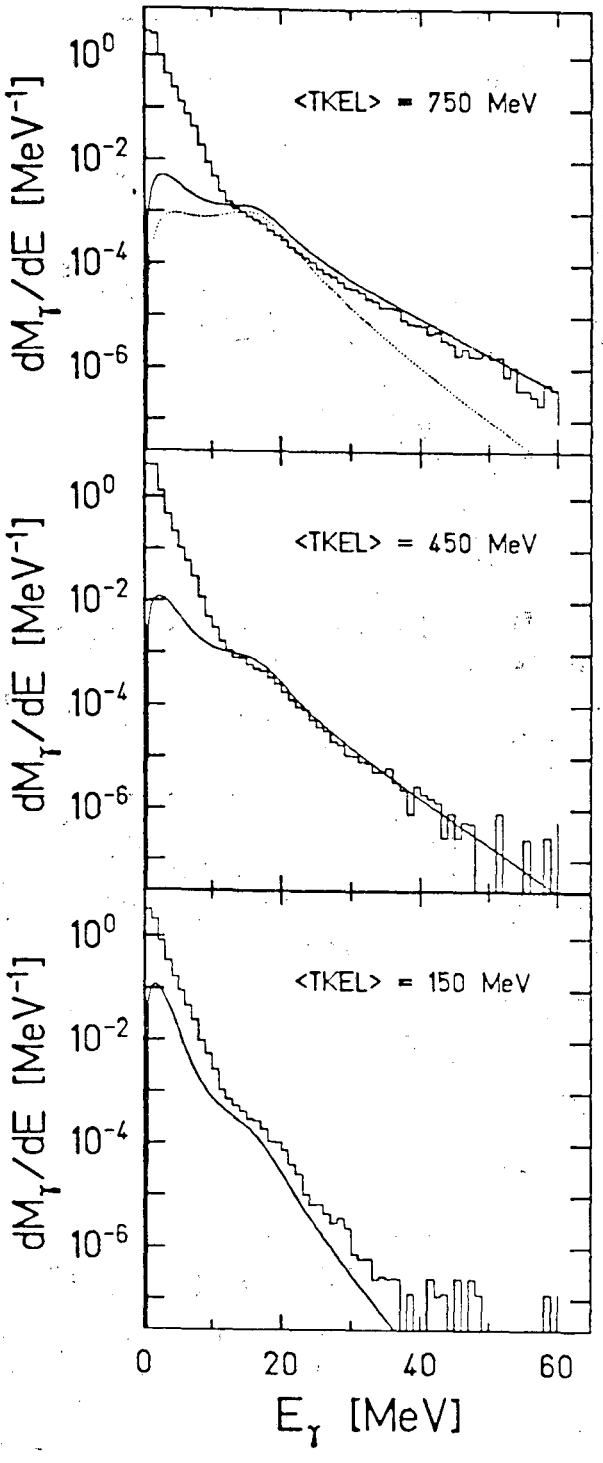

XBL 881-285

Fig. 35

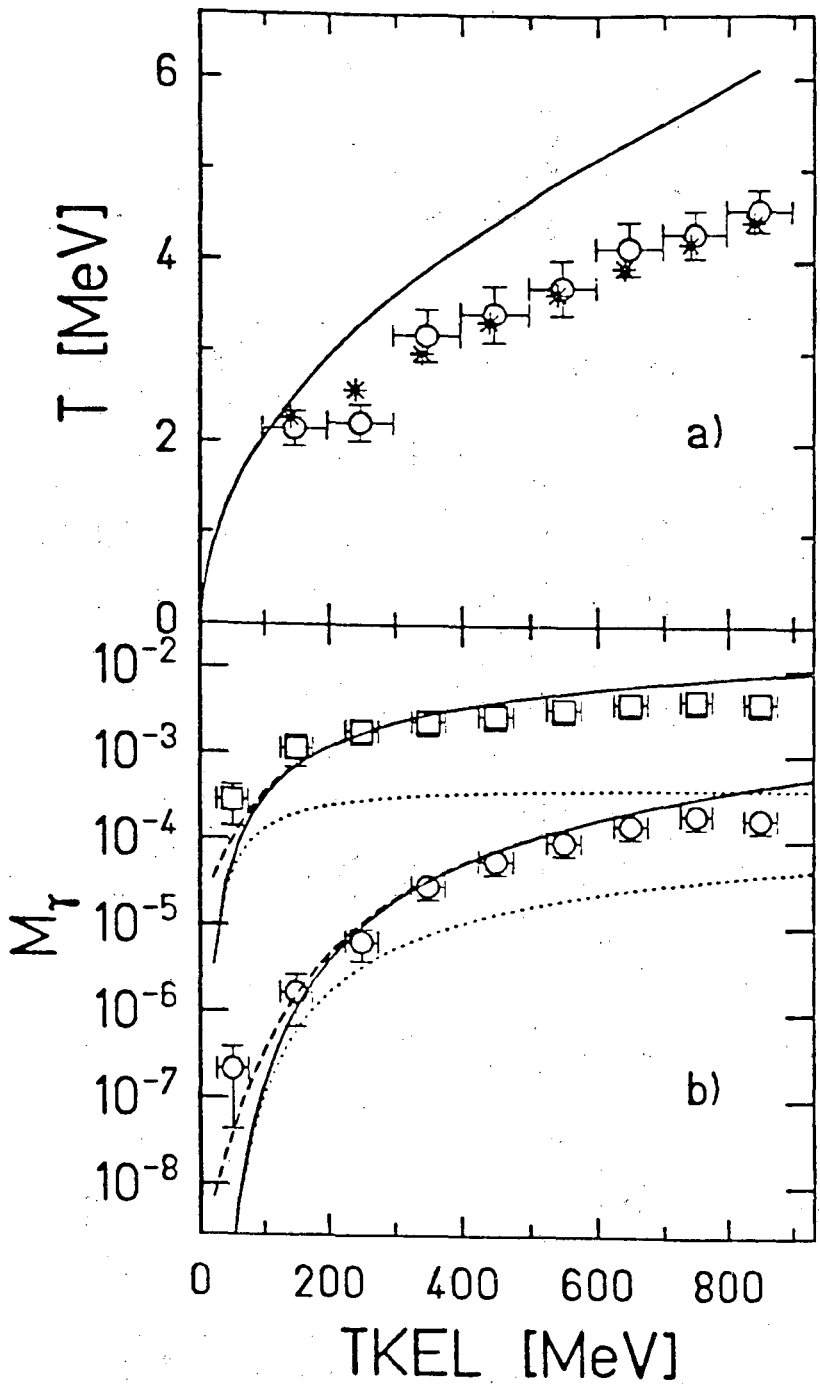

XBL 881-286

Fig. 36

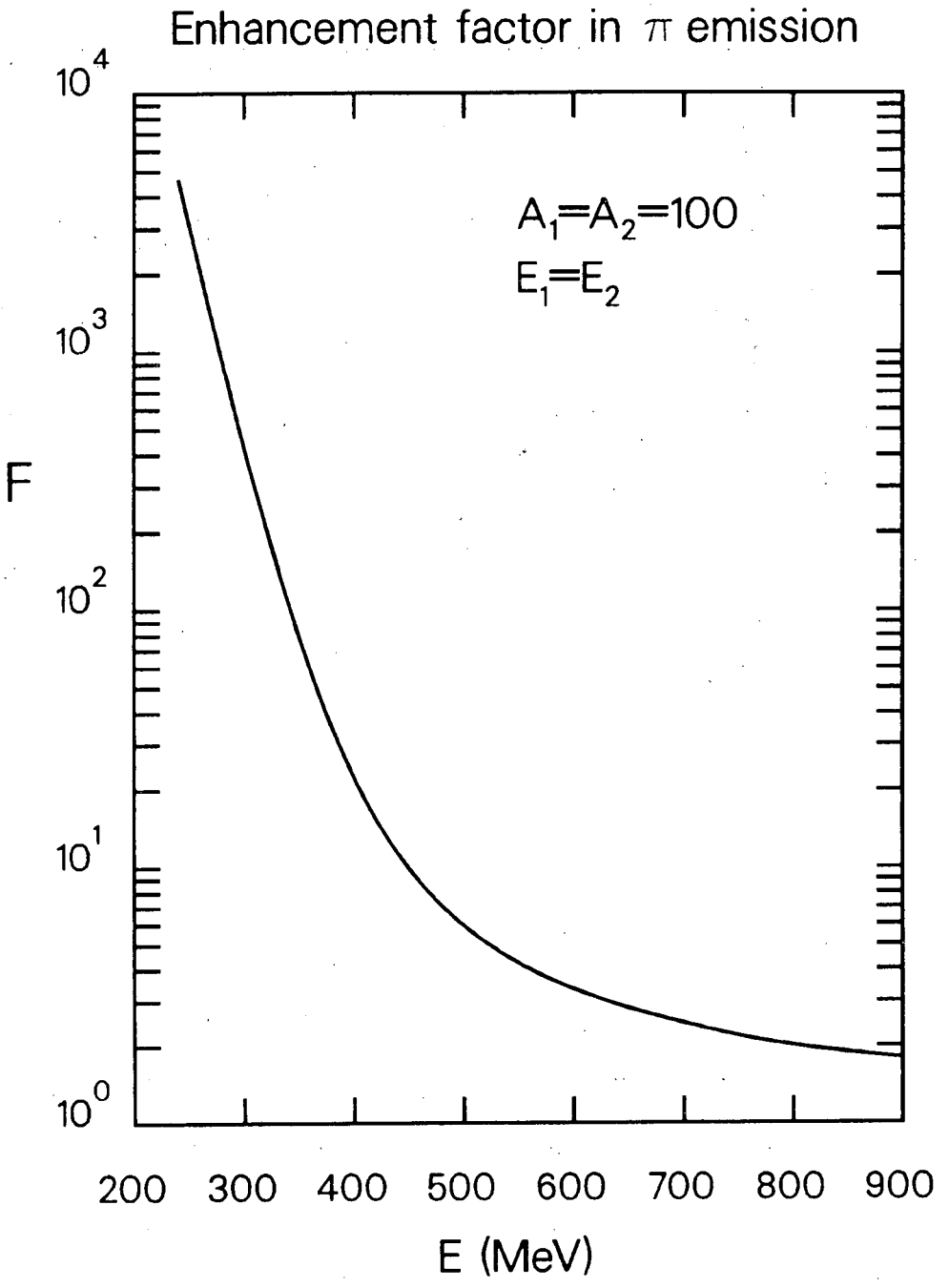

XBL 885-1806

Fig. 37

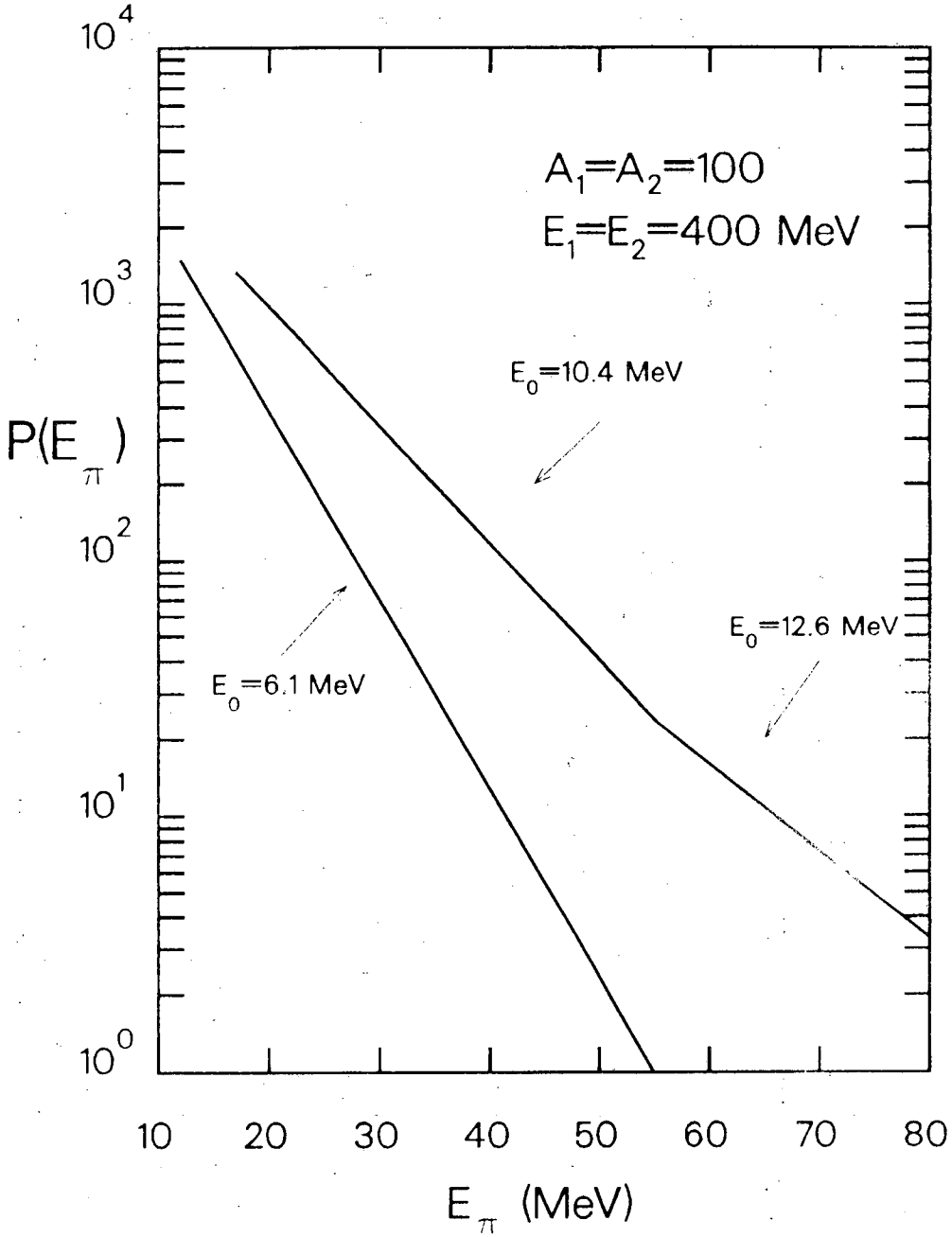
10^4
10^3
10^2
10^1
10^0
$P(E_\pi)$
$A_1=A_2=100$
$E_1=E_2=400$ MeV
E_0=10.4 MeV
E_0=12.6 MeV
E_0=6.1 MeV
10
20
30
40
50
60
70
80
E_π (MeV)
XBL 885-1807

Fig. 38

LAWRENCE BERKELEY LABORATORY
TECHNICAL INFORMATION DEPARTMENT
1 CYCLOTRON ROAD
BERKELEY, CALIFORNIA 94720